Spring 5-3-2024

SiC MOSFET Oscillator Circuit for Operation in High-temperature Harsh Environments: Design, Simulation, and Testing

Nikung Thapa
University of Maine, Nikung.thapa@maine.edu

SiC MOSFET OSCILLATOR CIRCUIT FOR OPERATION IN HIGH-TEMPERATURE HARSH ENVIRONMENTS: DESIGN, SIMULATION, AND TESTING

by

Nikung Thapa

B.E. Tribhuwan University IOE, 2017

A THESIS

Submitted in Partial Fulfillment of the

Requirements for the Degree of

Master of Science

(in Electrical Engineering)

The Graduate School

The University of Maine

May 2024

Advisory Committee:

Nuri Emanetoglu, Associate Professor of Electrical and Computer Engineering, Co-advisor

Mauricio Pereira da Cunha, Professor of Electrical and Computer Engineering, Co-advisor

Donald Hummels, Professor of Electrical and Computer Engineering

SiC MOSFET OSCILLATOR CIRCUIT FOR OPERATION IN HIGH-TEMPERATURE HARSH ENVIRONMENTS: DESIGN, SIMULATION, AND TESTING

By Nikung Thapa

Thesis Co-advisors: Dr. Nuri Emanetoglu and Dr. Mauricio Pereira da Cunha

An Abstract of the Thesis Presented
In Partial Fulfillment of the Requirements for the
Degree of Master of Science
(in Electrical Engineering)
May 2024

This thesis explores the design, simulation, and validation of a high-temperature (HT) Colpitts oscillator, motivated by the need for robust electronics in HT harsh environments (HE) across sectors such as space exploration, power generation, and industrial processes. The Colpitts oscillator circuit utilizes a silicon carbide (SiC) MOSFET in a source follower amplifier and an LC resonant tank circuit. The circuit was assembled on an alumina board with gold traces using silk-screen printing, and 1mm gold bond wires were employed for component connections.

The design and analysis of the oscillator, in both open and closed-loop configurations, involved deriving the transfer function from nodal equations, solved using MATLAB. Subsequently, simulations in Microcap assessed the oscillator's output characteristics. Sensitivity analysis highlighted the circuit's response to component variations, especially noting the oscillation frequency's sensitivity to inductor and capacitor values. Additionally, Monte Carlo simulations in both Micro-cap and MATLAB assessed the circuit's performance under varying temperatures and component tolerances.

Three circuits, labeled Prototype #1, Alpha, and Beta, were fabricated, and tested inside a furnace, powered by either a conventional power supply or Thermoelectric Generators (TEGs). These circuits operated successfully from room temperature to 350°C, demonstrating wireless signal transmission capabilities with successful detection 11 feet away from the furnace, validating their potential for remote wireless sensing in HT industrial environments. However, performance instability at 400°C and discrepancies between simulated and experimental results indicate future research directions, including the development of more accurate circuit models, improvements in circuit layout, and the exploration of temperature-compensated designs for improved stability. Thus, this thesis contributes to the advancement of high-temperature electronics, paving the way for the deployment of reliable wireless sensing technologies in HT HE settings.

ACKNOWLEDGEMENTS

I would like to express my sincere gratitude to all those who supported me throughout my thesis journey.

First and foremost, my deepest thanks go to Dr. Nuri Emanetoglu, for his constant support and assistance throughout my master's journey. His mentorship has been instrumental from start to finish, guiding me through every phase of my study. I am grateful to Dr. Mauricio Pereira da Cunha, and Dr. Donald Hummels for their guidance and feedback throughout the research process. I would also like to thank Luke Doucette and Mike Call for their help with the circuit assembly and fabrication process.

My appreciation also extends to my peers: Shane Winters, Emily Currie, Jude Zanoni, Mike Mooney, Shanon Scott, Conlan Taylor whose assistance and help have been beneficial to me in various aspects of my thesis work. Their contributions, whether in discussions, experimental setups, or just moral support, have been a great source of encouragement.

Lastly, I want to thank my family—my parents and my wife. Their endless love, understanding, and sacrifice have been the source of my strength and resilience.

TABLE OF CONTENTS

LIST OF FIGURES

LIST OF TABLES

CHAPTER 1

INTRODUCTION

1.1. Motivation

The need for resilient electronic systems that can function in extreme conditions is growing across various sectors, including space exploration initiatives like NASA's mission to Venus [1], highlighting the importance for advancements in technologies capable of withstanding harsh environmental challenges. Harsh environments include extremes of temperature, pressure, shock, corrosive elements, or radiation exposure. These conditions are prevalent in various industries, including geothermal energy [2, 3], oil and gas extraction [4, 5, 6] , automotive and aerospace engineering [7, 8, 9]. To ensure uninterrupted operation and avoid catastrophic incidents, real-time monitoring of parameters such as temperature, pressure, vibration, and various other critical variables, is crucial [2-9].

A significant challenge in developing circuits for high-temperature applications is the performance degradation of Si devices. At room temperature (RT, 300K) the intrinsic carrier density for silicon is 1.5×10^{10} cm^{-3}. At temperatures above 150° C, the intrinsic carrier density in silicon increases significantly to approximately 10^{13} cm^{-3} leading to increased leakage currents. At higher temperatures, it will become comparable to and may surpass the PN junction doping levels, shorting out the PN junction [10, 11]. The reduction in carrier mobility also degrades device performance [10]. There is thus a need to develop electronic devices and circuits that can endure high temperature conditions without experiencing a decline in performance. This can be achieved using wide bandgap (WBG) semiconductors such as silicon carbide (SiC), gallium nitride (GaN), aluminum nitride (AlN) and diamond [8-13],[28]. SiC has been investigated for high temperature applications due of its wide bandgap (3.23 eV at 300K for 4H-SiC) and resulting small intrinsic carrier concentration $(5 \times 10^{-9}\ \mathrm{cm}^{-3}\ at\ 300K)$, high thermal conductivity (330-490 W/mK)

[12], large breakdown electric field strength (2-4MV/cm) [13], and better chemical and mechanical stability than other WBGs [11]. These qualities position SiC-based devices as ideal candidates for the development of high-temperature electronic circuits.

Oscillators are vital components for electronic systems. In communications systems, oscillators are used to generate stable carrier frequencies which enable reliable transmission and reception of signals. They also provide timing signals for synchronization, ensuring precise operation of digital circuits and microprocessors. An oscillator circuit would be the beating heart of a wireless sensor system operating in harsh environments. Designing oscillators for high-temperature environments presents specific challenges, particularly in circuit design and the temperature dependence of the properties of electronic components, such as transistors, resistors, and capacitors. This study focuses on designing, constructing, and testing an oscillator circuit capable of continuous operation over a wide temperature range, from room temperature to at least 300 ℃. The aim is to demonstrate performance stability under a wide range of temperatures, ensuring reliability and ease of maintenance.

The surge in demand for electronics capable of functioning in high-temperature environments has necessitated the search for dependable power solutions. Thermoelectric generators (TEGs), with their ability to transform thermal energy into electrical energy via the Seebeck effect, present a viable option. Utilizing TEGs to power oscillators facilitates the development of robust wireless communication systems, particularly in scenarios where conventional power sources such as battery or solar power may prove challenging to perform.

This thesis addresses the need for dependable high-temperature electronics by developing and evaluating a silicon carbide (SiC) MOSFET-based oscillator circuit. The circuit is designed to function across a broad temperature range, from room temperature up to 400 °C.

1.2. Sensing Needs in Harsh Environments

Harsh environments pose unique challenges and demands for sensing technologies due to their extreme conditions such as high temperatures, high pressures, corrosive atmospheres, and high radiation levels. Various industries, such as power generation, aerospace, process control, and downhole drilling, require accurate and reliable sensors to operate effectively in these environments [2-9]. Demand for such sensors is high as they play an important role in ensuring the safety, efficiency, and proper functioning of equipment in a wide range of industries.

In the power generation industry, power plants have environments with high temperature and high pressure and may further have highly corrosive gases and/or liquids. For example, in modern gas turbines firing temperatures can reach up to 1427°C and gas pressure can reach 3000 kPA [14] . Efficiency is improved by 2-4% for each 55 °C increase in firing temperature [15]. The need for higher operating temperatures in turbine design has made blade life a critical bottleneck for performance. Modern blades, made with advanced metallurgy, can withstand temperatures between 537°C and 704°C [16]. However, due to the temperature limits of older sensors, data on blade integrity and prevention of hot corrosion, which is an accelerated corrosion that occurs when they are exposed to corrosive environment at high temperatures, is often collected indirectly, away from the key areas. This necessitates the use of mathematical models to estimate blade temperatures, leading to a higher margin of error in operating parameters.

In the aerospace sector, which includes both aviation and space exploration, conditions experienced by the systems and components are very challenging. For example, the operating temperatures can exceed 1500°C in the combustion chamber of jet engines and the turbine inlet temperature can often reach up to 2000°C [17]. For planetary exploration missions, such as those to Venus which has a surface temperature of 450°C, high pressures, a corrosive environment, and

high radiation levels may be encountered [1]. Typical sensor needs for the aerospace industry include, but are not limited to, temperature, pressure, and vibration monitoring.

In the automotive industry, the demand for durable sensors that can withstand extreme temperatures is critical. Vehicles' exhaust systems, engine compartments, and combustion chambers expose sensors to temperatures ranging from 150°C to 800°C [18]. These sensors are crucial for vehicle safety. Electric vehicles (EVs) also require sensors in battery management systems, power electronics, and electric drivetrains to function under high heat, ensuring efficient monitoring and control.

The field of downhole drilling in oil and gas exploration presents significant challenges for sensing technologies. Drilling in downhole environments poses significant challenges due to high corrosion potential and temperatures reaching up to 230°C [16]. Operators depend on accurate measurements of the drill bit's temperature, acceleration, and position to optimize drilling performance and safety. Furthermore, the implementation of sensors to measure pressure, density, and mass flow has been investigated as a means to detect early signs of fluid influx, known as "kick", which poses a risk of causing catastrophic blowouts, endangering both the drilling operation and environmental safety [5].

In response to the critical demand for monitoring in harsh environments, various sensors are used to accurately measure parameters under extreme conditions. Among these, thermocouples have already been demonstrated for their ability to measure exceedingly high temperatures about 1750°C [19], making them indispensable in environments where thermal monitoring is crucial. Strain gauges have been demonstrated used for their robustness and reliability in measuring mechanical stress at temperatures higher than 800°C [20]. Additionally, acoustic wave sensors (AW sensors) have proven highly effective, capable of operating up to 1000°C [21].

1.3. Semiconductor Technologies Used in Harsh Environment Electronics

The performance and durability of electronic systems in harsh environments are determined by the technology used. High temperature and harsh environment electronics demand careful material selection and implementation techniques. The trends and recent developments in harsh environment sensing applications are reviewed in this section, exploring limitations and advances in various technologies.

Silicon (Si) has been the dominant material in semiconductor technology for many years. However, it has limitations when it comes to temperatures above 150 °C. In these conditions silicon starts to exhibit performance degradation, including reduced carrier mobility, increased leakage current, and gate oxide reliability issues [10].

A key aspect of this degradation is due to the increase in intrinsic carrier concentration as temperature rises. This increase, an inherent material property of semiconductor materials, results from the exponential growth in increase with temperature which is defined by equation 1.

$$n_i = \sqrt{N_C N_V} e^{\left(-E_G / k_B T\right)} \quad (1)$$

where n_i is the intrinsic carrier concentration in cm^{-3}, temperature T is expressed in Kelvin, k_B is the Boltzmann constant, and E_G is the bandgap energy of the semiconductor in eV. N_C and N_V are effective density of states in the conduction and valence bands, respectively. Figure 1 shows the intrinsic carrier concentration of silicon, 6H-SiC, and 2H-GaN.

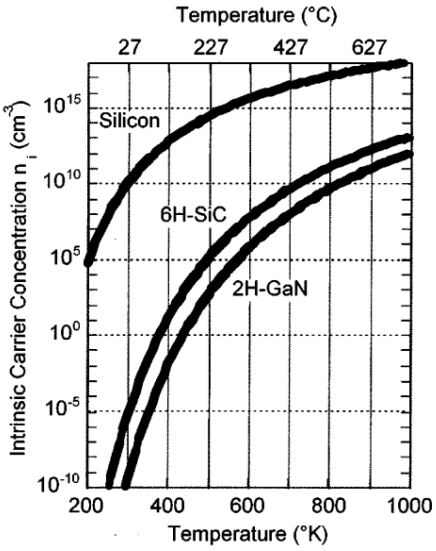

Figure 1: Comparison of intrinsic carrier concentration as a function of temperature for silicon, 6H-SiC, and 2H-GaN semiconductors [11]

Figure 1: Comparison of intrinsic carrier concentration as a function of temperature for silicon, 6H-SiC, and 2H-GaN semiconductors [11], for Si at high temperatures, the intrinsic carrier concentration can reach levels that exceed those of the dopants, adversely affecting the device's electrical conductivity. For example, silicon's intrinsic carrier concentration is in the order of 10^{15} cm^{-3} at 227°C. In contrast, wide bandgap semiconductors like SiC and GaN ($E_G > 3.3\ eV\ @\ 300\ °K$), have lower intrinsic carrier concentrations at elevated temperatures. For example, at 627 °C, the intrinsic carrier concentrations of SiC and GaN are on the order of 10^{13} cm^{-3} and 10^{12} cm^{-3}, respectively [11].

Silicon-on-Insulator (SOI) technology, where a thin layer of silicon is placed on an insulator, often silicon dioxide or sapphire, has emerged as an alternative that can mitigate some of the limitations of traditional silicon. In comparison with bulk silicon, SOI MOSFETs offer significant advantages in high-temperature applications, reducing leakage currents (3 to 4 order smaller), reducing variation of threshold voltage (2 to 3 times) and improving output conductance,

enabling circuits to operate up to over 300 °C [22]. It also offers advantages such as reduced parasitic capacitances for high frequency applications. The operation of an 8-bit embedded microcontroller has been demonstrated from -40°C to 250°C using SOI CMOS technology [23]. Also, a gate driver circuit for SiC FET switches using a SOI process showed successful operation up to 200°C [24].

Wide bandgap semiconductors are required to develop electronic circuits capable of operating at temperatures above 250°C. They exhibit outstanding properties, including high thermal conductivity, carrier mobility, and breakdown electric field. These materials outperform current Si technology in high temperature applications, paving the way for next-generation power conversion devices to function at elevated switching frequencies and temperatures, significantly reducing power losses and device size [25].

Figure 2 presents a comparative analysis of the material properties of GaN, SiC, and Si. Si's low breakdown field (0.3 MV/cm) and bandgap (1.12 eV) limit its use in high-voltage and high-temperature devices, despite its good electron mobility (1500 cm^2/Vs) and moderate thermal conductivity (150 W/mK). SiC excels with a high breakdown field (2.5 MV/cm), wide bandgap (3.3 eV), higher saturated electron velocity (2x10 ^{7} cm/s), and superior thermal conductivity (490 W/mK), making it ideal for high-voltage, high-power, and high-temperature applications. GaN offers the highest breakdown field (3.3 MV/cm) and bandgap (3.4 eV) among the three, along with the highest saturated electron velocity (2.7x107 cm/s) and high electron mobility (2000 cm^2/Vs) but has lower thermal conductivity (130-200 W/mK) compared to SiC. These characteristics make GaN and SiC more suitable than Si for demanding environments requiring high efficiency, speed, and thermal management.

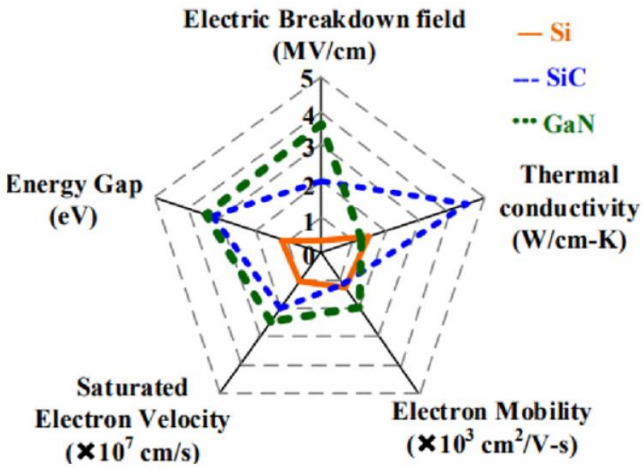

Figure 2: Comparison of semiconductor material properties of Si, SiC and GaN [25].

GaN and its alloy with Aluminum (AlGaN) are two wide bandgap materials that have shown promise in high temperature and power electronics. Although the operation of III-N Insulated Gate Field-Effect Transistors (IGFETs) at temperatures surpassing 600°C has been demonstrated, sustained performance at these high temperatures requires further enhancements in gate insulation capabilities [26]. Reference [27] describes the development of a 31-stage ring oscillator, frequency dividers, various logic gates, and a comparator using GaN/AlGaN HFET devices, all of which have been successfully tested at 300°C. Also, diamond is another example of the WBG semiconductor technology that has the potential for high temperature applications [28].

SiC is another wide bandgap material that is suited for high temperature and high-power applications. An advantage of SiC over III-nitrides is that SiC wafers are easily available [29] and NASA's Glenn Research Center has confirmed the long-term reliability and stability of SiC JFET technology through extensive testing at an ambient temperature of 500°C [1] for several thousand hours. These tests included experimental evaluations of amplifier stages and logic gates.

Temperature sensors capable of operating up to 450°C utilizing SiC Schottky diodes and MOS capacitors were reported in [7]. A Colpitts oscillator circuit that incorporates a SiC Metal-Semiconductor Field-Effect Transistor (MESFET) has been reported [30]. Figure 3 presents a compact, high-temperature wireless MEMS sensing and data telemetry system. Key components (SiC MESFET, pressure sensor, resistors, capacitors) are integrated on a ceramic substrate using gold wire bonding and are placed at the center of spiral inductor. The packaged SiC MESFET forms the core of a Colpitts oscillator which has been demonstrated to function at 400°C with 1-meter telemetry range. Similarly, Maximilian C. et al have also demonstrated a wireless pressure sensing solution using a SiC MESFET based clap oscillator, capable of operating up to 400°C and have explored energy scavenging partially i.e TEGs were driving the gate of the MESFET while power supply was used to supply drain voltage [31].

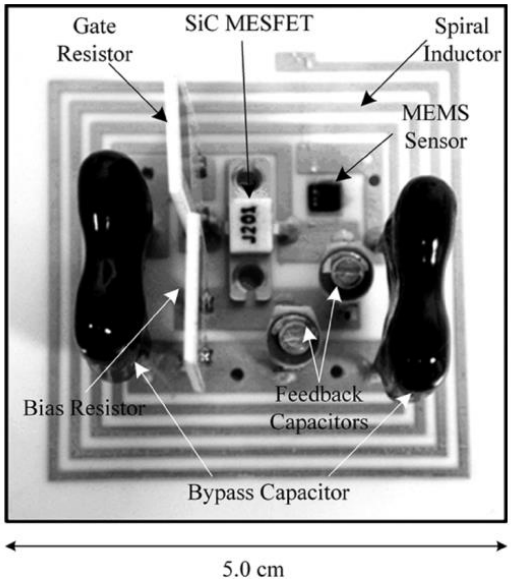

Figure 3: A Colpitts oscillator based on SiC MESFET [30]

1.4. Powering Semiconductor Circuits for HT HE Operation

Powering electronic circuits in high-temperature harsh environments poses significant challenges. An external power source wired to the circuit in the harsh environment may not be practical or feasible. Alternative methods for powering these circuits are needed. This section explores existing energy scavenging technologies and focuses on thermoelectric generators (TEGs).

The need for an in-situ power source for active electronic components, such as transistors, has led to the exploration of energy-harvesting techniques. The techniques include solar energy harvesting that employs photovoltaic cells to convert sunlight to energy. Kinetic energy capture through piezoelectric or electromagnetic means, is suited for devices in motion-intensive applications like wearables. RF harvesting captures electromagnetic waves from the surroundings, providing power for small devices in urban environments. Thermal harvesting uses TEGs to utilize temperature gradients, often found in industrial waste heat, for power generation [32]. Despite efforts to adapt SiC technology for use in high-temperature applications [28-32], energy-harvesting approaches have yet been applied to power SiC transistor circuits with milliwatt-level or higher power needs in a fully standalone and wireless mode within high-temperature harsh environments (HT HE).

Thermal energy harvesting is as a viable option due to the availability of thermoelectric generators (TEGs) capable of delivering the power required for biasing circuits and potential operation up to 900 °C [33]. Figure 4 shows the cross-section of a TEG. TEG power modules create a voltage difference between cooler and warmer surfaces through the Seebeck effect in both P and N doped materials. This makes TEGs an appealing choice for powering circuits in scenarios with suitable temperature gradients. TEG technology has found applications in a wide array of

harsh environments, from interplanetary probes [34] and deep-sea energy harvesting [35] to combustion engine waste heat recovery [36]. TEGs have been explored for use in various settings, including ships, locomotives, and human bodies [37,38] A Si-based wireless sensor network was powered by exploiting temperature gradients between the inside and outside of a window frame in winter [37].

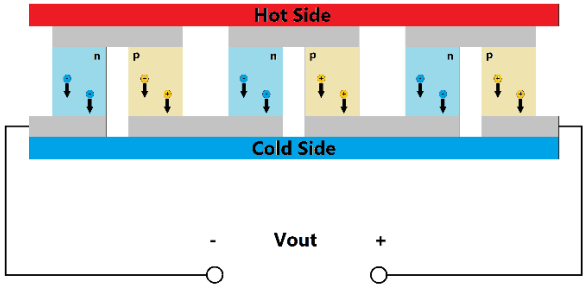

Figure 4: Cross-section of a TEG module [38]

1.5. Oscillator Circuits

Oscillators play a crucial role in various applications, including wireless communication and sensing, generating periodic signals like sine waves or square waves [39]. This section provides a background on oscillators, focusing on the fundamental concepts underlying oscillation and the technical aspects involved in their design. Also, basic components in oscillators and the desired operation and stability characteristics are discussed. Furthermore, different types of oscillators are explored.

1.5.1. Principles of Oscillators

Oscillators rely on feedback mechanisms to sustain oscillation, which provides a continuous output signal without an external input. The fundamental principle of oscillation involves the balance between amplification and feedback. For an oscillator to maintain continuous

and stable oscillations, it must satisfy the Barkhausen Stability Criterion. This criterion consists of two fundamental conditions [41].

1. The Magnitude Condition: The loop gain, which is the product of the amplifier's gain and the feedback factor, must be equal to be 1 to sustain oscillation. This condition ensures that the oscillator can compensate for signal loss and sustain oscillations over time. The loop gain should be larger than 1 to initiate oscillation.
2. The Phase Condition: The total phase shift around the loop should be an integer multiple of 2π radians (or 360°). This condition ensures that the feedback signal and the input signal are in phase thereby supporting, not cancelling the oscillation.

Core components of an oscillator include an amplifier for signal amplification, a feedback network for routing signals back into the system, and a resonant element that sets the frequency of the oscillation. The amplifier boosts the amplitude of the signals and compensates for the energy loss within the circuit. The feedback network, as the name suggests, feeds the output signal back into the system's input. The phase and magnitude of this feedback signal are crucial for maintaining steady oscillations. The resonant element, such as a capacitor-inductor network in LC oscillator determines the oscillation's frequency based on its properties.

1.5.2. Common Oscillator Types

a. Ring Oscillators:

Ring oscillators are a type of digital oscillator where an odd number of NOT gates are connected in a ring-like configuration, as shown in Figure 5 with the output of the last NOT gate fed back into the first [42]. The ring oscillator does not require an external frequency source, and instead uses the inherent delay through the NOT gates to generate a periodic signal. This type of oscillator is often used in integrated circuits due to its simplicity and ease of integration. The

frequency of the oscillator circuit can be adjusted by varying the number of gates in the ring or the supply voltage. A significant disadvantage of this topology is that the propagation delay is determined by the switching of the transistors, which changes with temperature. As such, these oscillators suffer from significant drift and are not used for applications where precise time keeping is required, for example in global positioning system (GPS) receivers.

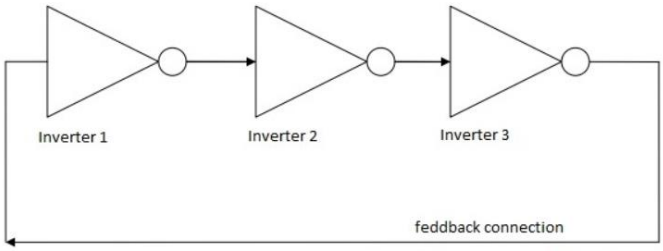

Figure 5: A simple ring oscillator *[40]*

b. Resistor-Capacitor (RC) oscillators:

RC oscillators use resistors and capacitors in conjunction with an amplifier circuit, as shown in Figure 6. The RC time constant determines the frequency of oscillation. These oscillators are generally used for generating low-frequency signals, typically in the audio range. RC oscillators are valued for their simplicity, low cost, and the ease of tuning their output frequency by adjusting the resistor or capacitor values. However, they are sensitive to component variations and environmental conditions. Some examples include the phase-shift oscillator and the Wein bridge oscillator.

The phase-shift oscillator uses a phase-shift network of resistors and capacitors to provide the necessary phase shift and feedback. By cascading multiple stages of RC network as shown in Figure 6, a total phase shift of 180 ° is achieved, enabling sustained oscillations. The oscillation frequency is determined by the time constant of the RC network. In the simplest design, the

resistors all have the same value R and the capacitors all have the same value C, the oscillation frequency is given by:

$$f = \frac{1}{2\pi RC\sqrt{6}} \tag{2}$$

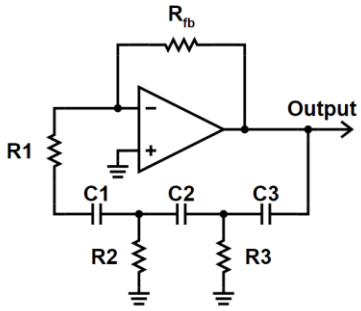

Figure 6: A simple ring oscillator *[40]*

The Wein bridge network oscillator uses a Wein bridge network for feedback and stability as shown in Figure 7. They consist of bridge network with resistors and capacitors connected to an operational amplifier or an active device. The balance between the reactive and resistive components in the bridge circuit enables oscillation. In Figure 7, the circuit incorporates two distinct feedback networks: one composed of resistors Rf and Rs, which furnishes negative feedback to establish the amplifier's gain, and the other, an RC network, that supplies positive feedback. These combined feedback mechanisms enable the oscillator to sustain oscillations by balancing the amplification and phase shift requirements for continuous wave generation [41]. The oscillation frequency is determined by the resistor and capacitor values in the bridge network. For the simple circuit below the frequency is given by

$$f = \frac{1}{2\pi RC} \tag{3}$$

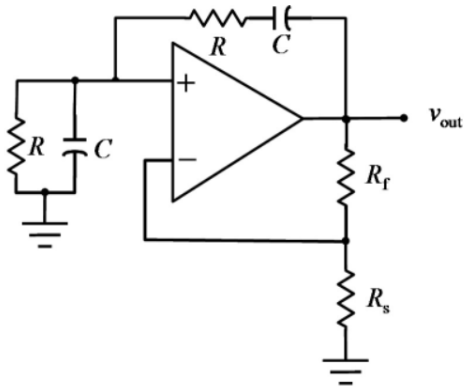

Figure 7: Wein bridge oscillator using op amp [42]

c. LC Oscillators (Inductor-Capacitor Oscillators):

LC oscillators utilize a tank circuit composed of an inductor and a capacitor to generate high frequency signals. The frequency of the output waveform depends upon the values of inductors and capacitors. They are used in applications like radio transmitters and receivers due to their ability to generate stable frequency signals. ranging from MHz to GHz. Some examples include the Hartley oscillator and the Colpitts oscillator which is shown in Figure 8.

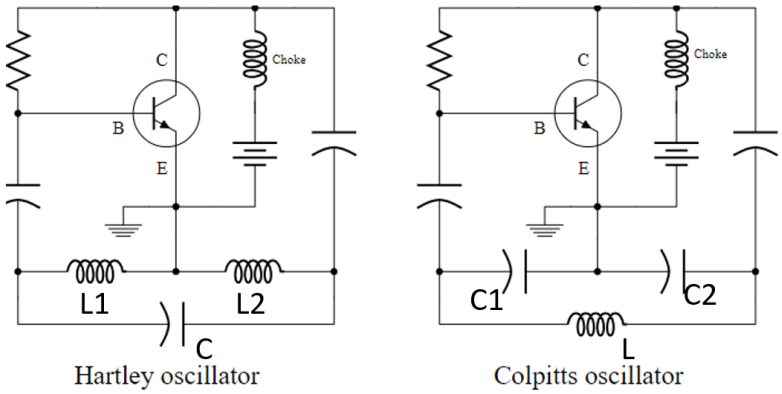

Figure 8: Schematic of Hartley oscillator and equivalent Colpitts oscillator [43].

In Figure 8, The Hartley oscillator uses a pair of inductors in series (L1 and L2) and a capacitor (C) for its feedback network. The inductors are typically connected to the common ground or reference point. The active device, such as transistor or vacuum tube, provides amplification and positive feedback to sustain oscillation.

The Colpitts oscillator utilizes two capacitors (C1 and C2) and an inductor (L) in its tank circuit. The capacitors are connected in series, and the junction between them is connected to the base or gate of the active device. The other end of the capacitor is connected to the common ground or reference point. This configuration creates a voltage divider, resulting in positive feedback that sustains oscillations. The Colpitts oscillator can be simple to design and implement. It has a wide frequency range and it's relatively easy to tune by adjusting the values of capacitors or the inductor. Additionally, it has low output impedance making it suitable for driving other circuits.

d. Crystal oscillators:

Crystal oscillators use a piezoelectric crystal, typically quartz, as a high-Q resonator to generate highly stable and precise sinusoidal waveforms. The quartz crystal vibrates at a specific frequency when subjected to an electric field due to the piezoelectric effect. This resonant frequency serves as a precise reference for generating the desired output frequency. Cystal oscillators offer several advantages over other oscillator types such as high frequency stability, low phase noise and distortion waveforms, temperature stability, and low power consumption. However, they can be expensive and sensitive to physical stress. Figure 9 shows an example of a Pierce crystal oscillator that uses a crystal typically Quartz in the feedback path, a BJT as an amplifier and two capacitors C1 and C2 connected in series with the crystal forming a network with the crystal to determine the oscillation frequency [41].

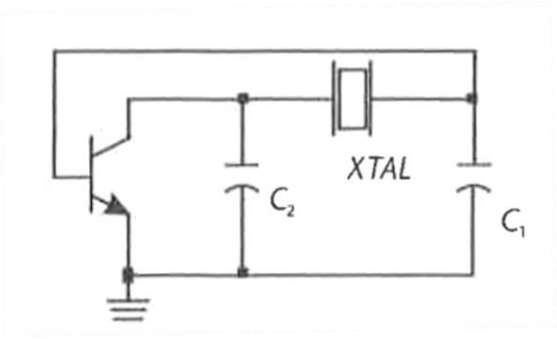

Figure 9: A Pierce crystal oscillator [41]

1.6. Work Objectives

The objectives of this research in the thesis are as follows:

- Objective 1: To design and simulate a high-temperature oscillator circuit using Silicon Carbide (SiC) MOSFETs for operation in harsh environmental conditions with wide range of operation, focusing on the challenges of high temperatures and energy scavenging.
- Objective 2: To perform sensitivity analysis and Monte-Carlo simulations for the oscillator circuit, aimed at understanding the impact of component variations and temperature fluctuations on the circuit's performance and reliability.
- Objective 3: To validate the designed oscillator circuit through fabrication and experimental testing across a broad temperature spectrum, ensuring its stability and performance under high temperature conditions.
- Objective 4: To investigate the feasibility of using thermoelectric generators as a power source for the oscillator circuit, demonstrating the circuit's capability for energy scavenging in harsh environments.

- Objective 5: To explore the oscillator's capability for remote wireless sensing in high-temperature industrial environments, validating its application for real-time monitoring systems through successful wireless signal transmission and reception tests.

1.7. Organization of Thesis

This thesis is structured to provide a comprehensive journey from the initial motivation behind the study to the conclusive insights derived from the research conducted. Chapter 1 sets the context for the research by highlighting the importance of developing oscillator circuits capable of functioning in harsh environments and the relevance of energy scavenging in modern applications. Chapter 2 delves into the technical details of designing the Colpitts oscillator circuit. It covers the rationale behind choosing specific components and the methodology used in both the design and simulation processes. Sensitivity analysis and Monte-Carlo simulations are introduced to evaluate the impact of component variations on the circuit's performance. Chapter 3 details the physical assembly of the oscillator, including the selection of high-temperature compatible components and the experimental setup for testing the circuit's performance across a range of temperatures. Chapter 4 presents the experimental results obtained from testing the oscillator circuits. It compares these results with the simulations conducted in Chapter 2, discussing any discrepancies observed and their potential causes. This chapter also explores the circuit's capability for wireless signal transmission in high-temperature environments. Chapter 5 summarizes the key findings of the research, highlighting its contributions to the field of high-temperature electronics. It also suggests directions for future research to address the limitations encountered in this study and to explore new applications for the developed technology.

CHAPTER 2.

OSCILLATOR CIRCUIT DESIGN AND SIMULATION

2.1. Introduction

This chapter delves into the design and simulation of a high temperature oscillator circuit using a source-follower based Colpitts oscillator topology, covering design considerations and an analysis of the circuit. Circuit simulations and sensitivity analysis are used to analyze how the oscillator responds to variations in components and operating conditions. Montecarlo simulations were performed to evaluate the effect of component variations on the oscillator's behavior from room temperature to 300°C.

The oscillator circuit and the wireless transmitter using it must function across a wide range of temperatures, even though the circuit components' parameters change with temperature. A circuit using as few components as possible is preferred to reduce the probability of malfunction with increasing temperature. A version of the Colpitts oscillator was selected for the work thesis due to its simple design with minimal component usage, which simplifies circuit assembly.

2.2. The Source Follower Based Colpitts Oscillator:

The Colpitts oscillator is well known for its frequency stability, high oscillating frequency, and low power operation [42]. The latter property allows for the circuit to be powered by thermoelectric generators. The Colpitts oscillator uses a tank circuit made of an inductor and two capacitors to set the frequency of oscillation. Different types of sensors can be used in the circuit, making it possible to adjust the oscillation frequency for data transmission.

Figure 10 shows the schematic of a Colpitts oscillator using a source follower amplifier. The source follower amplifier configuration was selected due to its very high input impedance, low output resistance, and a near unity open circuit voltage gain. The tank circuit in Figure 10 is formed by one inductor(L1) and two capacitors (C1 and C2). Capacitor C1 is used for the feedback, C2 is at the output and L1 is at the input. C3 and C4 are bypass capacitors and are significantly larger than C1 and C2 i.e. (C3, C4>>C1, C2). The tank circuit provides positive feedback whereas R_S provides negative feedback to the oscillator circuit. The drain current I_{DS} is influenced by the gate-to-source voltage drop V_{GS}, given by:

$$I_{DS} = \frac{1}{2}\mu_n C_{ox}\frac{W}{L}(V_{GS} - V_{tn})^2 \tag{4}$$

In equation (4), V_{tn} is the threshold voltage for the n-channel device, $\mu_n$is the electron mobility, Cox is the oxide capacitance per unit area, W is the width of the MOSFET, and L is the Length of the MOSFET.

The gate-to-source voltage for this circuit is determined by the gate bias network, the source resistor, and the drain current:

$$V_{GS} = V_G - I_{DS}R_S \tag{5}$$

The resistor RS introduces negative feedback, which helps stabilize I_{DS}. According to equation (5), V_{GS} must decrease if I_{DS} increases due to any factor, as V_G remains constant. Consequently, this decreases in V_{GS} leads to reduction in I_{DS}. The presence of R_S ensures that I_{DS} remains as constant as possible.

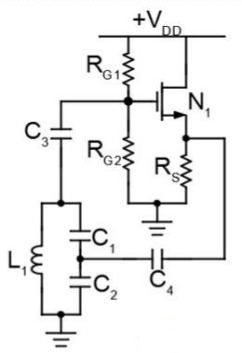

Figure 10: Source Follower Colpitts Oscillator

2.3. Design Modification to Ensure Wide Voltage and Temperature Operating Ranges

Discrete transistor source follower circuits are typically biased with a voltage divider at the gate, as shown in Figure 10. It was originally intended to power the oscillator circuit directly from thermoelectric generators. As the output voltage of the TEGs is proportional to the temperature and it was desired to turn on the circuit at low a temperature as possible, resistor R_{G2} was removed from the circuit, as shown in Figure 11. With this modification, the DC bias gate voltage is always equal to the supply voltage, $V_{G,Q} = V_{DD}$. The transistor will turn on as soon as $V_{DD}(T) > V_{tn}(T)$. This modification has the added benefit of reducing component count and therefore a potential point of failure.

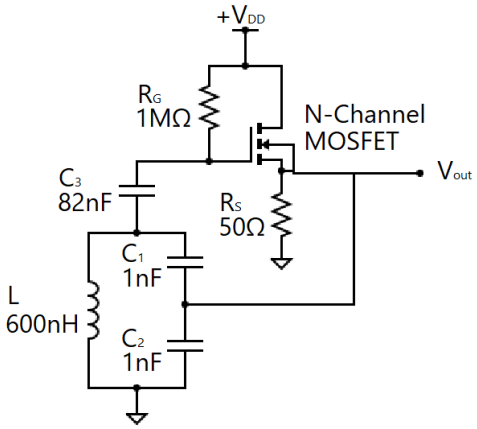

Figure 11: Simplified source-follower Colpitts oscillator circuit [38].

However, the bias resistors R_{G1} and R_{G2} are essential for maintaining a stable gate voltage (V_G), which ensures that the MOSFET operates at a fixed point on its characteristic curve. This is particularly advantageous in applications where the power supply stability and operating range are not limiting factors. Removing R_{G2} enables a broader operating range for MOSFET, but this comes at the cost of reduced control over the gate voltage. Consequently, the MOSFET's performance may become more susceptible to variations in the supply voltage V_{DD}.

2.4. Small-signal Analysis of the Colpitts Oscillator.

A small-signal analysis of the Colpitts Oscillator was performed to understand the conditions required for the oscillators to start and maintain oscillation and to determine the frequency of oscillation. Both closed loop and open loop analysis were performed.

2.4.1. Closed loop analysis

Closed-loop analysis is performed to determine the gain magnitude and phase conditions at oscillation. First, a simplified case was analyzed where the values of R_G, C_3 and the MOSFET's parasitic capacitances and output resistance (r_O) were such that they could be ignored. The small signal model for this case is shown in Figure 12.

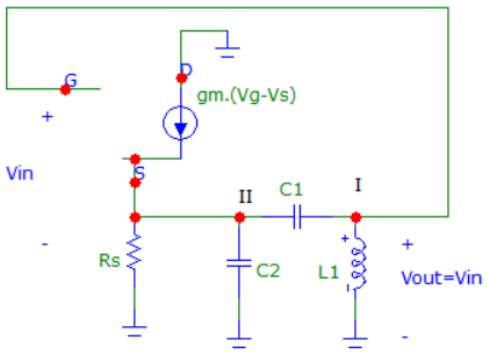

Figure 12: Simplified closed-loop small signal model of the circuit.

There are two independent nodes, marked I and II, in the circuit. At node I:

$$\frac{V_{in} - 0}{\mathrm{j}\omega L_1} + (V_{in} - V_S).\mathrm{j}\omega C_1 = 0 \tag{6}$$

At node II:

$$\frac{V_S}{R_S} + Vs.j\omega C_2 + (V_S - V_{in}).j\omega C_1 - g_m(V_{in} - Vs) = 0 \tag{7}$$

Combining these two equations, we obtain:

$$V_S\left(\frac{\omega^2 L_1 C_1 - 1}{\omega^2 L_1 C_1}\right)[1 + g_m R_S + j\omega(C_1 + C_2).R_S] - Vin(g_m R_S + j\omega C_1 R_S) = 0 \tag{8}$$

The gain condition is obtained setting the real part of Equation 8 to zero:

$$\omega^2 L_1 C_1 = 1 + g_m R_S \tag{9}$$

The oscillation frequency is obtained setting the imaginary part of Equation 8 to zero:

$$\omega = \frac{1}{\sqrt{L_1 C_T}} \tag{10}$$

Where $C_T = \frac{C_1 C_2}{C_1 + C_2}$. The gain condition for oscillation is thus:

$$g_m R_S = \frac{C_1}{C_2} \tag{11}$$

While the above analysis assumed that the MOSFET's gate-to-source capacitance, C_{gs}, could be ignored, the actual power MOSFET used in this circuit has large C_{gs} values. The closed-loop circuit including C_{gs} is shown in Figure 13.

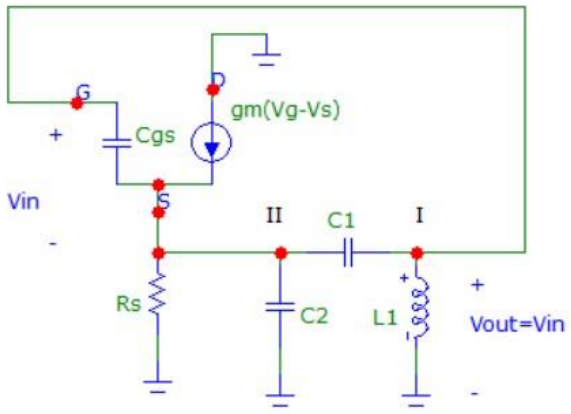

Figure 13: Closed loop model of the circuit including Cgs.

At node I:

$$\frac{V_{in}}{j\omega L_1} + (V_{in} - Vs)(j\omega C_1) + (V_{in} - Vs)\left(j\omega C_{gs}\right) = 0 \tag{12}$$

Now, nodal equation at II,

$$\frac{Vs}{Rs} + V_S.j\omega C_2 + (V_S - V_{in})j\omega C_1 + (V_S - V_{in}).j\omega Cgs - g_m(V_{in} - V_S) = 0 \tag{13}$$

From Equations 12 and 13

$$V_{in}\left[\frac{\omega^2 L_1\left(C_1 + C_{gs}\right) - 1}{\omega^2 L_1\left(C_1 + C_{gs}\right)}\right]\left(1 + g_m + j\omega\left[C2 + \left(C_1 + C_{gs}\right)\right]\right) - Vin\left(g_m Rs + j\omega\left(C_1 + C_{gs}\right)Rs\right) = 0 \tag{14}$$

Setting the real part of Equation 14 to zero,

$$\omega^2 L_1\left(C_1 + C_{gs}\right) = 1 + g_m Rs \tag{15}$$

Setting the imaginary part of Equation 14 to zero,

$$\omega = \frac{1}{\sqrt{L_1 C_T}} \tag{16}$$

Where $C_T = \frac{(C1+C_{gs}).C2}{(C1+C_{gs})+C2}$

Equation 16 gives the expression for frequency of oscillation. The gain condition for oscillation is obtained by combining Equations 15 and 16:

$$g_m Rs = \frac{C1+C_{gs}}{C2} \tag{17}$$

2.4.2. Open Loop Analysis

In the open loop analysis, the feedback loop of the system is opened or broken at a certain point and the system is analyzed as if there is no feedback. The main goal is to determine the transfer function of the system, which describes the relationship between the input and output in the frequency domain. It can be used to determine the dominant frequency and phase of the oscillator circuit.

The open-loop analysis of the circuit was performed including the loading due to R_G and C_3, which were considered to be large enough to be negligible in section 2.4.1. Also, the

MOSFET's parasitic capacitances (C_{gs} and C_{ds}) and the output resistance(ro) were considered for more accurate model. The feedback loop of the oscillator circuit was broken at the gate terminal. The input signal was applied to the gate terminal, i.e Vg=Vin. The gate-to-source voltage (Vgs) of a MOSFET can be determined by subtracting the source voltage (Vs) from the gate voltage (Vg), and the output was measured across R_G as indicated in Figure 14.

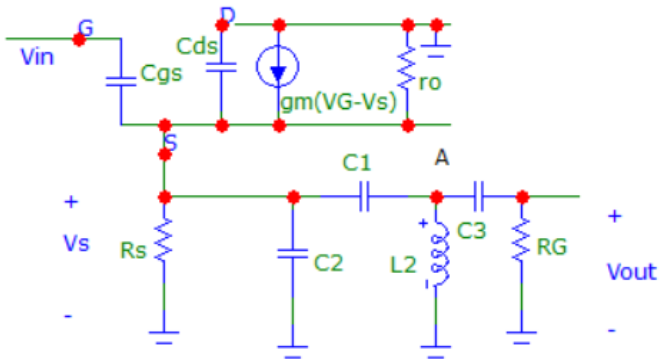

Figure 14: Detailed Open Loop Model of the Circuit

Node equation at Node S,

$$\frac{V_s}{Rs}+\frac{V_s}{\frac{1}{j\omega C2}}+\frac{V_s-V_A}{\frac{1}{j\omega C1}}+\frac{V_s}{\frac{1}{j\omega Cds}}+\frac{V_s}{ro}+\frac{Vs-V_{in}}{\frac{1}{j\omega Cgs}}-gm(V_{in}-V_s)=0 \tag{18}$$

Node equation at node A,

$$\frac{V_A}{j\omega L_1}+\frac{V_A-Vs}{\frac{1}{j\omega C1}}+\frac{V_A-Vout}{\frac{1}{j\omega C3}}=0 \tag{19}$$

Node equation at output node,

$$\frac{Vout}{R_G} + \frac{Vout - V_A}{\frac{1}{j\omega C3}} = 0 \tag{20}$$

MATLAB and its symbolic toolbox were used for this analysis. Nodal equations 18-20 were transcribed in MATLAB in s-domain and MATLAB's symbolic toolbox was utilized to solve the system of equations. Symbolic solutions were obtained for the nodal voltages and the system's transfer function was determined by taking the ratio of output voltage to the input voltage. The phase of the transfer function at each frequency point was determined using the 'atan2d' function. Next, the resonance frequency of the circuit was determined by identifying the frequency at which the imaginary part of the transfer function is zero. The expressions for the gain $G(jw)$and phase $\phi(jw)$ of the transfer function as well as the frequency(f) are shown in Appendix A. Figure 15 shows the gain and phase plot obtained from the open loop model in MATLAB with the oscillation frequency of 7.8MHz with the gain margin of 7.4 dB.

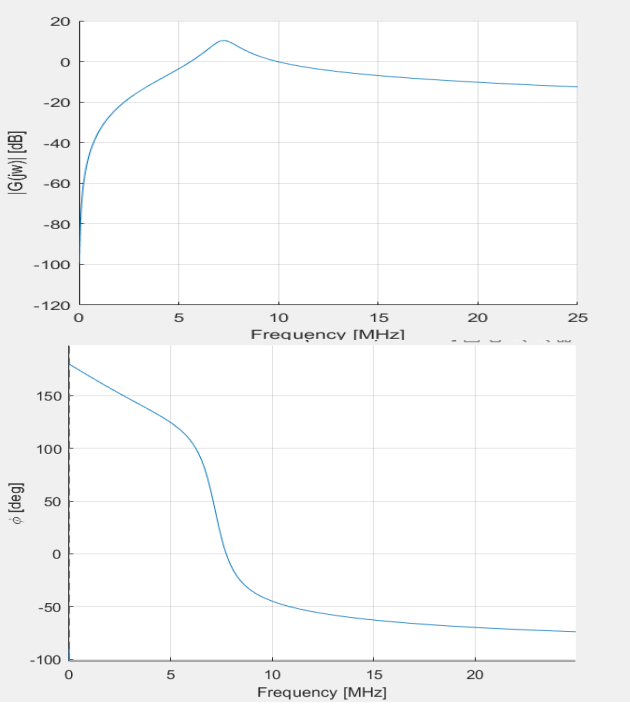

Figure 15: Open Loop Gain and Phase plot of the Oscillator from MATLAB

2.5. Component Value Determination

The determination of the component values for the Colpitts oscillator is guided by several considerations. The primary goal was to construct the circuit to operate within a frequency range of less than 10 MHz, due to the large internal capacitances of the SiC power MOSFET. The second consideration was the availability and cost of high-temperature components. For example, the largest valued capacitor rated for 500°C was 82 nF, with a cost of $100 per capacitor.

Due to their commercial availability, 1 nF capacitors were chosen for the feedback loop. The value of the inductor was determined accordingly, considering the resonant frequency for LC circuits. The decoupling capacitor C_3 would ideally have had a value larger than 1μF. However, the largest available value was 82 nF. Using the resonant frequency formula given by Equation 2.13, $L = 600\ nH$ was chosen.

The source resistance, R_S plays a crucial role, by setting the bias point and gain of the Colpitts oscillator. Equation 17 indicates that the value of R_S should neither be too high, which would result in a drop in gain, nor too low, which would limit its ability to provide the necessary feedback to stabilize the oscillator's output. The final value of R_S was determined experimentally by building the circuit on a breadboard and through simulations. The final value chosen was R_S.

The CREE SiC bare-die MOSFET CPM3-1200-0075A was chosen due to availability in bare-die format and lower capacitances than other bare-die SiC power MOSFETs that were available. The circuit schematic with component values is shown in Figure 11.

2.6. Circuit Simulations

The oscillator circuit was simulated using Micro-Cap simulation software version 12. Both the closed-loop and the open-loop configurations were studied to evaluate the performance and

understand the behavior of the oscillator circuit. The SPICE model for the CMP3-1200-0075A SiC MOSFET was provided by CREE. The use of this SPICE model allowed for a more accurate representation of the MOSFET's behavior in the circuit simulations compared to the small signal analysis in section 2.4.

2.6.1. Closed loop simulation

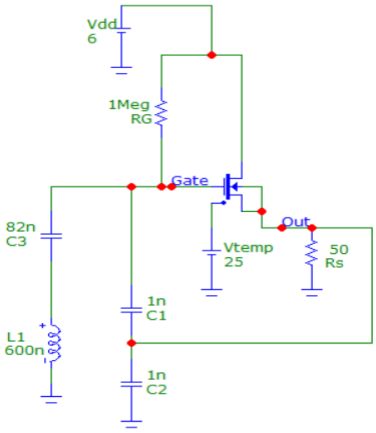

Figure 16: Source follower Colpitts Oscillator in Microcap

The closed-loop schematic used for transient simulation to determine oscillation frequency is shown in Figure 16. The transient analysis provides a time-domain view of the oscillator's output voltage. The result obtained from the transient analysis showed a sustained sinusoidal oscillation at the output of the oscillator, indicating the successful operation of the oscillator circuit, as shown in Figure 16. Figure 17.a shows the start-up transient. It takes approximately 22 µs for the oscillation to reach a steady state with stable peak to peak voltage of $V_{pp} = 2.68\ V$ and Figure 17.b shows the zoomed in section of the output.

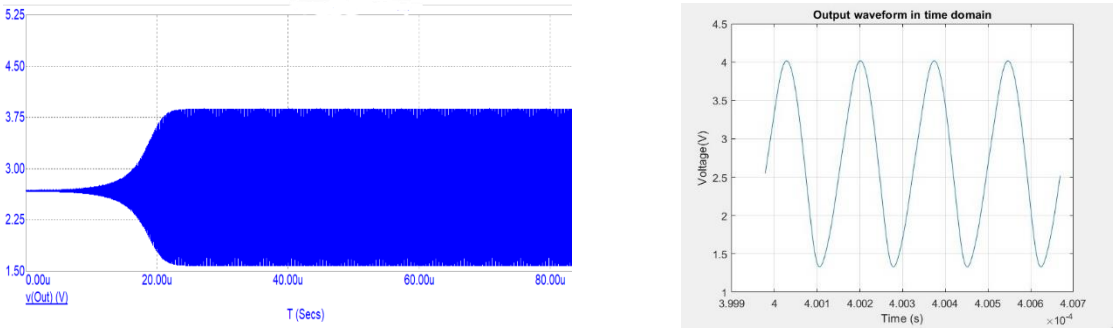

Figure 17:a) transient simulation, 0<t<80 µs b)zoomed section of output, 400 µs <t<400.6 µs

A Fast Fourier Transform (FFT) of the output signal performed to determine the oscillation frequency, view of the frequency components present in the output signal, shown in Figure 18.

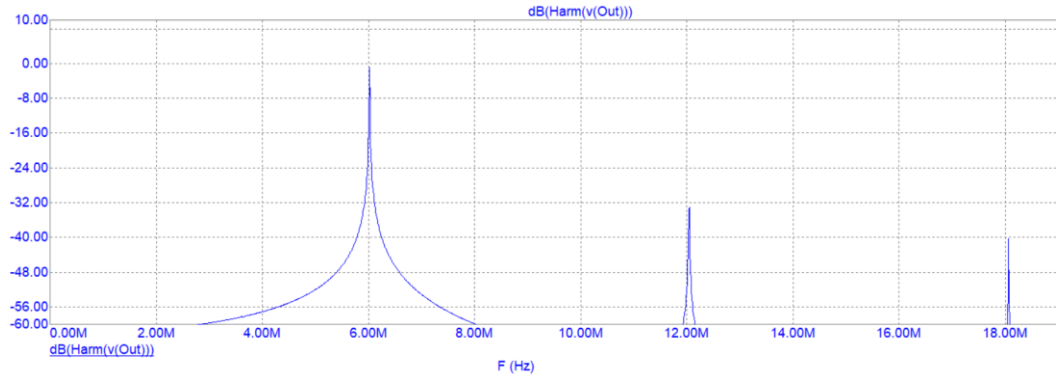

Figure 18: FFT of the Oscillator's Output Voltage

The FFT showed a prominent peak at 6.020 MHz which is at -0.8 dBV. The second and third harmonics at 12MHz and 18 MHz are also seen in the frequency spectrum, indicating a distortion of the output signal. However, their amplitudes are more than 32 dB below the fundamental, which indicates the energy present at these harmonics is weak compared to the fundamental frequency.

2.6.2. Open loop simulation:

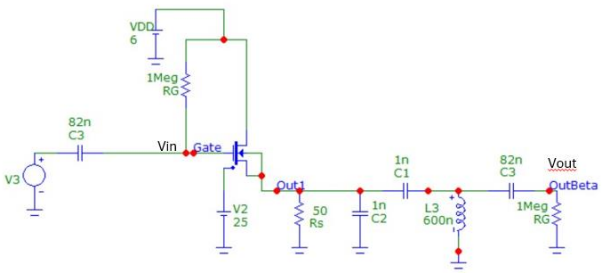

Figure 19: Open loop model in Micro-Cap

The simulation schematic is shown in Figure 19. An AC analysis was conducted, with the input applied to the gate of the transistor. The open loop gain magnitude and phase responses of the oscillator are shown in Figure 20. These two responses offer critical insights into the operational characteristics of the oscillator, particularly its resonant frequency and stability. The resonant frequency of the oscillator is the frequency at which the phase shift is 360 degrees, as long as the gain magnitude at that frequency is greater than or equal to 0 dB. From Figure 20, it can be seen that the oscillation frequency is approximately 8 MHz with the gain margin of 6.5dB

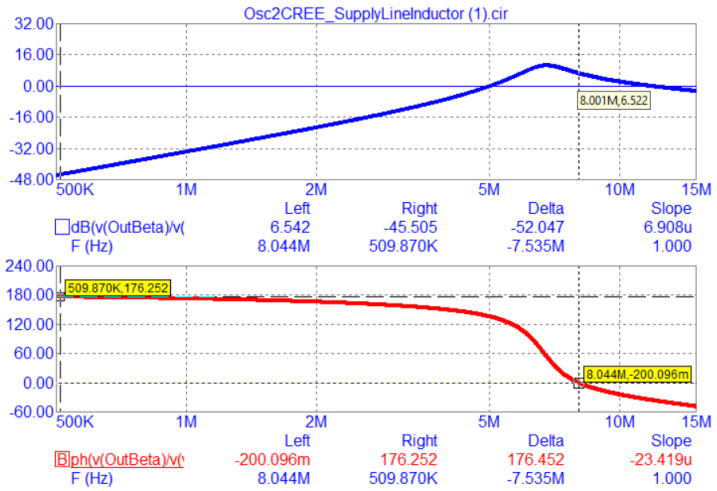

Figure 20: Open loop gain and phase of the oscillator.

The observed discrepancy between the open-loop and closed-loop simulation frequencies—6 MHz and 8 MHz respectively—can primarily be attributed to the incomplete modeling of the MOSFET's parasitic capacitances in the load circuit of the open-loop model. Although the Microcap model accounts for these parasitics, their effects on the output were not incorporated. This oversight affects the accuracy of the simulation by altering the impedance seen by the circuit, which is critical for assessing the frequency response and stability of the oscillator. Properly accounting for these capacitances at both the input and output in the open-loop model would help in achieving a closer alignment between the simulated and actual operational frequencies.

2.7. Sensitivity analysis

2.7.1 Sensitivity: The Bode Perspective

In control system analysis, sensitivity as a concept was introduced by Bode [41] to quantitatively express how system performance varies with changes in system parameters. It is defined as the relative change in a system's output for a relative change in its input or parameter. the sensitivity, S, of a system's output, y, to a system's parameter, p, is given by.

$$S_p^y = \frac{\delta y/y}{\delta p/p} = \frac{p}{y}\frac{\delta y}{\delta p} \tag{21}$$

In Equation 21, $\frac{\delta y}{\delta p}$ is the partial derivative of the system's output with respect to the parameter p. Positive sensitivity indicates that the output increases with an increase in the parameter, while a negative sensitivity means that the output decreases with an increase in the parameter.

2.7.2. Sensitivity Analysis of the Source Follower Colpitts Oscillator

Sensitivity analysis was applied to evaluate the impact of varying values of the components C_1, C_2, L_1, C_{gs}, C_{ds} and g_m on the frequency of the source follower based Colpitts oscillator. This

evaluation was accomplished using a MATLAB script using the frequency expression obtained in section 2.4.2. The MATLAB code for sensitivity analysis employs partial derivative calculations for each of the circuit components with respect to frequency which indicates how much frequency changes as each component values are slightly altered. This code is given in appendix B.

Normalized sensitivity for each component was then calculated by multiplying the ratio of component value to frequency by the corresponding partial derivative which gives the measure of relative change in frequency for a relative change in the component value.

2.7.3. Results and Interpretation

The analysis output, represented as a bar graph, is shown in Figure 21. This gives a visual representation of the oscillation frequency sensitivity to all the components in the circuit. From the Figure, it can be observed that inductor L_1 showed the highest sensitivity of -0.5, signifying that the frequency of the oscillator is most influenced by variations in the inductor value. Among the capacitors, the oscillation frequency shows a higher sensitivity to C_1, (-0.35) compared to C_2 (-0.08). It is also slightly more sensitive to the gate-source parasitic capacitance (C_{gs}) of the SiC MOSFET, with a sensitivity of -0.09, compared to C_2. This is primarily due to the influence of large gate-source (C_{gs}) parasitic capacitance of the SiC MOSFET. In contrast, the oscillation frequency demonstrated relatively low sensitivity to both C_{ds} and g_m.

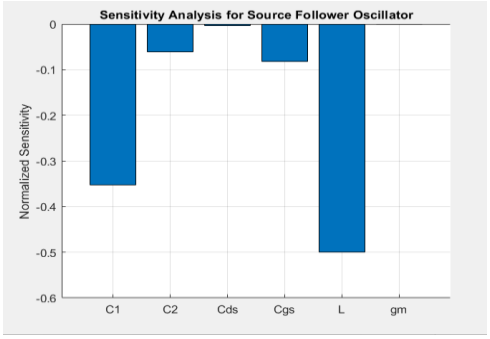

Figure 21:Sensitivity analysis of oscillation frequency to circuit components.

Sensitivity analysis helped identify the most critical components influencing the oscillator's frequency. The oscillation frequency was found to be most sensitive to variations in inductor L_1 and capacitor C_1. Also, negative sensitivities indicate that an increase in the values of the components would cause a decrease in the frequency and vice versa.

While the model effectively captures static sensitivity, it cannot reflect the dynamic sensitivity, which includes time-varying behaviors and interactions under changing operational conditions. Despite this limitation, models remain crucial for initial design and stability analysis as it helps prioritize component selection and predict the behavior under component value changes.

2.8. Monte-Carlo Simulation

Monte Carlo analysis is a powerful statistical technique used to understand the impact of risk and uncertainty in prediction and modeling. Montecarlo simulations were used to analyze the variability of the oscillator circuit's performance, including frequency and output voltage magnitude considering the tolerances of components and temperature variation. Monte Carlo analysis was done in two ways. The first was using Micro-Cap simulation software and the second was using MATLAB with the open loop model discussed in 2.4.2.

2.8.1. Montecarlo simulation in Micro-Cap

The Montecarlo simulations in Micro-Cap were carried out on the closed-loop oscillator circuit shown in Figure 22. In the simulations, the tolerance of passive components was based on datasheet specifications. The resistors and capacitors were varied by ±5%. The inductors, which were fabricated in-house, were assigned a wider tolerance range of ±20% in order to account for the variations in the fabrication process. As mentioned previously, a SPICE equivalent circuit model was provided by CREE for its CPM3-1200-0075A. This model allowed for the adjustment of the MOSFET's junction temperature (Tj) using a voltage source. Furthermore, the passive

component values were also adjusted based on information from the datasheets as well as experimental measurements. High temperature resistor characterization data was used to determine the resistor value at each temperature while capacitors were adjusted as per the data sheet. For the Monte Carlo simulations, 100 runs were performed at each temperature. During each run, Micro-Cap randomly varied the component values according to the Gaussian distribution model. In the following, the results from the Monte Carlo analysis in Micro-Cap will be discussed, focusing on how changes in the temperature and component values affect the frequency and the output voltage magnitude (the peak-to-peak voltage VPP) of the oscillator. The results are presented in the form of histograms.

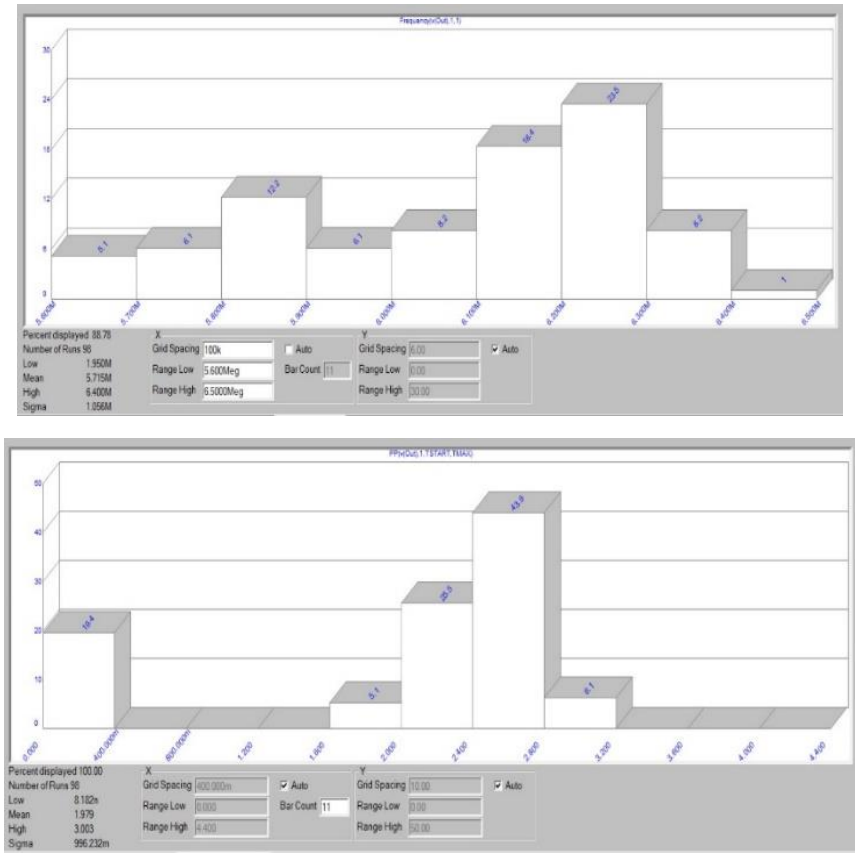

Figure 22. a) Histogram of Frequency variations (Top) b) Histogram of VPP variation at Room Temperature (Bottom)

The first analysis was done at room temperature (25°C). The histogram, shown in Figure 23.a, revealed a frequency distribution that varied from minimum of 5.6 MHz to maximum of 6.4MHz, with a mean of 6.04 MHz and standard deviation of 0.274MHz. The histogram shown in Figure 23.b, indicated a peak-to-peak voltage (VPP) distribution centered around 2.5 V, with a standard deviation of 0.288 mV. Failure rate: About 12.5% of the simulation runs failed to oscillate at room temperature.

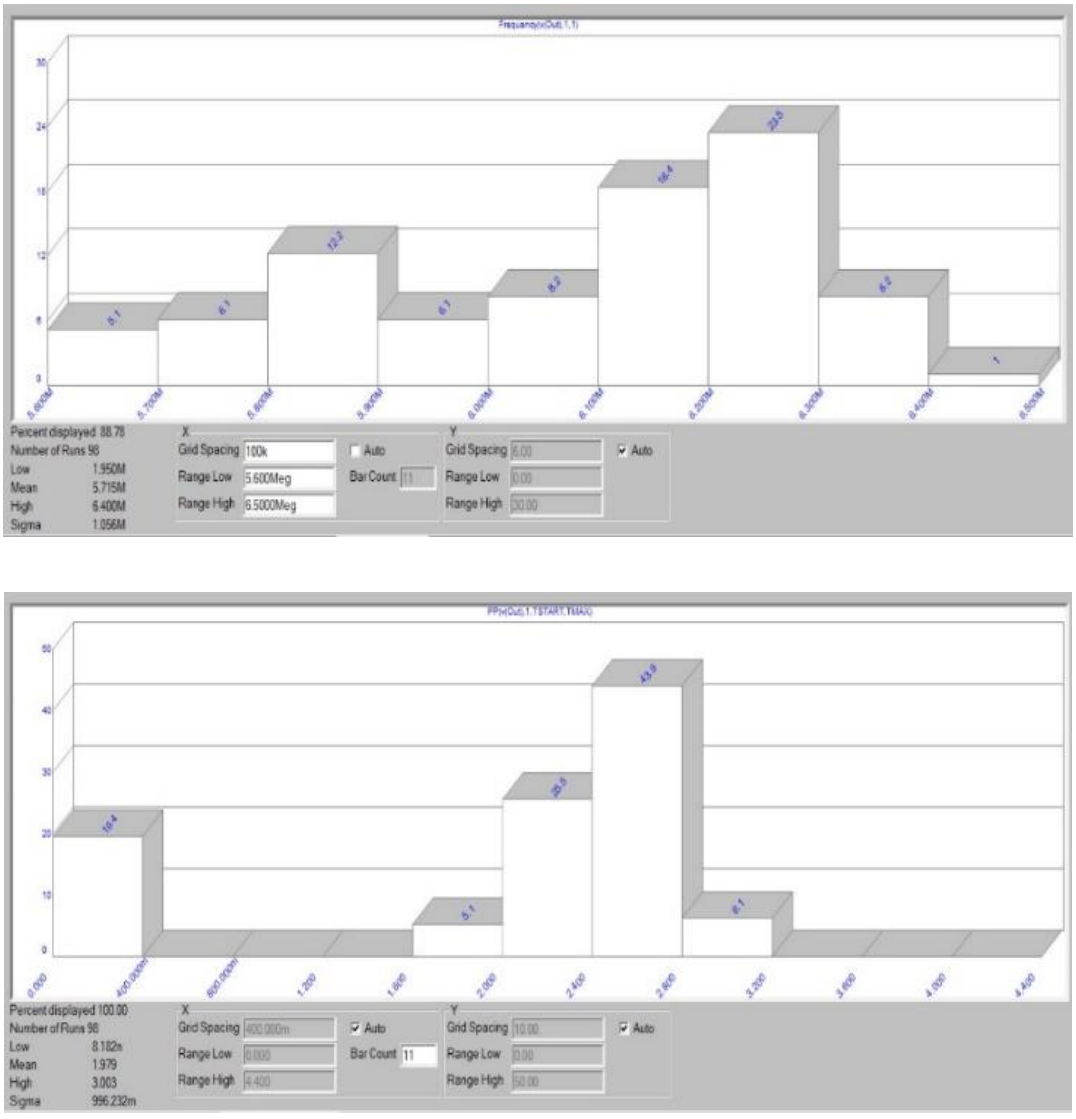

Figure 23. a) Histogram of Frequency variations (Top) b) Histogram of VPP variation at Room Temperature (Bottom)

The analysis was repeated at 100 ℃, 200 ℃ and 300 ℃. The histograms for 100 ℃ are shown in Figure 24. The frequency distribution varied from minimum of 5.8 MHz to maximum of 6.7MHz, with a mean of 6.19 MHz and standard deviation of 0.214MHz, while the peak-to-peak output voltage distribution centered around 2.834 V, with a standard deviation of 0.213 V. About 7.5% of the simulations failed to oscillate at 100 C.

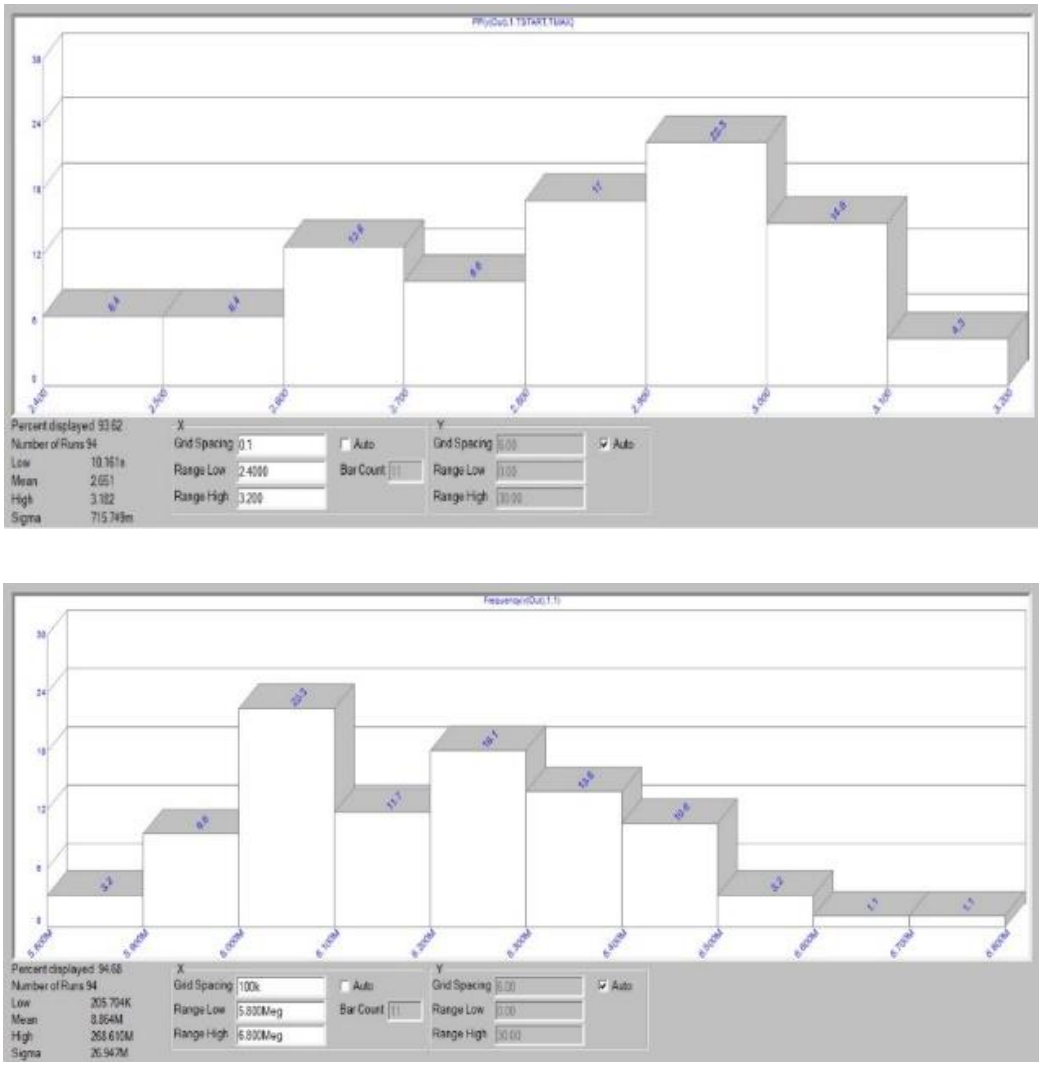

Figure 24 a) Histogram of Frequency variations (Top) b) Histogram of VPP variation at 100° C(Bottom)

The histograms for 200 ℃ are shown in Figure 25. The frequency distribution is centered around 6.852 MHz, with a standard deviation of 255 KHz, while the peak-to-peak output voltage

distribution is centered around 4.28 V, with a standard deviation of 0.11 V. 100% of these simulations were successful.

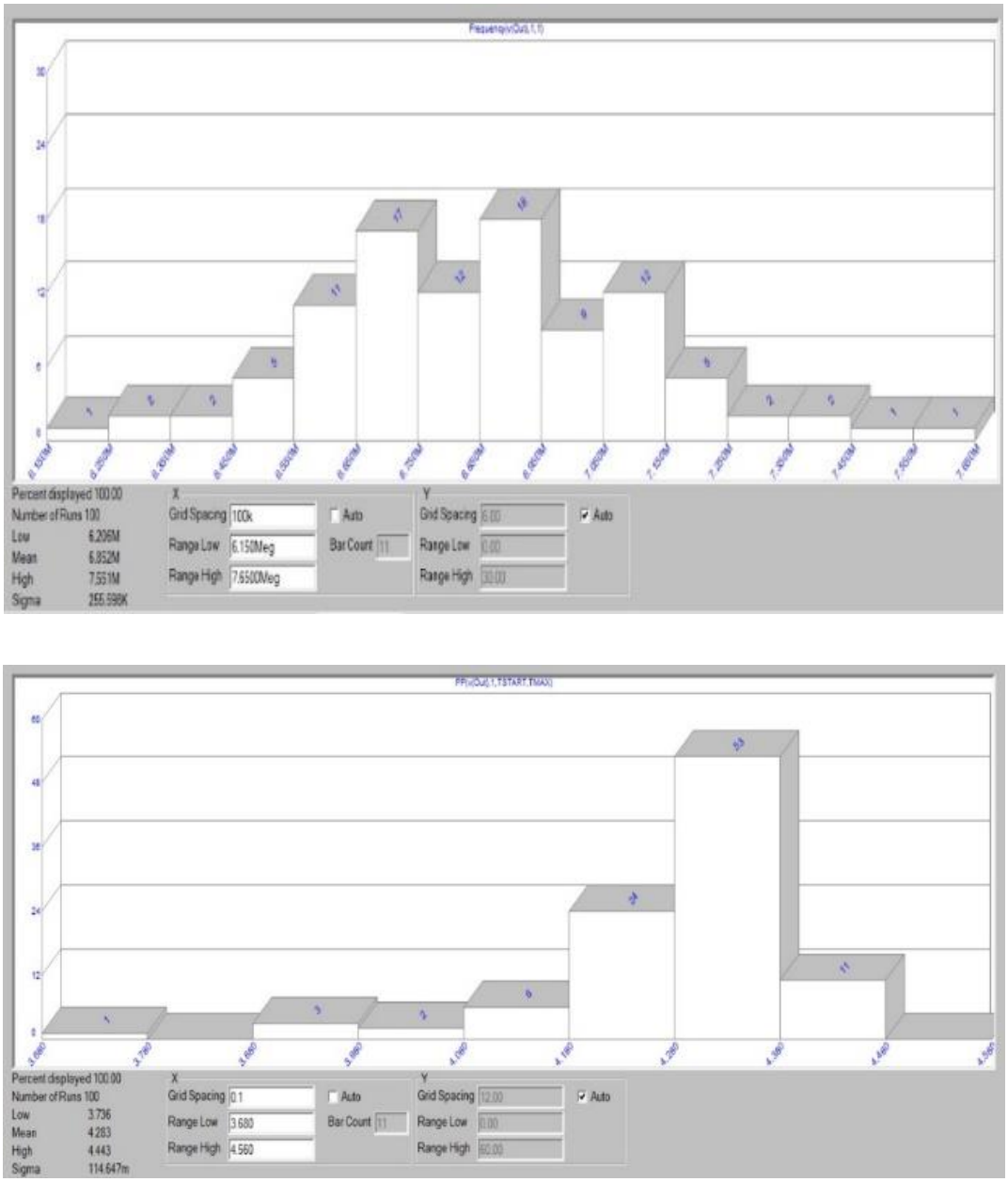

Figure 25 a) Histogram of Frequency variations (Top) b) Histogram of VPP variation at 200℃(Bottom)

The histograms for 300 ℃ are shown in Figure 26. The frequency distribution rangws from 6.1 to 8.1 MHz, centered around 6.9 MHz, with a standard deviation of 448KHz. The peak-

to-peak output voltage distribution is centered around 4.55 V, with a standard deviation of 0.1 V. 100% of these simulations were successful.

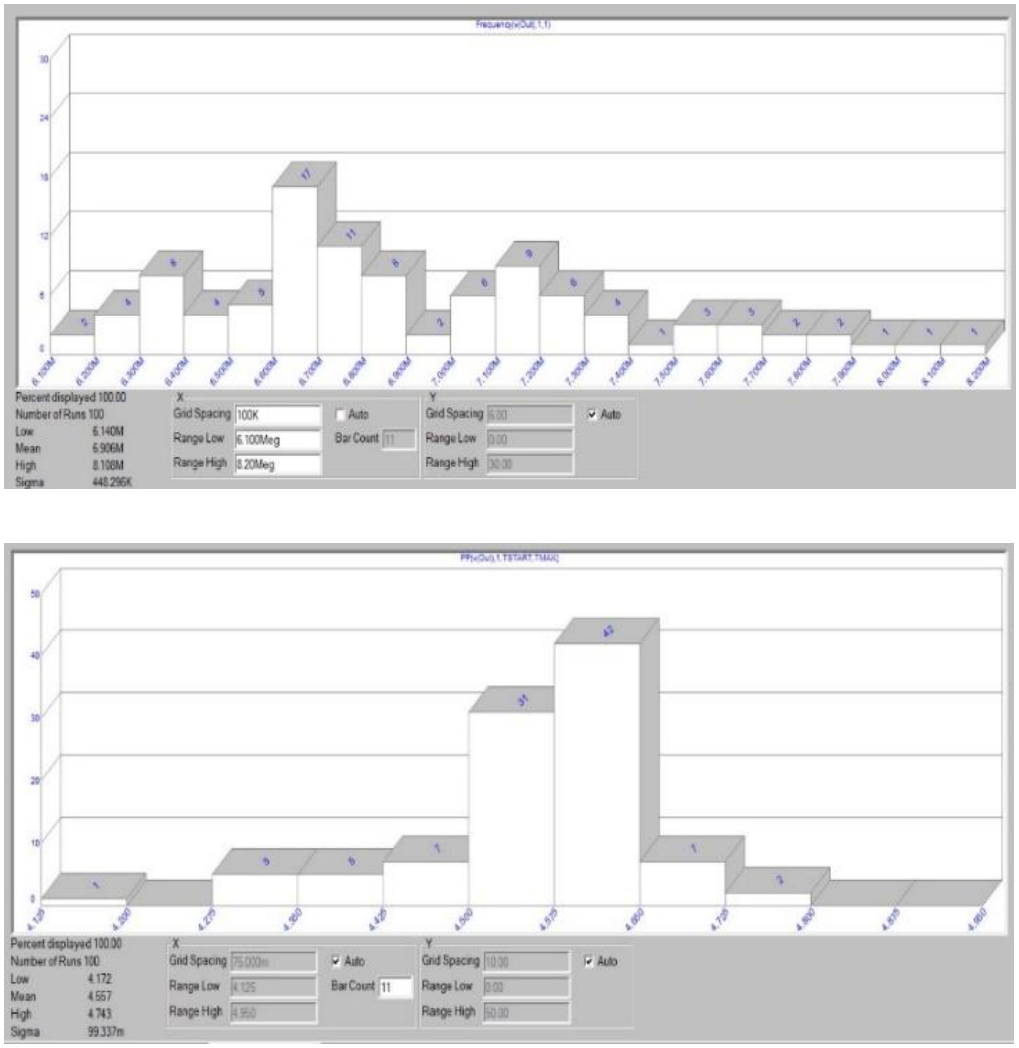

Figure 26. a) Histogram of Frequency variations (Top) b) Histogram of VPP variation at 300°*C* (Bottom)

The histograms obtained from Micro-Cap show a wide distribution in oscillation frequency and output magnitude as the component values vary within the specified tolerance range. It also can be noticed that with the increase in temperature the frequency and peak to peak voltage also increased. However, the simulations indicated that at lower temperatures, the oscillator more frequently failed to meet the conditions necessary for oscillation. Therefore, the results from the

Montecarlo simulations from microcap must be viewed with caution due to inherent limitations in the modeling tools used. The microcap model employed for these simulations is rated for use only up to 125 °C. Given this limitation simulations conducted above 125 °C may not accurately reflect the true behavior of oscillator under such conditions. Also, since the MOSFET equivalent circuit model could not be altered, the parameters describing MOSFET's dynamic and static characteristics did not have any tolerances assigned. Additionally, the simulations were run 100 times at each temperature, providing limited insights. Ideally, thousands of simulations would be necessary for a thorough distribution analysis. Therefore, this result needs to be validated through experimental testing.

2.8.2. Monte Carlo simulations using MATLAB:

Monte Carlo analysis at room temperature was also conducted using MATLAB and evaluation the frequency response of the circuit was done under room temperature conditions. The source follower Colpitts oscillator circuit's open loop model as designed in section 2.5 was taken in MATLAB, with component values defined using symbolic variables. The small signal model was utilized to express the circuit's frequency response as a function of these variables, incorporating parameters such as C_{gs}, C_{ds}, g_m, R_G, L_1, C_1, C_2, C_3 and were defined in the script which is given in Appendix C. The tolerances for resistors and capacitors were chosen to be 5%, and 20% for the inductors as done in section 2.8.1. In addition to that, the tolerances for the MOSFET parameters C_{gs}, C_{ds}, g_m, r_o were set to 20%. The simulations were run 1000 times, randomly varying the component values within the specified tolerance ranges using a Gaussian distribution.

The frequency response values obtained from each simulation were used to generate a histogram, visualizing the distribution of frequency of oscillation from each simulation run

conducted at room temperature. Figure 27 displays the histogram of frequency obtained from the Montecarlo simulation which shows the frequency distribution from 6.9 to 8.8 MHz with the mean of 7.7 MHz and standard deviation of 468 KHz.

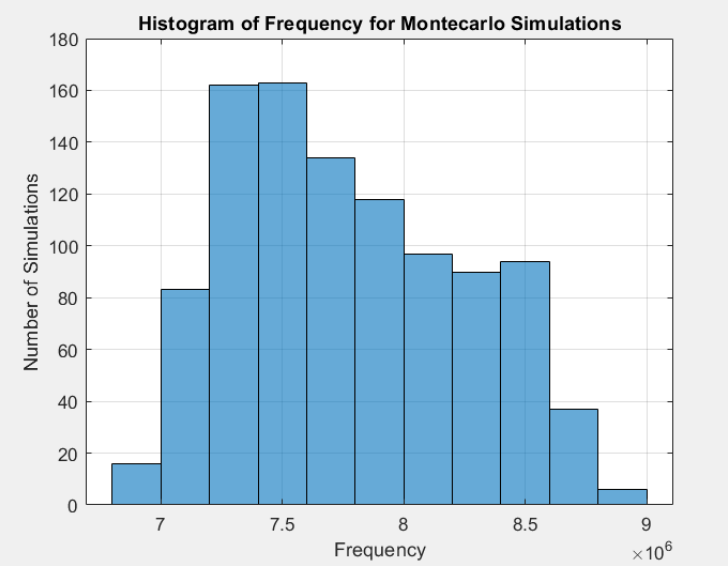

Figure 27: Histogram of Frequency at Room Temperature

2.9. Conclusion

This chapter has provided a comprehensive exploration into the design, simulation, and analysis of a high-temperature oscillator circuit, utilizing a source-follower based Colpitts oscillator topology. The chapter delved into critical design considerations, such as the circuit's ability to operate across a wide range of temperatures and the impact of component variations on performance, culminating in the adoption of a simple design approach to enhance reliability in high-temperature environments.

The design and modification of the oscillator to ensure wide voltage and temperature operating ranges were detailed, showcasing the practical aspects of engineering design in addressing real-

world challenges. Through small-signal analysis, the fundamental principles governing the oscillator's operation were elucidated, offering insights into the conditions necessary for stable oscillation and the determination of oscillation frequency.

Simulation results, encompassing both closed-loop and open-loop configurations, along with sensitivity, demonstrated the effectiveness of oscillator design. Also, discrepancies observed between the MATLAB and Microcap simulations can be attributed to modeling inconsistencies. The MATLAB model appears to be incomplete, as the gate-drain capacitance (C_{gd}) element is missing. Furthermore, the successful implementation of sensitivity and Monte Carlo analyses demonstrates the circuit's reliability and performance stability. However, it's important to note that the sensitivity analysis focused on component variations and did not extend to high-temperature effects, marking a limitation in sensitivity modeling.

The upcoming chapter pivots from the theoretical analysis and simulations to the practical fabrication and experimental setup of the oscillator circuit. This shift will allow for the comparison between the simulated behaviors with the measured performance of the circuit, highlighting the critical differences and insights gained from hands-on testing.

CHAPTER 3

OSCILLATOR FABRICATION AND EXPERIMENTAL SETUP

3.1. Introduction to the Chapter

Chapter 3 focuses on the fabrication and testing of the SiC Colpitts oscillator circuit, designed for high-temperature environments. It outlines the selection of components, like SiC MOSFETs and gold-plated alumina substrates, chosen for their durability and thermal resilience. The assembly process is detailed, highlighting techniques such as silk-screen printing for applying gold traces and wire bonding for connections.

The experimental setup described in this chapter tests the circuit across temperatures up to 400°C inside a furnace, using both standard power supplies and Thermoelectric Generators (TEGs). This setup aims to assess the oscillator's performance in extreme conditions, particularly its capability for wireless signal transmission—a critical feature for its application in remote wireless sensing.

3.2. Oscillator Component Selection & Design

3.2.1. Component Selection Criteria

The most important criterion for component selection is the capability to operate from room temperature to temperatures greater than 200°C. SiC MOSFETs are chosen as the active component in the circuit due to their high-temperature resilience. Gold-plated alumina substrates are used because gold offers very good conductivity, is resistant to corrosion, and has a melting temperature of 1064°C [43], providing a stable base for gold traces. Alumina, with its melting temperature of over 2030°C [44], serves as a robust base for these traces. Circuit components should be compatible with wire bonding for connections. The final criterion concerns the physical stability of the oscillator circuit. Passive components are attached to the circuit using epoxy paste

to ensure adhesion under high-temperature conditions. To facilitate high-temperature testing, Inconel cables are used between the power sources and the circuit. The following sections will elaborate on the component selection in detail.

3.2.2. Selection of Active Component

The most important criteria for transistor selection were capability of high temperature operation, commercial availability, and availability in bare die form. While the first is self-explanatory considering this work's focus on high-temperature electronics, the latter two need explanation. While a number of university research groups have demonstrated high-temperature SiC or GaN transistors [Insert references], these were custom manufactured for specific projects in university cleanrooms and are not available. Designing a SiC transistor and developing a manufacturing process is a multi-year process and beyond the scope of the present work. Therefore, commercially available transistors are required. Furthermore, these transistors need to be available in bare-die format. Commercial transistor packaging techniques are not compatible with operating temperatures above 300 ℃. Instead, gold bond wires need to be attached directly to the device. The selection of the active component, the bare-die SiC CPM3-1200-0075A MOSFET manufactured by Cree, was therefore crucial in the oscillator's design.

The CPM3-1200-0075A is a bare die n-channel enhancement type MOSFET, pictures of which are shown in Figure 28. It was chosen due to prior demonstration of high temperature operation [45]. This device is a power transistor with a maximum drain current rating of 7.5 A and a maximum drain-to-source voltage rating of 1200 V. Thus, this is a large area transistor with very large capacitances, as described below. This limits the maximum oscillation frequency, as will be discussed later. Unfortunately, a small-signal SiC MOSFET was not available. A second limitation

of this device is that it has aluminum bond pads. This limited the temperature range of the device, which will be discussed later.

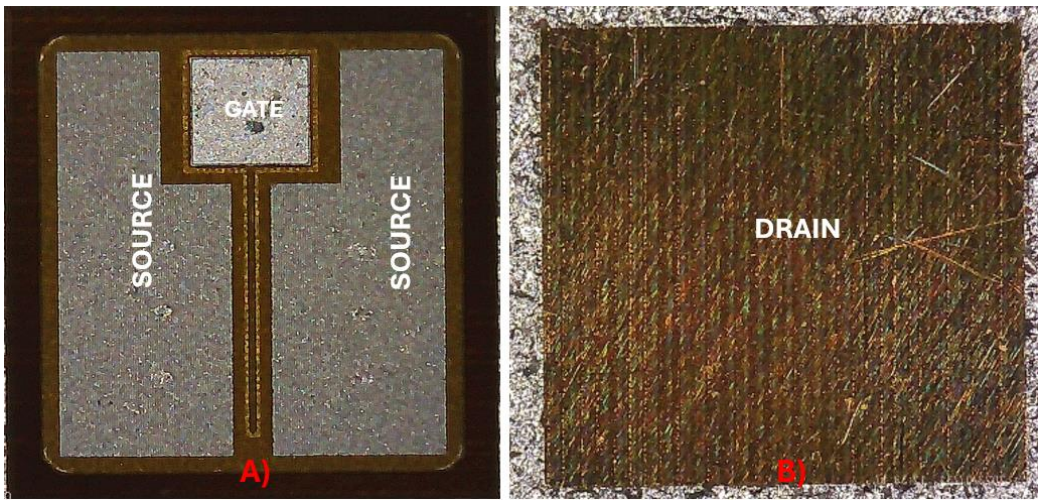

Figure 28: Pictures of the Cree CPM3-1200-0075A SiC Bare Die Power MOSFET taken in the RF Photonics Lab, UMaine: (a) top view showing the gate and source contacts; (b) bottom view, the entire back side is the drain contact.

According to the datasheet provided by Cree, the input capacitance (C_{iss}) is1390 pF, the output capacitance (Coss) is 58 pF, and the reverse transfer capacitance (Crss) is 2 pF. These values need to be translated to the gate-to-source (Cgs), gate-to-drain (Cgd) and drain-to-source (Cds) capacitances used in the circuit analysis presented in Chapter 2. The input capacitance is given by:

$$C_{iss} = C_{gs} + C_{gd} \tag{22}$$

The output capacitance is given by:

$$C_{oss} = C_{ds} + C_{gd} \tag{23}$$

The reverse transfer capacitance is equal to the gate-to drain capacitance given by:

$$C_{rss} = C_{gd} \tag{24}$$

Using equation 3.1-3.3, Cgd, Cgs and Cds were determined to be 2pF, 1388 pF and 56 pF, respectively. Figure 29 shows how these capacitances are connected to the transistor's terminals.

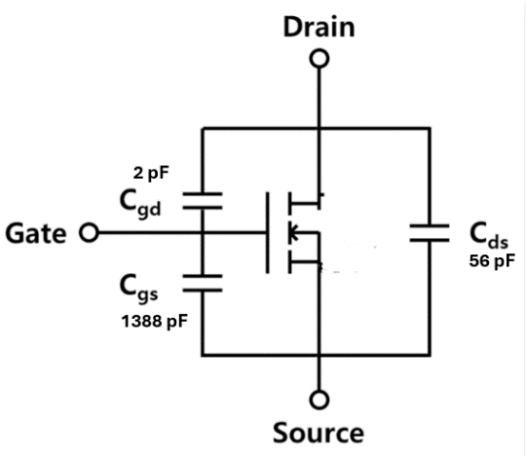

Figure 29: Model of the CREE MOSFET with parasitic capacitances [46]

3.2.3. Selection of High-Temperature Resistors and Capacitors

Vishay-Dale's surface mount chip resistors were selected due to the availability of large range of resistors and low cost. The surface mount chip design allowed for easy integration to the circuit through wire bonds. The highest operating temperature for these resistors was rated at 250°C. However, these resistors were operated up to 350°C in this work, with the protective covering degrading at temperatures above 300°C. The results of a high temperature characterization test of a 50 Ω Vishay-Dale resistor (PATT1206E1001BGT1), are shown in Figure 30. The change in resistance was less than 0.5% when tested from room temperature to 350 °C. For the oscillator design in this work, a gate resistor R_G of 1MΩ and a source resistor, R_S of 50 Ω were chosen as mentioned in Chapter 2.

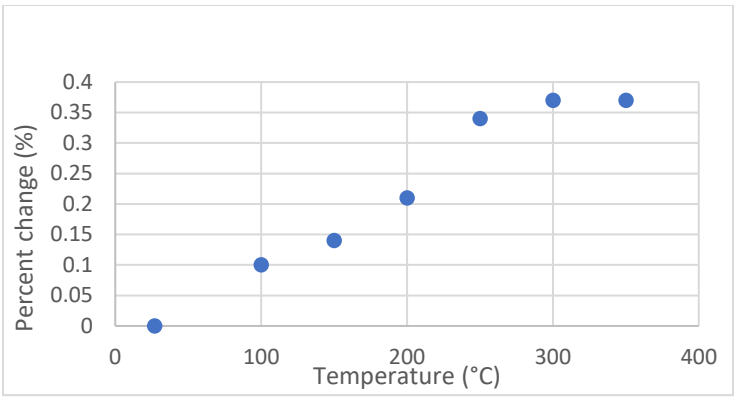

Figure 30: Resistance variation with temperature of a 50 Ω Vishay-Dale resistor compared to its room temperature value

For the capacitors, Presidio Component's high temperature ceramic capacitors were chosen due to their remarkable ability to withstand temperatures up to 500 °C. These capacitors were developed for NASA's Venus mission. According to the datasheet provided by Presidio Components [47], the temperature coefficient for the selected capacitor was nearly zero from -60°C to 300 °C, as shown in Figure 31. Although these capacitors come at higher cost and are available in a limited value range, their selection for the high temperature circuit was crucial.

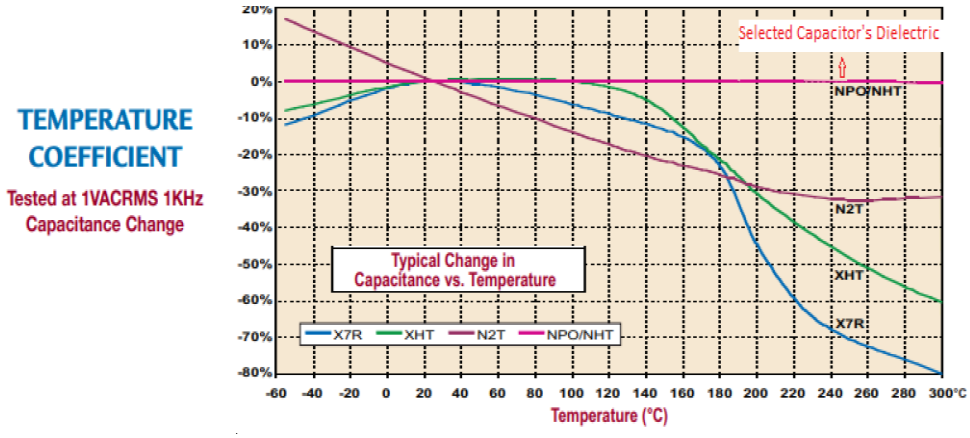

Figure 31: Temperature coefficient (shown in pink) for the selected capacitor's dielectric

3.2.4. Development of High Temperature Inductors

The design, fabrication and testing of high temperature inductors was one of the major tasks necessary for the fabrication of the high temperature oscillator circuit. This task was performed by my colleague Jude Zanoni as a part of his honor's thesis [48]. Circular shaped spiral inductors were fabricated directly on the alumina board using gold paste through a silk printing process.

Keysight's Advanced Design System (ADS) software and its Coilsys tool were used in the design and simulation of these circular spiral inductors. The inductors developed by Jude Zanoni were tested, with key results summarized in Table 3.2, detailing both the designed and measured inductance values. The error between the measured and design values ranged from 3.5% to 15.6%.

Table 1. Summary of Designed and Measured Inductance Values for High-Temperature Inductors *[48]*

Designed Inductance(nH)	Measured Inductance(nH)	Max Error (%)
100	84.4-85.4	15.6
400	386-402	3.5
600	525-573	12.5%
1000	976-986	6.7%

Any discrepancies in the application of the gold paste or potential spreading during the baking process could be responsible for the observed error. Also, discrepancies observed in inductor measurements may also result from the design process, which assumed a perfectly circular shape. However, the actual design, created using the Coilsys tool in ADS, incorporated numerous linear segments, leading to an imperfect circular form.

3.3. Circuit Fabrication

This section covers the fabrication processes of the circuit. First, an existing prototype oscillator circuit was modified by swapping components and changing bond wire connections. After initial testing of this circuit, a dedicated mask was designed for this oscillator.

3.3.1. Modification of an Existing Circuit

The first phase of the experiments involved modifying a Pierce oscillator circuit designed and built by Mr. Jonathan Kinkaid and Mr. Qingsong Cui, former research associates at (Frontier Institute of Research for Sensor Technologies) FIRST at University of Maine. This Pierce oscillator design worked in a narrow temperature range due to the bias point shifting with temperature. As a preliminary experiment to verify the functioning of the current Colpitts oscillator design, modifications were made to bond wire connections to convert the Pierce oscillator to the Colpitts oscillator. Several components were removed, and a source resistor was added. This modified layout is shown in Figure 32.

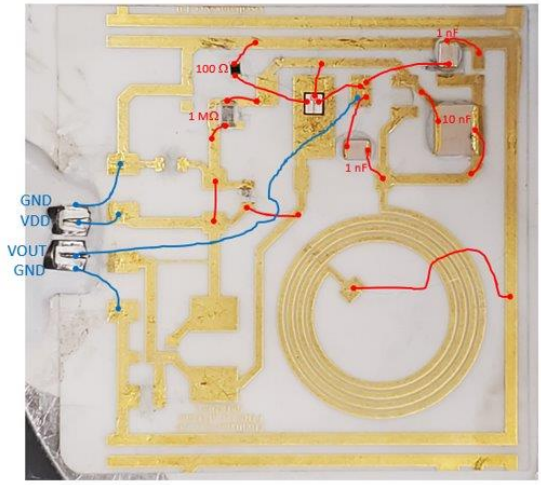

Figure 32: Modification to the existing Pierce oscillator design

It became evident from testing that there were issues with the wiring and component placement. For example, one noticeable drawback was the lengthy bond wire connecting the circuit's output to the Inconel Cable, shown as a long blue line in Figure 32. This long wire has the potential to sag and short-circuit at high temperatures, as well as causing parasitic coupling. Once the functioning of the circuit at high temperatures was verified, a new layout was designed.

3.3.2. Design and Fabrication of a Reconfigurable Layout for the Colpitts Oscillator

Upon the successful operation of the modified circuit, a layout for the Colpitts oscillator circuit was designed by Conlan Taylor, a participant in the NSF funded Research Experiences for Undergraduates Site: Sensor Science and Engineering. The inductors were designed by Jude Zanoni. The circuit layout, shown in Figure 33.a, was created in AutoCAD. The circuit has 4 spiral inductors, with values of 400nH, 600nH, 800nH and 1000nH. This allows reconfiguring the circuit to oscillate at different frequencies. The circuit's oscillation frequency is set by connecting the desired inductor to the circuit via gold bond wires. The inductors can be connected in series or parallel as well, to obtain other inductance values. Two copies of this circuit were fabricated, which were called the Alpha and Beta circuits.

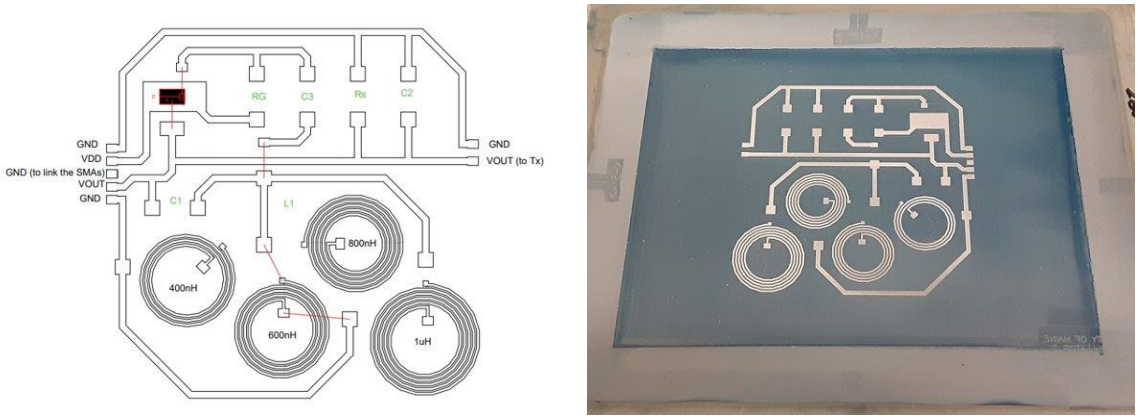

(a) (b)

Figure 33: a) Reconfigurable Layout Design in AUTOCAD b) Stencil for Fabrication of Reconfigurable Circuit Layout

The circuits were fabricated on alumina substrates, due to alumina's robust thermal properties. The circuit pattern was realized by employing a silk screen printing method using gold traces. Specifically, the Heraeus C5729 gold paste was used. Gold was chosen for its excellent electrical conductivity and resistance to corrosion and oxidation. In this process, a stencil of the circuit layout was first created as shown in Figure b, with the circuit design being transferred onto a screen. This screen was then placed over the alumina substrate, and the gold paste was applied over the screen at an angle of 45° using a squeegee. The openings in the stencil allowed the gold paste to be deposited onto the alumina substrate in the desired pattern. After the gold paste was applied, it was allowed to set for 15 minutes. It was then dried at 150 °C for 10 minutes. The substrate then underwent a firing process at 850 °C for 10 minutes to reach the peak temperature, with the total cycle time of 60 minutes. The gold traces achieved the thickness of 8-11 μm.

The next step involved attaching Inconel cables for the power supply, ground, and oscillator output connections. Inconel cables were chosen for their excellent heat and corrosion resistance. The Inconel cables were fixed to their designated spots using a ceramic adhesive paste. The SiC MOSFET was integrated into the circuit by bonding its drain, located on the back side as depicted in Figure 33.b, directly onto the circuit's drain terminal on the gold trace. This connection was achieved through wire bonds, creating a net-like configuration to ensure a secure and proper attachment. The resistors and capacitors were secured through the bond wires and ceramic adhesive paste. The Inconel cables were bonded to the circuit using 4 mil platinum wire while the other circuit elements were bonded using 1 mil gold wire. In order to measure the circuit's temperature during experiments, a type-K thermocouple was also attached to the circuit board. The fabricated Alpha circuit is presented in Figure 34, showing component placement on the fabricated layout, along with the Inconel cables and the type-K thermocouple.

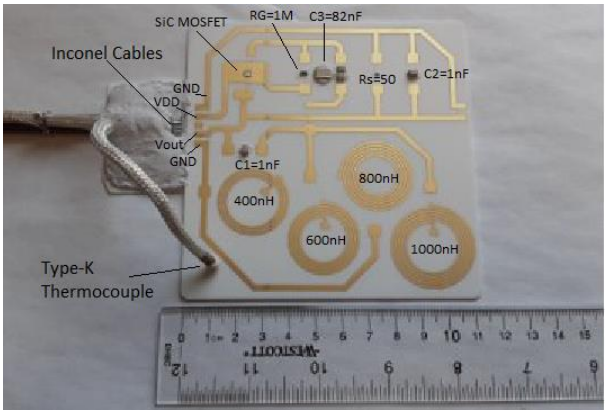

Figure 34: Fabricated oscillator circuit (Alpha) with Inconel cables and thermocouple placement.

3.4. Experimental Setup

Two experimental setups were used, one utilizing a conventional laboratory power supply and the other using thermoelectric generators. Each setup was designed to explore specific aspects of the oscillator circuit's behavior under high temperature conditions.

3.4.1. Setup with Conventional Power supply

Figure 35 illustrates the experiment arrangement, featuring the oscillator circuit within a Thermolyne F6000 box metal furnace. The circuit is powered by a CSI3005xIII power supply from Circuit Specialists. To observe the oscillator's output, it was connected to a RIGOL DS1054 oscilloscope.

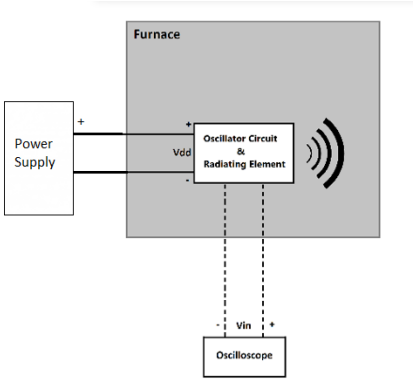

Figure 35: Block diagram of the setup with Conventional Power Supply

The Thermolyne F6000 metallic box furnace is capable of reaching up to 1093°C for continuous operation and up to 1200°C for intermittent use with the stability of ± 3°C at 750 °C. This provides more than sufficient temperature range to meet the experimental needs of this work.

The CSI3005xIII adjustable power supply is capable of sourcing up to 30 V and 5 A. It was used to determine the turn-on voltage of the oscillator, as well as its performance for different supply voltages up to 6V. The power supply provided a stable supply voltage to the circuit, necessary for the long-term stability tests and cycling tests described below.

Placing the oscillator circuit inside a metallic furnace would make wireless transmission impossible. As a result, a non-metallic furnace was designed and built for latter wireless transmission tests.

3.4.2. Setup with Thermoelectric Generators

The block diagram of the setup is shown in Figure 36 . This setup has of four serially connected TEGs heated by a hotplate. The TEGs utilize the temperature difference between their hot side on the hot plate and their cold side connected to heat sinks to generate the electric power. To ensure the voltage stability of the power supplied to the oscillator circuit, the output of the TEG bank is connected to a voltage booster circuit. This DC-DC voltage booster circuit does convert the TEG bank voltage to 6 V, providing a regulated supply voltage to the oscillator circuit.

The oscillator circuit is positioned in the center of the custom-built non-metallic furnace and heated to temperatures up to 450°C. A PID controller is used to control the temperature of the furnace during the experiments. As in Figure, the oscilloscope is connected to the oscillator circuit through Inconel cables to monitor the oscillator circuit's output. The oscillator circuit incorporates an electrically small antenna for wireless signal transmission. The wireless signal is captured outside the furnace environment by a receiving antenna. To analyze the received signal, an Agilent

9320A spectrum analyzer is employed. The detailed description of the setup is explained in the following subsections.

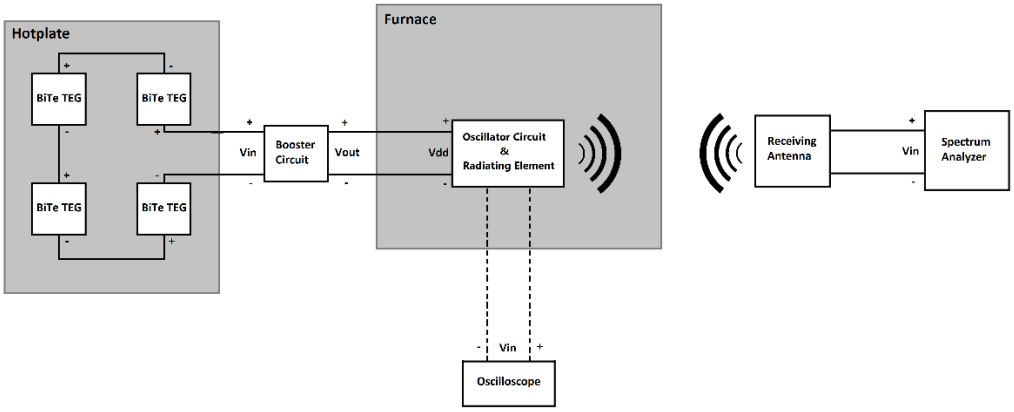

Figure 36:Block diagram of the setup with TEGs and Booster Circuit

The experimental setup utilized four Bismuth-Telluride (Bi2Te3) TEGs procured from Thermoelectric Conversion Systems Ltd. The selection of these specific TEGs was based on their low cost and commercial availability. With a compact size, multiple devices could be easily mounted in a small area. The specifications indicated that each TEG could generate 1V-2V per device at achievable temperature difference (ΔT) in the absence of active cooling, making them suitable for the experiments.

For passive cooling of the TEG's cold side, an aluminum heat sink from Wakefield-Vette was utilized. This heatsink was chosen for its large size, tall fin height, low cost and commercial availability. Its large size provided ample space to accommodate multiple TEGs on a single heatsink. At first, a different heat sink with short fins was used. However, the low height of the cooling fins was inadequate for generating the necessary temperature difference, limiting the voltage output from the thermoelectric generators (TEGs). Switching to a model with taller fins resolved this by improving the temperature gradient and voltage generation, while also enhancing heat dissipation efficiency. Four TEGs were mounted on the backside of heatsink using a thermal

paste (8616-ML from MG Chemicals) and connected in series with insulating strips in between to prevent thermal convection currents which is shown in Figure 37 [38].

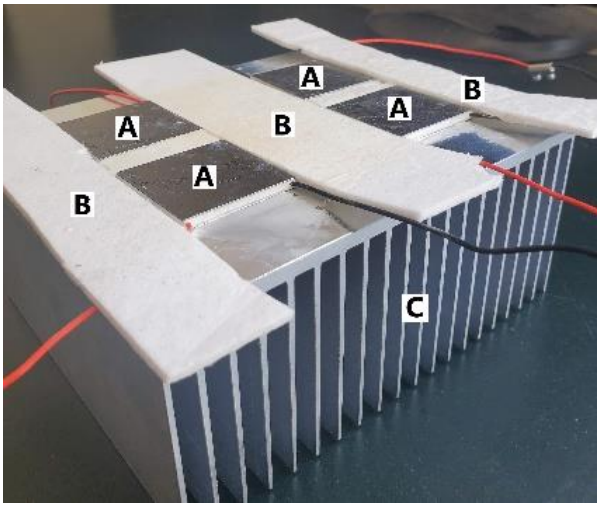

Figure 37: Upside-down view of the four TEGs mounted on the heatsink with thermal paste. The TEGs are marked with (A), (B) is the ceramic insulation and (C) is the heatsink

The X0122 boost converter from TXL Group was chosen to convert the varying TEG output voltage to 6 V. The booster circuit operates as a buffer between the TEGs and the oscillator circuit, effectively stabilizing the supply voltage provided by the TEGs. This stabilization becomes essential during testing as it was observed empirically that directly connecting the oscillator to the TEGs did not result in successful oscillation. The booster circuit mitigates this issue by buffering the TEGs from experiencing the large periodic swings in current drawn by the oscillator circuit, allowing the circuit to oscillate successfully. Without the booster circuit, the TEG's lack of internal feedback circuitry could lead to significant voltage swings that prevent oscillation from occurring.

The custom non-metallic furnace was constructed using a ceramic fiber board insulation (from Cotronics Corp) to mitigate the interference caused by metallic furnace and enable wireless signal transmission from within the high temperature environment. Temperature control was achieved by incorporating a serpentine heating element (from Watlow Electric Manufacturing Co.)

at the bottom of the furnace and the PID controller (CNPT-series from omega engineering). The oscillator circuit was housed inside this furnace, while the TEG and booster circuit setup from was placed in a separate heater on top of the furnace. Temperature for this heater was also controlled using the CNPT-series PID controller. A sideview and top-down view of the combined furnace and TEG setup is presented in Figure 38 [38], detailing the various components and their arrangement.

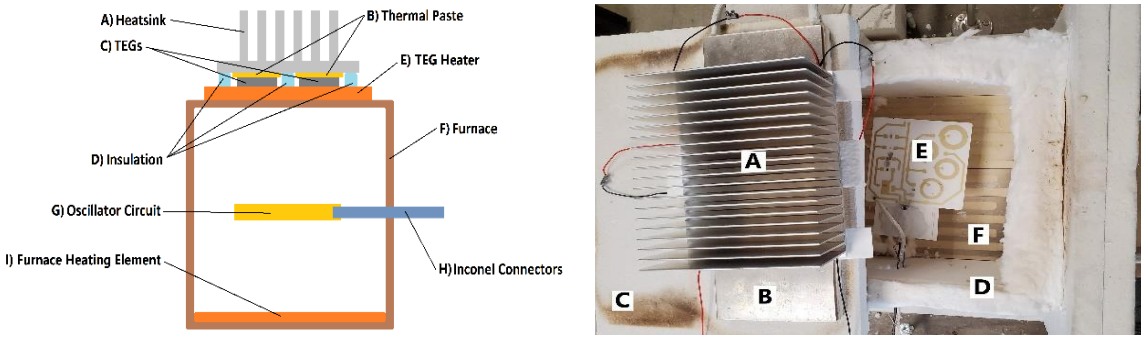

Figure 38: Combined TEG/Furnace/oscillator circuit setup a) Side view b) Top-down view of combined TEG/furnace/oscillator circuit setup, with top cover partially opened and shifted to the left so that the oscillator circuit is visible inside the furnace. A) Heatsink and TEGs. B) Heater for controlling TEG temperature. C) Top cover of furnace. D) Side wall of furnace, constructed from ceramic fiberboard. E) Oscillator circuit, implemented on alumina board

The receiving antenna depicted in Figure 38 is a rectangular loop type which was designed to detect the wireless signal transmitting from the oscillator circuit placed inside a high-temperature environment. A rectangular loop design was chosen as a 6 MHz dipole antenna was impractical due to its large length (25 meters). Therefore, an electrically small rectangular loop antenna was constructed using a copper wire loop, fastened onto a wooden frame to ensure structural integrity and support. Due to the spatial limitations of the laboratory in which the experiment was performed, the receiving antenna was placed at an 11-foot (approximately 3.4 meter) distance from the high temperature furnace. The specific implementation and physical appearance of the receiving antenna is shown in Figure 39 [38].

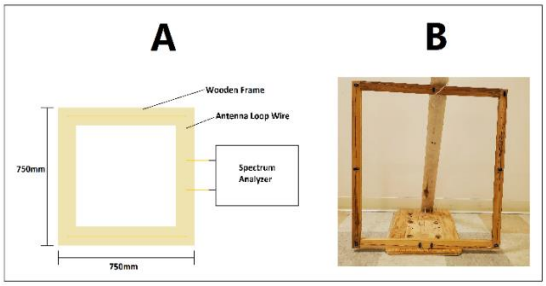

Figure 39: Experimental Loop Antenna Configuration(A) Schematic Representation of the Antenna Connected to the Spectrum Analyzer (B) Actual Physical Setup of the Antenna

3.5. Experimental Procedures

The experimental procedures included a ramp test, stability test, cycling test and a wireless transmission test. Each test provided valuable insights into different aspects of oscillator's performance and its potential applications in harsh environments.

3.5.1. Ramp Test

A ramp test was conducted to gather information on the oscillator's performance under varying temperature conditions. The test covered a temperature range from room temperature to 400 °C with an increment of 50 °C for each step. At each temperature level, the circuit was allowed to stabilize or 'soak' for an hour before the measurements were taken. At each temperature point, twelve distinct transient data points were captured from the oscilloscope's output to account for variation from oscilloscope. By further processing the data, information such as peak-to-peak voltage (VPP), frequency, and power output were determined, enabling a detailed study of the circuit's behavior across the entire temperature range.

3.5.2. Stability Test

To capture the long-term behavior of the oscillator circuit, a 48-hour stability test was executed. MATLAB's Instrument Control Toolbox was used for automatic data acquisition from

the oscilloscope. The MATLAB script was designed to interface with a Rigol oscilloscope, which was connected to the oscillator circuit's output. Over the 48-hour period, the script automated the process of capturing the data from the oscilloscope, ensuring a steady stream of measurements. The temperature was maintained at 300 °C ±5 °C, throughout the test duration. Every thirty minutes, the MATLAB script captured a set of 12 distinct measurements. Using the obtained dataset, a comprehensive analysis of the oscillator circuit's stability and performance during extended high-temperature operation.

3.5.3. Temperature Cycling Test

A thermal cycling test was conducted to evaluate the circuit's resilience and its ability to revert to its initial performance parameters following exposure to a sequence of temperature cycles. In this experiment, the circuit's temperature was raised from ambient room temperature to 300°C and subsequently returned to room temperature. This process was repeated three times. The primary objective of this test was to determine if the circuit's output demonstrated any variation or instability during these temperature cycles.

3.5.4. Wireless Transmission Test

In the wireless transmission test, the oscillator's output signal was captured using an electrically small rectangular loop antenna, shown in Figure 38, which was placed at the distance of 11 ft from the oscillator circuit inside the furnace. The captured signal was then analyzed using a spectrum analyzer (Agilent 9320A) to examine its frequency content and other characteristics. By doing so, the test provided valuable information about the quality and strength of the oscillator's wireless signal output, a crucial aspect for its potential applications in wireless communication in harsh environments.

CHAPTER 4

MEASUREMENTS AND ANALYSIS

4.1. Introduction

In this Chapter, the measurement results obtained from the experiments described in Chapter 3 are presented and analyzed. These measurements were made using the preliminary circuit Prototype #1 and the two reconfigurable layouts 'Alpha' and 'Beta'. Notably, the Alpha and Beta circuits were replicas of each other, and the circuit was reconfigurable due to the inclusion of four different values (400 nH,600nH,800nH, 1000nH) spiral inductors. The circuits' performance, including amplitude, frequency, and power consumption, were investigated in a broad range of temperatures and power supply voltage. Simulation and experimental are compared and possible reasons for the discrepancies are discussed.

4.2. Oscillator Circuit testing with Bench-Top Power Supply

This section provides a detailed overview of the experimental results obtained from testing the oscillator circuits using the CSI3005xIII power supply as described in section 3.4.1. All three circuits were tested with this configuration.

The Prototype #1 circuit was evaluated with tests performed using three different voltages (including the turn-on voltage, 4.5V, and 6 V) and temperature conditions (from room temperature to 350 °C in 50°C steps). The circuit's performance parameters such as signal amplitude, frequency, and power consumption were measured, and wireless transmission capability was assessed.

Following the evaluation of the preliminary circuit, the Prototype #2 Alpha and Beta circuits were tested. Experiments with the Beta circuit included ramp tests, cycling tests, and

repeatability tests. Each of these tests was designed to examine a different aspect of the circuit behavior under different conditions. The Alpha circuit, on the other hand, was mostly tested using TEGs as the power source. Both the Alpha and Beta circuits were subjected to 48-hour bake tests at 300 °C using the power supply. The 48-hour stability test allowed for the study of the oscillator's performance over an extended period, providing insights into its long-term reliability and behavior at 300 °C.

4.2.1. Temperature Ramp Test Results

Temperature ramping tests with the bench-top supply powering the circuits were conducted on the Prototype #1 and Beta circuits. The circuit under test was placed inside the Thermolyne 6000 furnace. The furnace temperature varied from room temperature to 400 °C at 50°C steps. The local temperature of the circuit inside the furnace was measured using a type-K thermocouple attached to a USB-2001-TC temperature sensor.

i) Prototype #1 Circuit testing:

The experiments were performed at three supply voltages: the turn-on voltage, 4.5 Volts, and 6 Volts. The turn-on voltage is defined as the minimum supply voltage required for the oscillation to start. The experiments were initially intended to cover a range of temperatures from room temperature to 400°C in 50 °C steps. However, due to the instability of the oscillation amplitude beyond 350°C, results and analysis in this section are confined to temperatures up to 350°C.

Figure presents the recorded output from the preliminary circuit at room temperature under two input voltages: the turn-on voltage and 6 V. The measurements taken with the oscilloscope in AC coupling setting. The minimum supply voltage required to initiate oscillation at room temperature was 4.62 V. At a supply voltage of 6, the circuit's amplitude increased as indicated by red plot in the Figure 40.

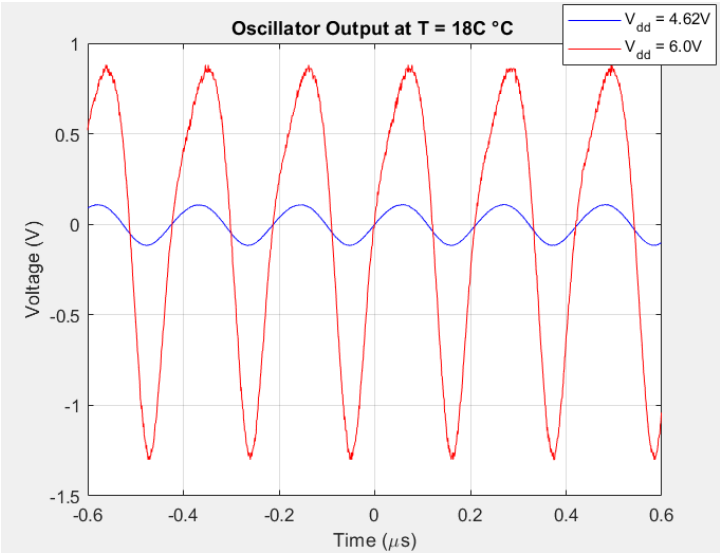

Figure 40: Prototype #1's output voltage at room temperature for different supply voltages represented by the red(6V) and blue (4.62V) plots

Figure 41 shows the output of Prototype #1 at 350 °C at three different voltages: turn on voltage (3.26 V), 4.5 V and 6 V, shown by blue, green and red lines respectively. The turn on voltage for the circuit at 350 °C is 3.26 V, going down from 4.62 V at room temperature.

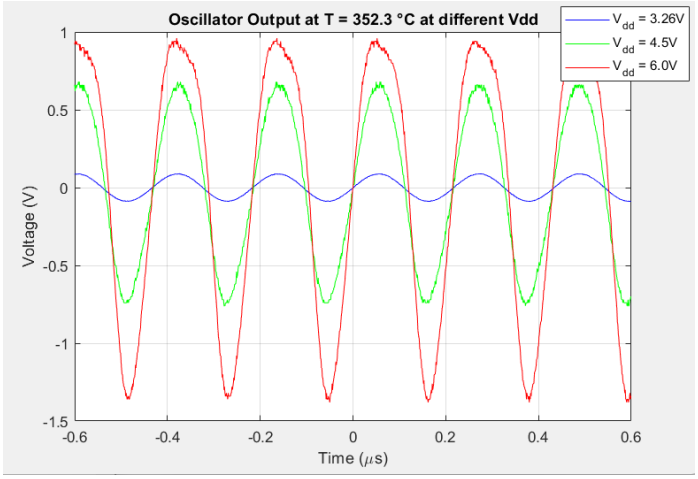

Figure 41: Prototype #1's output voltage at 350 °C for different supply voltages represented by the red(6V), green (4.5V) and blue (3.26)

Figure 42 shows the relationship between the turn-on voltage required for oscillation and temperature. The turn-on voltage decreases as temperature rises. This trend can be attributed to the reduction of MOSFET's threshold voltage with the increase in temperature.

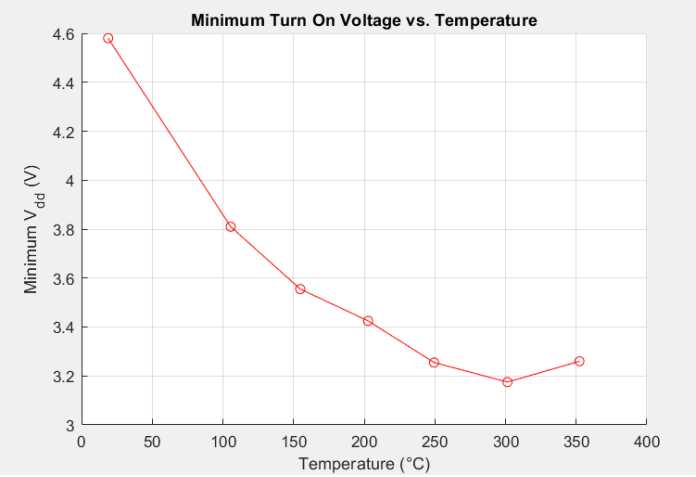

Figure 42: The relationship between minimum turn-on voltage for oscillation and temperature for Prototype #1

The oscillation frequency was computed by employing the zero-crossing method. This entailed identifying the points where the signal crossed zero (transitioning from positive to negative or vice versa). By calculating the time interval between these zero-crossing points, and taking the average over multiple cycles, the oscillation period was determined. The oscillation frequency was determined by taking its reciprocal. An alternative method, taking the FFT of the time-domain measurement, required a wider time base to achieve a high frequency resolution. This in turn results in a poor time resolution. The measurements in these experiments prioritized the waveform shape, and as such zoom in on five cycles at most.

The oscillation frequency relative to temperature is plotted plots in Figure 43 , at turn on, 4.5 V and 6 V shown by blue, black and red, respectively. It can be seen that the frequency drops up to 300°C. Beyond 300°C the trend reverses with frequency following an upward trajectory from 300°C to 350 °C for each voltage.

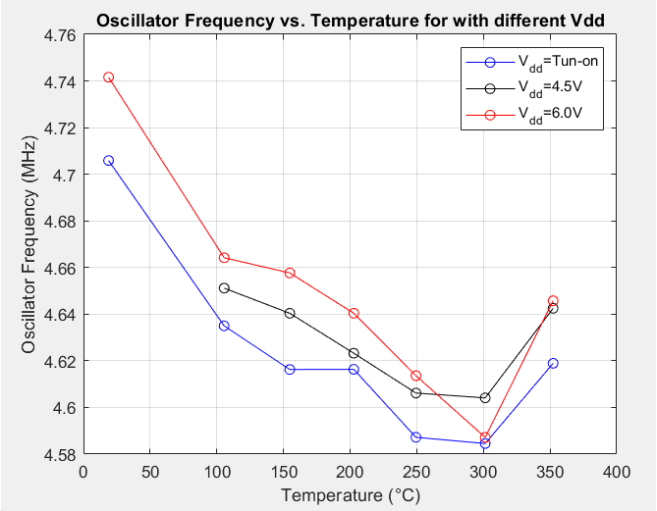

Figure 43: Oscillation frequency vs Temperature at turn-on (blue), 4.5 V (black) and 6 V (red) plots

Like the frequency analysis, the peak-to-peak output voltage (VPP) magnitude was examined against temperature at different supply voltages, shown in Figure 44. The output magnitude for 6 V supply is shown with the red line in the Figure. The output voltage magnitude increased from 2.2V at room temperature to 2.5V at 100°C and gradually decreased with temperature to 2.3V. For 4.5 V supply shown in black, the output voltage increased from 1.25V at 100°C to 1.6 V at 300 °C and decreased to 1.4V at 350°C. At the turn-on voltages, the peak-to-peak voltage (depicted in blue) maintained a consistent value of 0.22V. This remained unchanged as it represented the lowest voltage necessary to initiate oscillation.

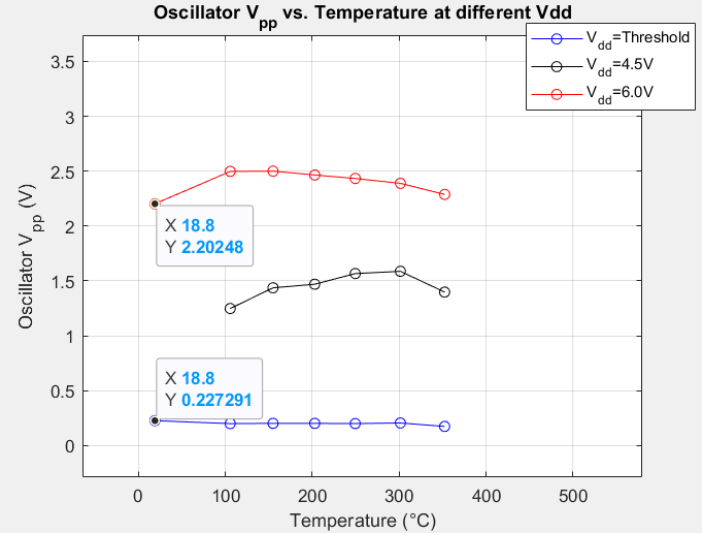

Figure 44: Peak-to-Peak Voltage (V_{PP}) vs Temperature for the preliminary circuit at various supply voltages shown in blue(turn-on), black (4.5) and red (6 V) plots

The current drawn by the oscillator circuit as a function of temperature and supply voltages are shown in Figure 45(a). The current reported by the CSI3005xIII power supply was recorded. The power supply's own ammeter has a resolution of 10mA. The power consumption shown in Figure 45 (b) was computed using these current measurements, by multiplying the current drawn with the supply voltage. For a 6 V supply voltage (shown in red) the power consumed increased from 300 mW at temperature to 420 mW at 200°C, corresponding to the supply current increasing from 50mA to 70 mA. From 200 °C to 350°C, the power consumption appeared to stabilize, corresponding to a relatively flat current draw over this temperature range. At 4.5 V supply voltage (shown in black) the supply current increased from 30 mA at 100 C to 40 mA at 150C, which increased the power consumption from 140mW to 180 mW. From 150C to 350C, power consumption appeared to stabilize around 180 mW, corresponding to the flat current draw over this temperature range.

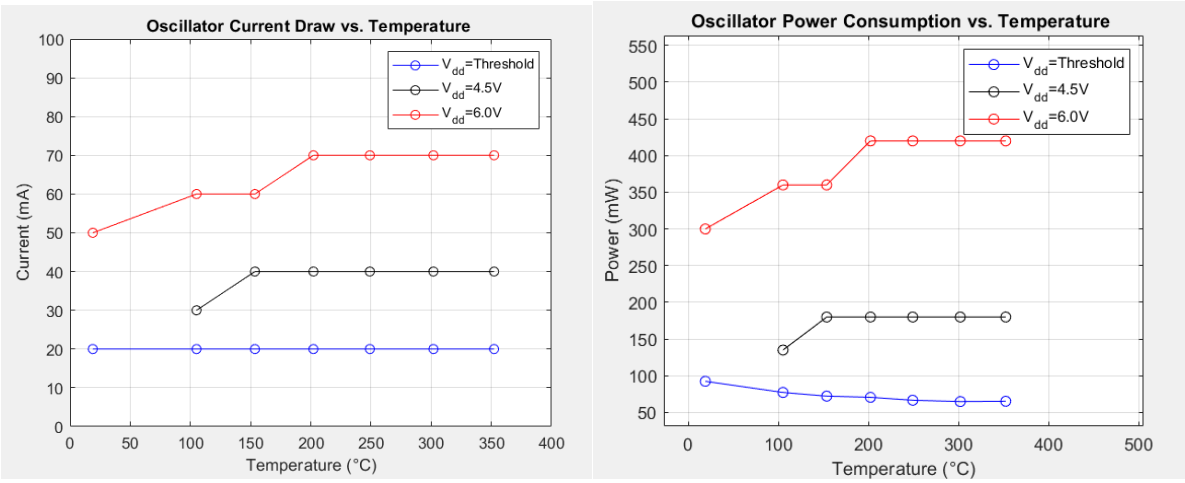

Figure 45(a) Current draw vs temperature(left) (b) Power consumption vs Temperature(right) for the preliminary circuit at various supply voltages shown in blue(turn-on), black (4.5) and red (6 V) plots

A stabilization in current draw at high temperatures is observed for both 6 V and 4.5 V supply voltages. The reason for this can be stated by two opposing effects. Initially as the temperature rises, the decrease in threshold voltage (Vth) dominates, leading to a slight increase in current draw. However, as the temperature continues to increase, the electron mobility goes down as a result of increased phonon-electron interactions that shows down the flow of charge carries. Therefore, these simultaneous effects lead to the observed stabilization in current draw.

ii) Beta circuit testing:

The Beta circuit was subjected to a ramp test similar to the Prototype #1 circuit, with one significant change. Instead of varying the supply voltage, the Beta circuit was tested with a fixed supply voltage of 6 volts. Due to the issues encountered at 400°C during the Prototype #1 testing, the Beta circuit was evaluated from room temperature up to 350°C, with the temperature being incremented in steps of 50°C.

In order to ensure stable temperature readings and accurate results, the circuit was allowed to soak for an hour at each temperature point. Twelve measurements were taken to account for potential variations, and the error bar in the plots below represents the standard deviation (1SD) from the mean value. This approach ensures accurate and reliable presentation of the experimental results. The details of the tests and the corresponding results are discussed below.

The oscillation frequency for the beta circuit was calculated using the zero-crossing method as for Prototype #1. Figure 46 depicts the oscillation frequency as a function of temperature. The trend observed indicates the beta circuit's consistent performance from room temperature to 300°C, with a variation of only 5%. However, beyond 300°C up to 350°C, there is a noticeable upward frequency shift of 20%.

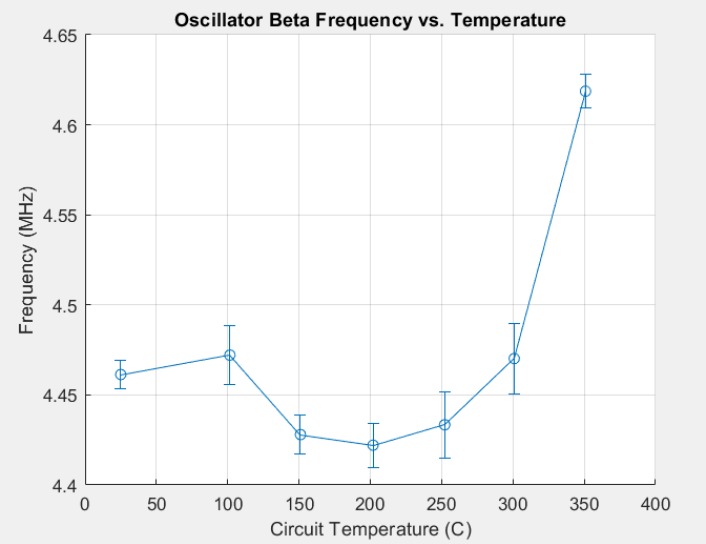

Figure 46: Oscillation frequency vs Temperature for the beta circuit under a fixed supply voltage of 6 V

In comparing the Beta Circuit to Prototype #1, a key difference lies in their response to the temperature changes. While the Beta circuit was tested with a fixed supply voltage of 6 Volts and showed a consistent performance from room temperature to 300 °C, it exhibited a significant upward frequency shift of 20% from 300 °C to 350 °C. In contrast, from Figure 42, the oscillation

frequency of Prototype #1 decreased monotonically over its tested temperature range. This discrepancy could be due to the improved design and differences in measurement approach. In Prototype #1, measurements were taken just once, whereas for the Beta circuit, 10 consecutive measurements were recorded at each temperature point which could lead to more accurate and reliable data, capturing variations and trends that a single measurement might miss.

Figure 47 showcases the peak-to-peak output voltage magnitude VPP for the Beta circuit across the tested temperature range. The output voltage was 2.81 V ± 0.1 V from room temperature to 100°C. The output voltage magnitude increased 3.35 V at 150°C and exhibited only a 2% variation up to 350°C thereafter. The sudden increase in the output voltage magnitude of the Beta circuit between 100°C and 150 °C, may suggest a measurement error as the output can fluctuate with the slight movement of wires from the power supply or specific anomalous behavior in the circuit at this temperature range. This significant change rather than a gradual variation, warrants further examination for more accurate interpretation.

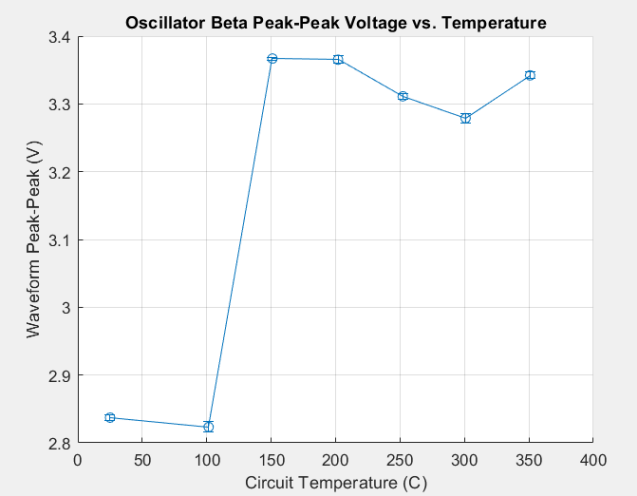

Figure 47: Peak-to-Peak Output Voltage vs Temperature for the Beta circuit

Like the preliminary circuit testing Figure 48(a) and (b) present the current drawn and power consumption respectively against temperature. The trend demonstrates a gradual increase

in power from 300mW to 420mW within the temperature range of 100°C to 300°C. However, between 300°C and 350°C, the average power decreases by 9.5%, corresponding to the decrease in average current.

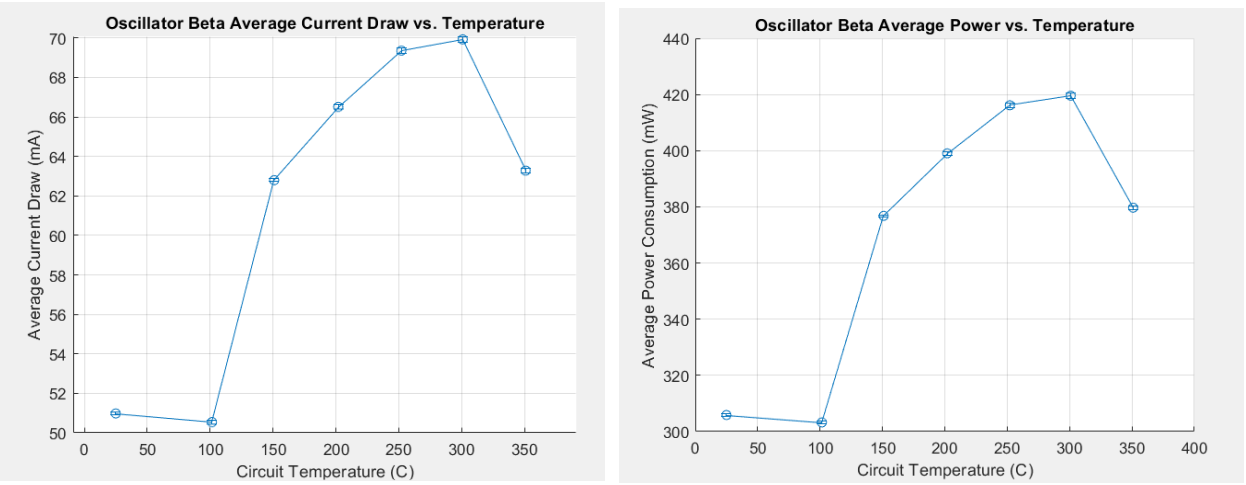

Figure 48(a) Current draw vs temperature(left) (b) Power consumption vs Temperature(right) for the beta circuit under a fixed supply voltage of 6 volts

A cause of the observed decrease in power consumption at 350 °C, despite the constant output voltage, might be increase in the source resistance (Rs) or changes in the component characteristics at this temperature which might lead to reduced current draw, and consequently lower power consumption. This decrease in power could also suggest a change in the circuit's load or internal losses which might require further investigation to validate this hypothesis.

4.2.2. Temperature Cycling Test

The Beta Circuit was additionally put through a temperature cycling test to examine its resilience and performance consistency under repetitive temperature fluctuations. This test aimed to simulate real-world conditions where the circuit may undergo frequent changes of operational temperature.

The circuit was subjected to three cycles of temperature shifts between 100°C and 300°C. Each cycle began by elevating the circuit's temperature to 300°C and maintaining it at this level for an hour. The temperature was then reduced to 100°C and again held steady for an hour. This pattern was repeated three times to emulate repetitive thermal cycling. Measurements were made with the Rigol oscilloscope at each temperature stage, focusing on parameters such as oscillation frequency and peak-to-peak voltages.

Figure 49 (a) and (b) depict the frequency and VPP responses of the Beta circuit during the cycling test respectively. In the initial cycle, a substantial frequency reduction from 4.47 MHz to 4.1 MHz occurred when the temperature dropped from 300°C to 100°C. The oscillation frequency stayed between 4.15 - 4.05 MHz in subsequent cycles. Figure 49 (a) and shows a similar pattern for the output voltage, with a significant drop during the first cycle from 3.3 V to 2.5 V, and less pronounced variations between 2.85 - 2.55 V in later cycles.

These patterns could be due to a hysteresis effect or a permanent change in component values. Hysteresis means that the circuit's past thermal conditions impact its performance in later cycles. To investigate this, a more detailed repeatability test was performed which is explained below.

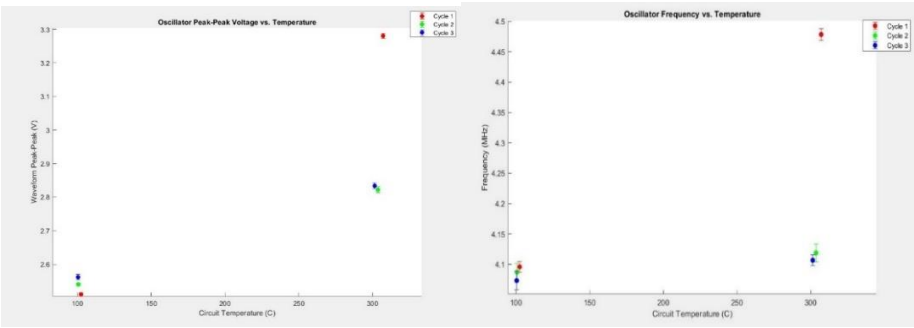

Figure 49(a) Oscillation Frequency versus Temperature (on the left) (b) Peak-to-Peak Voltage (VPP) versus Temperature (on the right) for three cycles (Red - Cycle 1, Green - Cycle 2, Blue - Cycle 3) during the Cycling Test of the Beta Circuit between 300°C and 100°C

4.2.3. Repeatability test

The hysteresis-like effect observed during the cycling test for the Beta circuit was further investigated to determine if it was hysteresis or a permanent shift in the circuit's behavior. The procedure started by initially elevating the Beta circuit's temperature to 50°C, followed by a 30-minute stabilization period. The temperature in the furnace was brought up to 100°C, where the circuit was allowed to stabilize for an hour, ensuring that any changes in its behavior could be accurately attributed to the temperature increase. Next, the temperature of the circuit was increased to 300°C, with measurements taken every 2 minutes. This allowed for a thorough analysis of how the circuit's response fluctuated with rising temperature. After achieving the 300°C mark, the circuit was left undisturbed for an hour to observe any changes or anomalies in its behavior at high temperatures. Finally, the furnace's temperature was returned to 100°C and held at the temperature for 30 minutes, and measurements were recorded every 5 minutes as the circuit cooled.

The findings from the repeatability test are displayed in Figure 50(a) and (b). Figure 50 (a) illustrates the oscillation frequency as a function of temperature, with separate paths for the ramp-up (in green) and ramp-down (in red) cycles. As the circuit heats from 100°C to 300°C, the oscillation frequency remains within 4.4-4.5 MHz until the temperature reaches 300°C. Here, an unexpected increase in the oscillation frequency is observed, peaking at 4.9 MHz. While cooling down to 100°C, the frequency gradually decreases and settles in the range of 4.5-4.6 MHz which is 2.27% higher than the initial frequency measured during the ramp up cycle at 100°C.

Figure 50 (b), on the other hand, offers a different perspective by representing the frequency changes over time at various temperatures, symbolized through a color gradient transitioning from blue (100°C) to red (300°C).

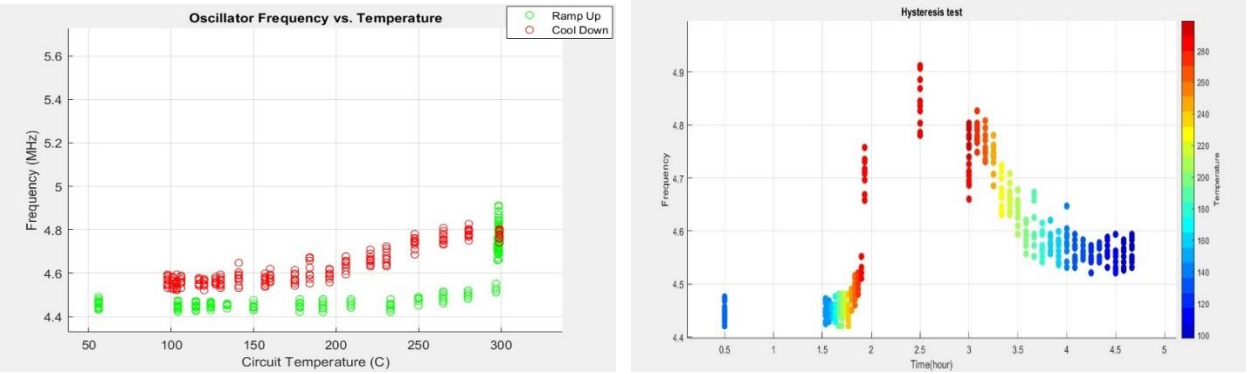

(a) (b)

Figure 50(a) Oscillation Frequency vs. Temperature for the hysteresis test, depicting both ramp-up (green) and ramp-down (red) cycles; (b) Oscillation Frequency vs. Time for the hysteresis test, with a color gradient ranging from blue (100°C) to red (300°C), indicating frequency changes at diverse temperatures over time

Figures Figure 51 (a) and (b) illustrate the peak-to-peak voltage (VPP) behavior against temperature and time respectively during the hysteresis test. During the heating phase, the VPP shows slight fluctuations, but a noticeable decrease from 2.6V to 1.25 V is observed at 300°C during the hour-long stabilization period. As the system cools back to 100°C, the VPP gradually increases but settles at around 1.4 V which is 46% less than its initial value at the same temperature during heating, indicating a change similar to the one observed in frequency measurements.

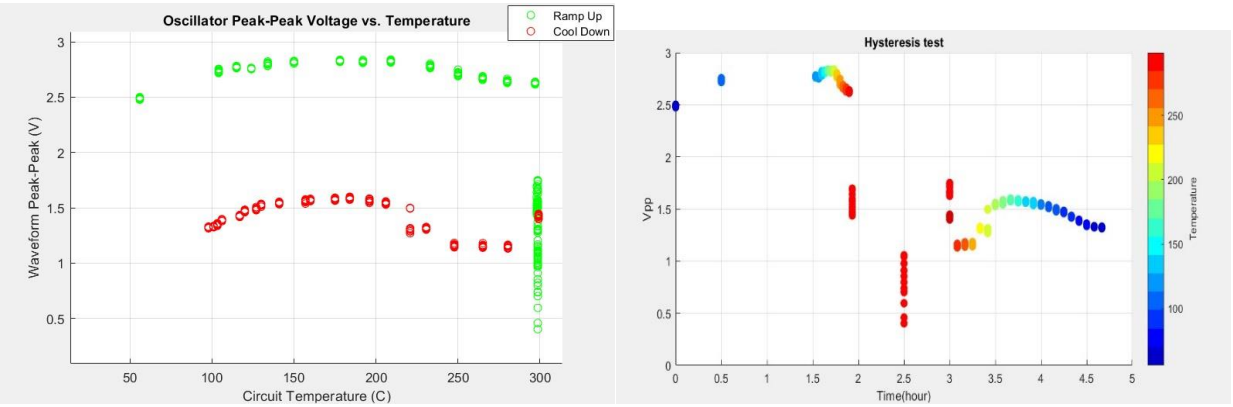

(a) (b)

Figure 51(a) Variation of peak-to-peak voltage (Vpp) against temperature during the hysteresis test. The heating cycle is shown in green and the cooling cycle in red; (b) Variation of peak-to-peak voltage (Vpp) against time for different temperatures during the hysteresis test. The temperature gradient from blue (100°C) to red (300°C) is displayed alongside.

The repeatability test on the Beta circuit aimed to discern if the observed behavior was true hysteresis or a permanent change. results, as depicted in Figure 50 and Figure 51, showed significant changes in both frequency and Vpp across temperature cycles. Notably, the circuit's parameters did not revert to their initial values after cooling, suggesting a permanent shift rather than reversible hysteresis. This implies that the circuit at high temperatures experiences permanent changes, as repeated tests cause the circuit parameters to shift irreversibly, suggesting the change in MOSFET characteristics or component degradation during high-temperature exposure. It is also important to note that the resistor was rated only up to 250°C. Repeated exposure of temperatures above 250°C might have degraded the resistor's performance, which might also be another reason for the permanent shift in the frequency and $V_{PP.}$

4.2.4. Bake Test

To evaluate the long-term stability of Alpha and Beta circuits under sustained operation, bake tests were performed at a constant furnace temperature of 300°C. Automated data acquisition was carried out using MATLAB, with 12 consecutive measurements taken 15 minutes apart for the Alpha circuit and 30 minutes for the Beta circuit. The Alpha circuit underwent a 48-hour bake test while the Beta circuit was tested for a period of 60-hours. However, a notable point was the Beta circuit's exposure to a higher temperature of 350°C during the ramp test while the Alpha circuit was taken only to 300°C, which might have led to the additional variations in its results compared to the Alpha circuit as discussed below.

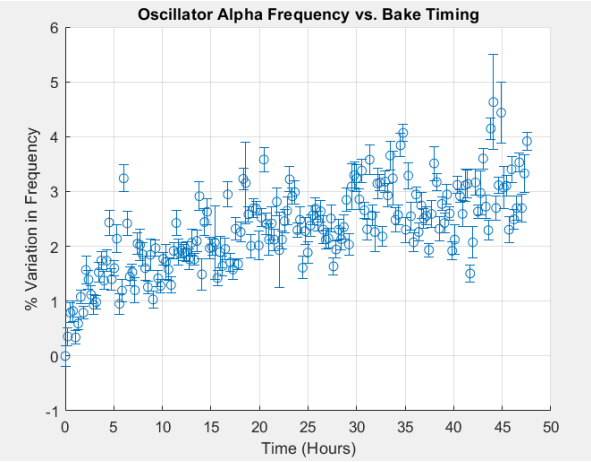

(a)

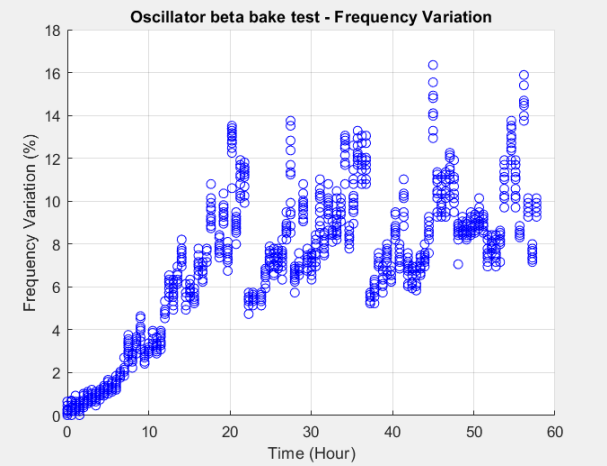

(b)

Figure 52(a) Percentage frequency variation for the Alpha circuit over a 48-hour bake test; (b) Percentage frequency variation for the Beta circuit during a 60-hour bake test

Figure 52 (a) and (b) illustrate the percentage frequency variation of Alpha and Beta circuits throughout their respective bake test durations. It can be seen that the frequency drift is increasing with bake time indicating the change in the component's values or MOSFET performance itself. The Alpha circuit demonstrated robust performance with minimal variation, staying below a 5% change in frequency, as depicted in Figure 52 (a). Conversely, the Beta circuit's performance displayed a higher variation of up to 16% throughout the test, as shown in Figure 52 (b).

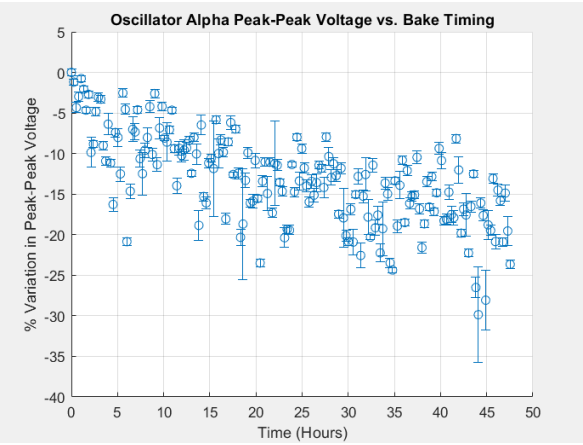

(a)

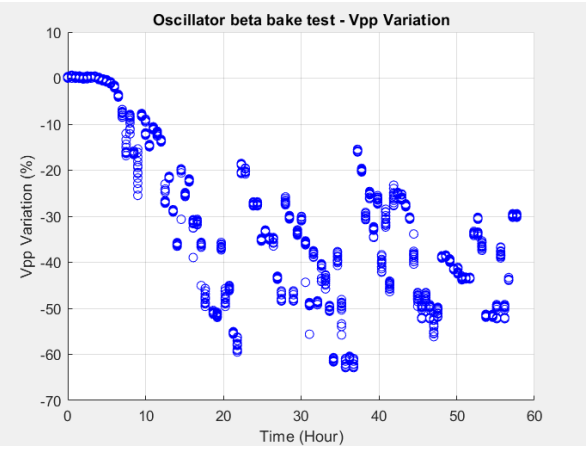

(b)

Figure 53(a) Peak-to-peak voltage (VPP) variation for the Alpha circuit over a 48-hour bake test; (b) Peak-to-peak voltage (VPP) variation for the Beta circuit during a 60-hour bake test

In addition, Figure 53 (a) and (b) portray the variation in peak-to-peak voltage (VPP) for Alpha and Beta circuits over their individual bake test durations. For the Alpha circuit, as shown in Figure 53 (a), the peak-to-peak voltage (VPP) variation was up to 35 %. Meanwhile, the Beta circuit, as depicted in Figure 53 (b), had the larger VPP fluctuation up to 60 %.

The results of the bake tests, as detailed in the study, confirm that both the Alpha and Beta circuits exhibit instability in terms of frequency and peak-to-peak voltage over extended periods of use. This is due to the aging of the components. The wire bonding to aluminum bond pads on the MOSFETs were observed to deteriorate. Additionally, the source resistance as well as the bias gate resistance increased in value with the temperature. This emphasizes the importance of optimizing circuit design for stability, particularly when the intended use involves prolonged operation periods.

4.3. Oscillator Circuit testing with TEGs

This section focuses on the results obtained from testing the oscillator circuits using Thermoelectric Generators (TEGs) integrated with a booster circuit following the experimental procedures as explained in section 3.4.2. Such an approach would be necessary in situations where conventional power supply wires were not practical or possible. The Prototype #1 and Prototype #2 Alpha circuits were placed in the custom-built furnace and tested while powered by the TEGs and voltage booster.

The TEGs and the booster circuit were characterized under loaded and unloaded conditions to understand their performance at different temperatures. The oscillator circuits were subjected to ramp tests, stability tests and wireless reception tests. The following subsections will delve into the specific details of the tests and results obtained.

4.3.1. TEG Voltage vs Temperature Characteristics

TEGs were arranged in series and affixed to the Wakefield-Vette heatsink and placed on the heated plate as shown in Figure 38 and. Figure 54 (top) shows the plots of the TEG open-circuit voltage output (represented by the blue dashed curve with no load) which was measured using a multimeter (model 287, Fluke, Everett, WA, USA). The hot side temperature measurements were taken with varying heater surface temperatures, ranging from 100°C to 170°C. The cold side temperature was not directly measured during this experiment. The data collected from the experiment demonstrates the TEG voltage's relationship with the hot-side temperature, which is approximately linear. At a heater temperature setting of 170°C, the TEGs collectively provided an open circuit voltage of approximately 6.4-6.5V.

To assess the loading effects, the TEGs were connected to the booster circuit, and the booster circuit was subsequently linked to the oscillator circuit. Throughout this test, the oscillator circuit operated at room temperature. The red dashed curve in Figure 54 [38] (top) illustrates the loaded TEG output voltage plotted against the hotplate temperature. The data begins at a hotplate temperature of 120°C, as below this value, the TEGs did not supply sufficient voltage/power to drive the booster/oscillator system effectively.

In Figure 54 (bottom), the current supplied to the booster circuit by the TEGs is depicted as a function of the hotplate temperature setting. The current value was calculated using the voltage difference between open-circuit and loaded-circuit conditions and the output resistance of the TEG system. It is to be noted that it was calculated assuming that the TEG has a fixed output resistance. Notably, the output of the booster circuit remained at an average voltage of 6V. The current draw of the booster circuit exhibits a decrease as the hotplate temperature increases from 120°C to 160°C. This can be attributed to the rise in supplied TEG voltage with increasing temperature,

combined with the relatively constant power consumption of the booster/oscillator system maintained at room temperature during the test. However, between 160°C and 170°C, the current draw increases. This is due to the TEG's voltage surpassing the input protection Zener diode's turn-on voltage in the booster circuit, leading to the activation and conduction of current through the Zener diode.

The results derived from Figure 54 demonstrate the capability of the passively cooled TEG/heatsink system to power the room temperature booster/oscillator system effectively when the TEGs are heated to at least 120°C on the hot side. It is noteworthy that a temperature of 120°C is sufficient to power the oscillator at room temperature. However, the data reveals that the TEGs can safely operate up to 170°C if the oscillator's power draw increases at elevated temperatures.

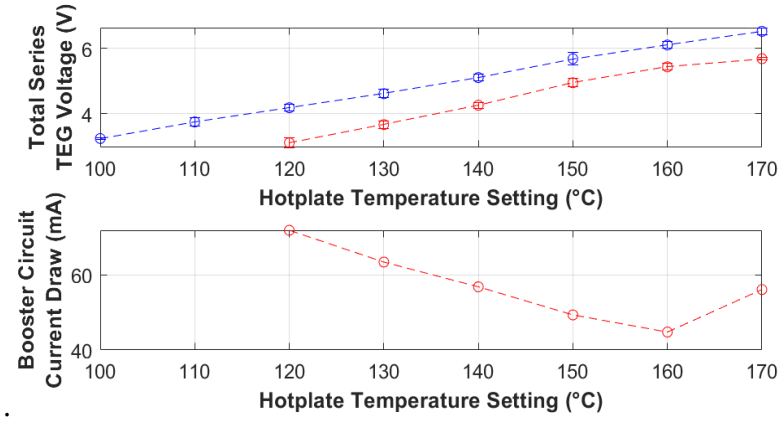

Figure 54: Voltage and current characteristics of four series-connected BiTe TEGs on Wakefield-Vette Heatsink. The top plot displays total open circuit TEG voltage (blue curve) and total loaded circuit voltage when connected to the booster/oscillator (red curve). Bottom plot shows current drawn by the booster circuit from the TEGs *[38]*.

4.3.2. Performance of Booster Circuit

The booster circuit (X0122 DC/DC converter) plays a vital role in ensuring a stable supply voltage for the oscillator circuit powered by TEGs. Acting as a buffer between the TEGs and the

oscillator circuit, the booster circuit stabilizes the supply voltage from the TEGs. Directly connecting the oscillator to the TEGs was found to be unsuccessful in achieving oscillation. However, the booster circuit resolves this issue by buffering the TEGs from the large periodic swings in current drawn by the oscillator circuit, enabling successful oscillation.

Figure 55 demonstrates the booster circuit's performance when connected to TEGs operating at 170°C and the oscillator circuit operating at room temperature. The blue curve represents the voltage swing of the oscillator, the yellow curve displays the TEG output voltage with approximately 0.5 VPP ripple, and the red curve depicts the booster circuit output with approximately 1 VPP ripple. Notably, the ripple frequency in both cases matches the oscillator waveform frequency.

The observed voltage ripples are a result of the periodic current demands from the oscillator waveform. Ideally, the booster circuit should maintain a 50mV-100mV ripple with a frequency defined by its internal oscillator (200 kHz) during nominal operation. However, during this test, the booster circuit could not maintain the specified nominal ripple value due to the oscillator circuit's current draw.

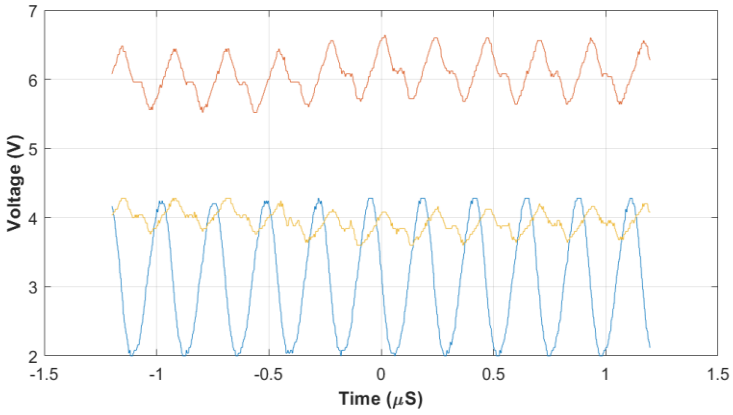

Figure 55: TEGs at 170°C, oscillator at room temperature. Blue curve: oscillator voltage output. Yellow curve: TEG voltage output. Red curve: booster circuit voltage output [38].

4.3.3. Ramp Test Results

The Alpha circuit was tested from room temperature up to approximately 300°C, with the TEG heater held at a constant 170°C. Oscilloscope measurements were taken at eight temperature points between room temperature and 300°C. At each temperature, twelve measurements were performed, and data were collected and averaged for the oscillating frequency, peak-to-peak output oscillator voltage, current and power drawn by the oscillator circuit.

Figure 56 depicts the oscillation frequency as a function of temperature. The oscillator circuit exhibits a maximum 1.3% rise in frequency as the temperature increases. While the variation is expected for our simple and primitive design, it might be unacceptable for most standard applications.

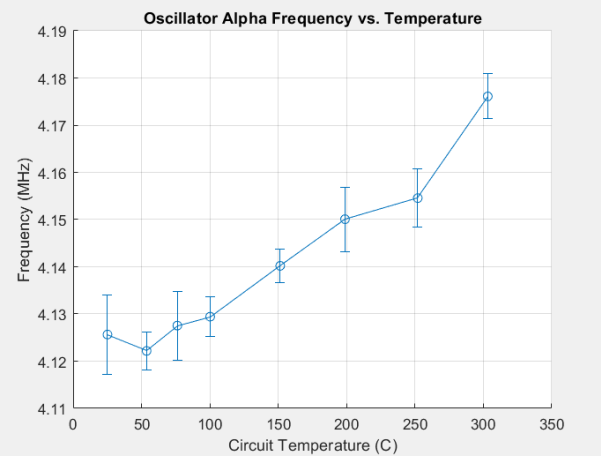

Figure 56: Oscillation frequency vs Temperature for the alpha circuit powered by TEGs and booster circuit

Figure 57 depicts the changes in the output magnitude versus temperature from room temperature to 300°C. The trend suggests a rise in magnitude up to 200°C, beyond which it stabilizes up to 300°C.

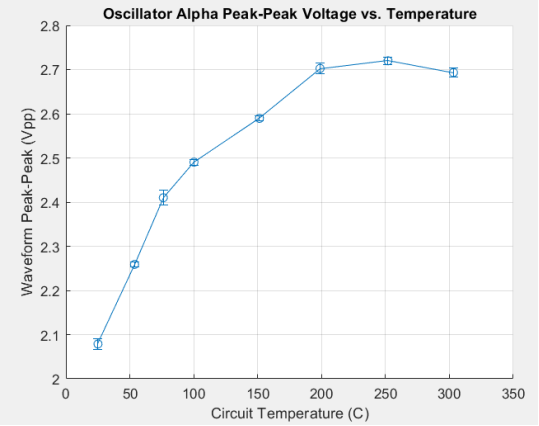

Figure 57: Peak-to-Peak Voltage (VPP) vs Temperature for the alpha circuit for the alpha circuit powered by TEGs and booster circuit.

Figure 58(a) and (b) present the current drawn and power consumption versus temperature, respectively. The current draw increases up to 250 °C and settles at 74 mA between 250 °C and 300°C. The power consumption plot follows the same trend where power consumption rises gradually with temperature until it reaches the same stable point between 250°C and 300 °C.

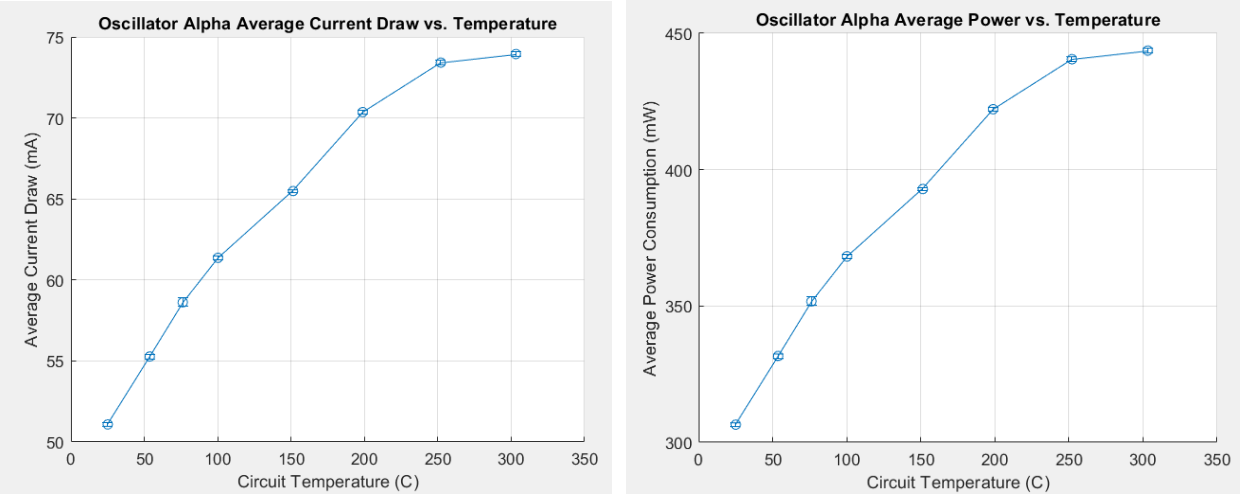

(a) (b)

Figure 58. (a) Current draw vs temperature(left) (b) Power consumption vs Temperature(right) for the alpha circuit powered by TEGs and booster circuit

4.3.4. Bake test with TEGs

A four-hour bake test was performed with the Alpha circuit while it was powered by TEGs and booster circuit, with the TEG hotplate temperature maintained at 170°C. The furnace

temperature was maintained at 300°C for 4 hours and the data was collected every 15 minutes throughout the duration of the experiment using a MATLAB script like done in section 4.2.3. except that the bake test with TEGs for the alpha circuit was performed prior to the 60 hours test using power supply.

Figure 59(a) and (b) shows the percent variation of the frequency and peak to peak voltage for the duration of 4 hours. From Figure 58(a), the frequency variation of 2% can be seen throughout the measurement and the trend shows the upward shift of frequency, while Figure 58(b) shows the variation of up to 8% in the peak-to-peak voltage (VPP) with the downward trend with time. It should be noted that the alpha circuit exhibited lower frequency drift during the initial TEG tests compared to later tests. This observation suggests that the initial tests likely benefited from less degradation in circuit components and MOSFET performance, as prolonged exposure during subsequent testing phases may have led to increased component wear and changes in parameters, impacting stability.

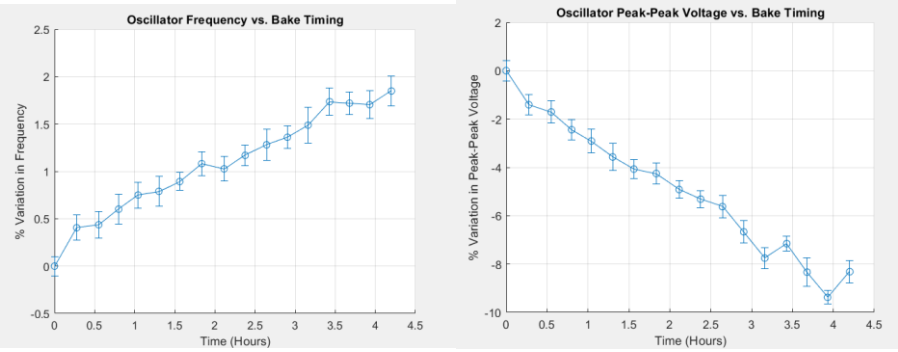

(a) (b)

Figure 59(a) illustrates the percentage frequency variation 58 (b) illustrates the peak-to-peak voltage (VPP) variation of Alpha circuit powered by TEGs and booster circuit during the bake test for 4 hours

4.3.5. Wireless Transmission test

Figure 60 demonstrates the power distribution received at the spectrum analyzer configured for wireless reception with the antenna configuration as shown in Figure 39. The Alpha

oscillator circuit was kept at 300°C. The TEG hot plate was maintained at 170°C, as in the previous experiments. The receiving antenna was positioned at a distance of 11 feet (approximately 3.4m) from the oscillator circuit. The oscillator signal is detected at a frequency of 4.184 MHz, with a power level of -47dBm.

This observation verifies the successful conveyance and acquisition of a wireless signal originating from a high temperature setting to an exterior receiver. Hence, it is established that the TEGs-powered, self-sustaining oscillating system can wirelessly transmit its signal.

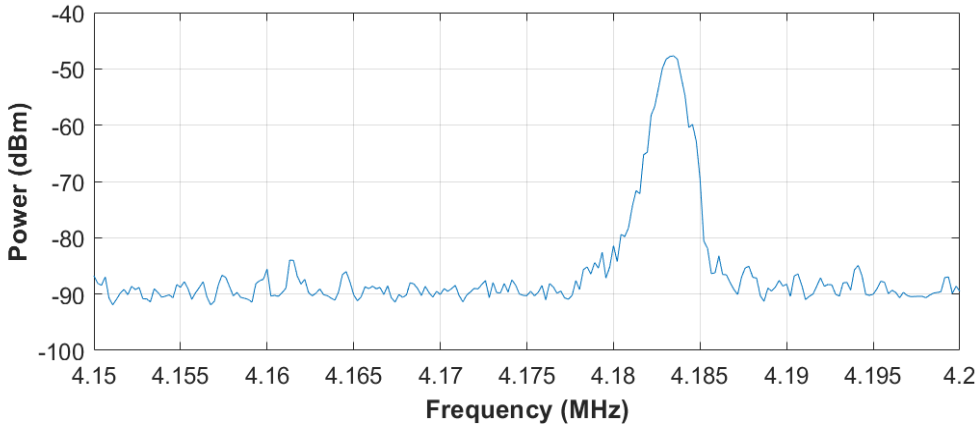

Figure 60: Frequency spectrum of the signal received at a distance of 11 feet from the Alpha circuit

4.4. Comparative Analysis of Simulations and Experimental Results

This section presents a detailed comparison between the data from MATLAB simulations, Montecarlo simulations in Micro-Cap, and the experimental data from various tests conducted on the oscillator circuit. It aims to validate the accuracy of the simulations and identify any discrepancies between theoretical predictions and real-world experimental performance. The focus is primarily on oscillator frequency and Vpp across room temperature and elevated temperatures. Discrepancies will be analyzed to understand their causes, such as limitations in the simulation model or experimental setup.

In analyzing the open loop model of our oscillator, discrepancies between the simulation results obtained from Microcap and MATLAB were observed, though they were relatively minor. The Microcap simulation showed an oscillation frequency of 8 MHz with a gain margin of 6.5 dB. In comparison, the MATLAB model yielded a slightly lower frequency of 7.8 MHz and a gain margin of 7.4 dB. The percentage difference in frequency between the two simulations is approximately 2.56%. The small variance in the results can be attributed to differences in how the models handle the MOSFET's gate-to-drain capacitance (C_{gd}). In the MATLAB model, C_{gd} was not included in the small signal analysis, which could potentially affect the accuracy of the frequency prediction. Omitting C_{gd} in the MATLAB model means that the feedback capacitance effect is slightly underestimated, leading to a variation in the predicted frequency and gain margin.

Table 1: Comparison of room temperature results

Oscillator circuit	Frequency (Micro-cap Simulated) (MHz)	Frequency (Measured) (MHz)	Peak-Peak Voltage (Simulated)	Peak-Peak Voltage (Measured)
Prototype #1	6	4.8	2.5	2.2
ALPHA	6	4.1	2.5	2.1
Beta	6	4.5	2.5	2.8
Beta with (1u) bypass capacitor	6.1	5.5	2.5	2.1

Table 1 summarizes room temperature results for the prototype #1, Alpha and Beta circuits comparing frequencies and peak-to-peak voltages between Micro-cap simulated and measured values. Across the board, simulated frequency was 6MHz, however measured frequencies were

lower, ranging from 4.1 MHz to 5.5 MHz, with the beta circuit incorporating a 1uF bypass capacitor showing the highest measured frequency of 5.5 MHz. The simulated peak-to-peak voltage was 2.5V at room temperature, but measured values varied from 2.1 to 2.8 Volts.

The introduction of a 1µF bypass capacitor between the power supply and ground in the Beta circuit effectively countered the parasitic inductance introduced by the Inconel cable, leading to a frequency shift from 4.5 MHz to 5.5 MHz. This adjustment demonstrates the impact of parasitics on circuit performance and the efficacy of bypass capacitors in mitigating such effects.

Table 2: Frequency Comparison

Temperature	MATLAB Simulation (MHz)	Monte Carlo Micro-Cap mean (MHz)	Experimental Prototype#1 (MHz)	Experimental Alpha (MHz)	Experimental Beta (MHz)
25°C	7.7	6.08	4.74	4.12	4.46
100°C	N/A	6.24	4.66	4.13	4.47
200°C	N/A	6.4	4.64	4.15	4.43
300°C	N/A	6.9	4.6	4.17	4.47
350 °C	N/A	N/A	4.64	N/A	4.6

Table 2 shows the frequency measurements obtained from MATLAB simulations, Monte Carlo simulations using Micro-Cap, and experimental results. The MATLAB simulation provided an overall expected frequency without accounting for temperature variations directly. The Monte Carlo Micro-Cap simulations offered a range of frequencies to account for component tolerances and temperature effects, which were compared against the measured experimental frequencies. The experimental frequencies of Prototype #1, Alpha, and Beta circuits exhibit a percentage change from their respective room temperature values (25°C) to 350°C as follows:

- Prototype #1 shows a decrease of approximately 2.95% from its initial frequency, indicating a slight reduction in oscillation frequency as the temperature increased to 350°C.
- The Alpha circuit demonstrates an increase of approximately 1.21%, showing a rise in frequency over the temperature range, indicative of its stability or minor sensitivity to temperature variations.
- The Beta circuit reveals a minimal change, with an increase of about 0.22%, showcasing a stable frequency response across the evaluated temperature spectrum.

It is critical to note that the Alpha circuit was powered using Thermoelectric Generators (TEGs) and a booster circuit, whereas the Beta circuit and Prototype ramp test were conducted using a direct power supply connection. The use of a booster circuit in the Alpha setup significantly reduced the parasitic inductance effects typically associated with the longer Inconel cable connections used in the tests powered by the power supply. This could explain why the Beta and Prototype circuits exhibited a similar trend of decreasing frequency with increasing temperature, whereas the Alpha circuit demonstrated an increasing frequency trend with temperature.

4.5. Analysis and Discussion

The discrepancies between MATLAB simulations, Micro-Cap simulations, and experimental results can be attributed to various factors:

1. Incomplete MATLAB Model: The MATLAB simulations lacked temperature dependency considerations, making the model incomplete. Due to this only room temperature data could be modeled. Also, MATLAB model did not include all the parasitics such as Cgd in the small signal model which might be one of the reasons for discrepancy in MATLAB and microcap model.

2. Microcap model limitations: In microcap, the temperature coefficients for the passive components such as resistors, capacitors and inductor were not included. Therefore, Montecarlo simulations in microcap should be interpreted with caution.
3. Grounding Issues: The single-layer circuit layout used a ground trace along the periphery of the alumina board, instead of a ground plane as would be used in a multi-layered printed circuit board. This could cause signal bouncing, introducing noise and instability in the oscillator's output, which would not be present in the idealized simulation environments.
4. Component Tolerances: The variability observed between simulations and experimental outcomes is partly due to component tolerances. Both Micro-Cap simulations and real-world experiments involve physical components with manufacturing tolerances, causing variations in electrical properties. These tolerances can lead to shifts in the oscillator's frequency and output voltage. MATLAB simulations typically use ideal components without these tolerances, further widening the gap between simulated and experimental data.

CHAPTER 5

CONCLUSION AND FUTURE WORKS

5.1. Summary

The research presented in this thesis focused on designing, simulating, and validating a Colpitts oscillator circuit capable of continuous operation over a wide temperature range, up to 350℃.

MATLAB and Microcap were used in circuit design and analysis used for both time and frequency domain analysis. These tools facilitated the selection of component values for the Colpitts oscillator circuit. MOSFETs made of the wide bandgap semiconductor SiC were used, due to the temperature limitations of traditional silicon devices. As the commercially available SiC transistors were power MOSFETs, they had large internal capacitances which limited the oscillator's frequency range. Microcap simulations, alongside the sensitivity analysis conducted using MATLAB, highlighted how the oscillation frequency is sensitive to variations in component values. The analysis revealed that changes in the inductor's value had the most impact on the oscillation frequency of the circuit. Monte-Carlo analysis showed the change in output characteristics and number of successful oscillations decreased at the high temperatures. This suggests that as the temperature increases, the circuit's performance becomes less predictable and reliable due to thermal sensitivity of its components.

Three circuits, labeled Prototype #1, Alpha and Beta, were fabricated using materials and components rated for high temperatures. SiC MOSFETs with Al bond pads were obtained from Wolfspeed. High temperature capacitors were procured while the inductors were directly fabricated onto the circuit board itself using printed gold traces in an alumina circuit board. High

temperature resistors were not available at the time of the experiments. Therefore, standard surface mount resistors rated up to 250°C were used.

Experiments were carried out using either external power supplies or thermoelectric generators with a booster circuit. The booster circuit was needed to provide a buffer for the oscillator circuit, as the TEGs alone were unable to supply the necessary voltage and current stability required for reliable oscillation. The TEGs with the booster circuit demonstrated the capability to power the oscillator by heat scavenging which can enable new industrial applications in high temperature environments.

The circuits demonstrated successful operation across a wide temperature range, from room temperature up to 350°C. However, at 400°C, the performance became unstable, leading to no oscillations. Notably, at 300°C, the oscillator's output signal was successfully received from 3.4 meters using a loop antenna situated externally to the furnace, illustrating the oscillator's applicability to remote wireless sensing in high-temperature industrial settings. This achievement lays groundwork for the deployment of wireless sensing technologies aimed at real-time monitoring in environments exposed to extreme temperatures.

The repeatability test revealed that the circuit experienced a permanent alteration in output characteristics, including frequency, peak-to-peak voltages, and output power. This change is likely due to damage to the SiC MOSFET and other components caused by exposure to high temperatures. The packaging of the resistors burned off and the resistor material oxidized, leading to an increase in the resistors' values.

Moreover, the instability in the oscillator's performance during the bake tests further illustrates the circuit's lack of stability in both frequency and amplitude. Specifically, at 300°C, the

Alpha circuit exhibited a drift in frequency of about 5%, whereas the Beta circuit displayed a more significant frequency variation of up to 16%.

Discrepancies between designed, simulated, and experimental results were observed. These can be attributed to the limitations of simulation models to capture complexities of real-world conditions such as parasitic inductances, bond wires integrity component tolerances, grounding issues as well as other factors.

In conclusion, addressing a critical demand for reliable electronics that can operate under extreme temperatures, this research offers a solution for wireless sensing in industries such as oil and gas exploration and extraction, geothermal power generation, automotive and aerospace industries.

5.2. Future Works

This research opens several avenues for future work, aiming to address the observed discrepancies between the designed, simulated, and experimental outcomes, which point to the inherent limitations of current simulation models in fully encapsulating the operation at different temperatures. These gaps emphasize on the need for enhanced simulation models that more accurately reflect the impact of real-world conditions, such as the parasitic effects introduced by inductance in Inconel cables, the integrity of bond wires, component tolerances, and grounding challenges. Also, the simulations did not include the temperature coefficient for the parameters and MOSFET's parasitics in the MATLAB open loop model. A well detailed model as explained can be a part of future work for making the simulations as accurate as possible to the experimental data.

Additionally, the occurrence of permanent changes in the circuit's output characteristics during repeatability tests, particularly at elevated temperatures, warrants further investigation into the resilience of components like SiC MOSFETs and the overall circuit design to prolonged exposure to high heat.

Furthermore, the frequency instability observed during high temperature bake tests suggests the need for more research on improving the stability of oscillator circuits. Future efforts should concentrate on devising circuit designs that are specifically engineered to maintain oscillator signal stability. Investigating temperature-compensated designs and exploring various oscillator topologies, beyond the simplicity of the current models, could offer promising strategies for achieving improved performance and reliability in extreme environmental conditions.

Expanding on this foundation, future research could investigate the incorporation of sophisticated energy harvesting methods, aiming to develop autonomous systems powered by the ambient thermal energy prevalent in high-temperature settings. In addition, further high temperature circuit development is highly desirable, so that circuits such as the booster circuit can be embedded into the HT environment in support of the energy scavenging function. Furthermore, the potential applications of these high-temperature oscillators could be expanded to include a variety of industrial purposes, such as implementing wireless pressure and temperature sensing technologies.

This thesis not only addresses the immediate needs for reliable high-temperature electronics but also sets a foundation for future advancements in the field. The path forward involves continuous innovation and exploration, aiming to develop sophisticated electronic systems capable of withstanding the lost challenging environmental conditions.

BIBLIOGRAPHY

[1] T. K. P. G. N. Gary W Hunter, High Temperature Electronics for Venus Surface Applications, NASA , 2020.

[2] A. C. Andrew A. Wright, "Evaluation of High Temperature Microcontrollers and Memory Chips for Geothermal Applications," in *GRC Transactions, Vol. 46, 2022*, Sandia National Laboratories, Albuquerque, New Mexico, USA, 2022.

[3] A. Veneruso, "High temperature electronics for geothermal energy," *IEEE Circuits & Systems Magazine,* vol. 1, pp. 11-17, 1979.

[4] B. L. G. (. Z. Chinthaka P. Gooneratne, "Sensors_and_Instrumentation_for_Downhole_Environments_-_Challenges_and_Opportunities," in *IEEE Xplore*, Saudi arabia, 2019.

[5] R. V. Ayesha Arjumand Nayeem, "Monitoring of down-hole parameters for early kick detection," *Journal of Loss Prevention in the Process Industries,* vol. 40, no. ISSN 0950-4230,, pp. 43-54, 2015.

[6] Chuan Wu, S. Yang, G. Wen and C. Fan, "A self-powered vibration sensor for downhole drilling tools based on hybrid electromagnetic–triboelectric nanogenerator," *American Journal of Physics* , vol. 92, no. 055003, 2021.

[7] M. B. Gheorghe Brezeanu, "High Temperature Sensors Based on Silicon Carbide (SiC) Devices," *IEEE Xplore,* 2015.

[8] R. R. D. a. R. R. Kubde, "Wide Band Gap Semiconductor Integration for the Defence and Aeronautical Applications," in *EEE International Conference for Innovation in Technology (INOCON),* Bangluru, India, 2020.

[9] A. B. L. K. J. O. T. M. S. M. L. a. A. M. J. Hornberger, "Silicon-carbide (SiC) semiconductor power electronics for extreme high-temperature environments,," in *EEE Aerospace Conference Proceedings (IEEE Cat. No.04TH8720)*, ig Sky, MT, USA,, 2004.

[10] W. Wondrak, "Physical Limits and Lifetime Limitations of Semiconductor Devices at High Temperature," *elsevier,* 1999.

[11] P. G. NEUDECK, "High-Temperature Electronics—A Role for Wide Bandgap Semiconductors," in *IEEE,* 2002.

[12] A. R. P. A. L. B. ROWLAND, "SiC Materials—Progress, Status, and Potential Roadblock," in *PROCEEDINGS OF THE IEEE,* 2002.

[13] ,. S. J.-S. (. L. Allen R. Hefner, "SiC Power Diodes Provide Breakthrough Performance for a Wide Range of Applications," *IEEE TRANSACTIONS ON POWER ELECTRONIC,* vol. VOL. 16, 2001.

[14] P. M. Castro, I. E. Grossmann, P. Veldhuizen and D. Esplin, "Optimal Maintenance Scheduling of a Gas Engine Power Plant Using Generalized Disjunctive Programming," *AIChE,* 2014.

[15] H. v. D. a. M. H. C. A.D. Foster, "FUELS FLEXIBILITY IN HEAVY-DUTY GAS TURBINES," in *General Electric*, New York, 1983.

[16] M. P. Boyce, Gas Turbine Engineering, elsevier science and technology, 2011.

[17] J. W. J. Zhao, "Ultrahigh-Temperature Materials for Jet Engines," *MRS Bulletin 28*, no. https://doi.org/10.1557/mrs2003.189, p. 622–630, 2003.

[18] J. L. E. P. J. J. R. T. a. M. C. R. W. Johnson, "The changing automotive environment: high-temperature electronics," *EEE Transactions on Electronics Packaging Manufacturing, vol. 27, no. 3*, no. doi: 10.1109/TEPM.2004.843109, pp. pp. 164-176, 2004.

[19] F. B. J. G. I. C. e. a. Edler, " Pt-40%Rh Versus Pt-6%Rh Thermocouples: An emf-Temperature Reference Function for the Temperature Range," *Springler,* Vols. https://doi.org/10.1007/s10765-021-02895-w, 2021.

[20] C. W. e. al., "TiB_2/SiCN Thin-Film Strain Gauges Fabricated by Direct Writing for High-Temperature Application," *IEEE Sensors Journal*, vol. oi: 10.1109/JSEN.2022.3172346..

[21] M. P. Da Cunha, "High-temperature harsh-environment SAW sensor technology," in *IEEE International Ultrasonics Symposium (IUS)*, 2023.

[22] P. F. e. al., "SOI technology for high-temperature applications," vol. https://doi.org/10.1109/IEDM.1992.307590., pp. 353-356, 1992 International Technical Digest on Electron Devices Meeting.

[23] H. Kappert, N. Kordas, S. Dreiner, U. Paschen and R. Kokozinski, "High temperature SOI CMOS technology and circuit realization for applications up to 300°C," in *2015 IEEE International Symposium on Circuits and Systems (ISCAS)*, 2015.

[24] M. A. B. B. J. S. C. V. Huque, "Huque, M. A., et al. "SOI based integrated circuits for high-temperature applications.," in *Proceedings of International Conference and Exhibition on High Temperature Electronics*, Albuquerque, New Mexico., 2008.

[25] H. M. X. R. L. M. A. G. Z. a. G. T. B. F. M. Shah, "Comparative performance evaluation of temperature dependent characteristics and power converter using GaN, SiC and Si power devices," in *2018 IEEE 12th International Conference on Compatibility, Power Electronics and Power Engineering (CPE-POWERENG 2018)*, Doha, Qatar, 2018.

[26] S. J. Pearton, J. C. Zolper, R. J. Shul and F. Ren, "GaN: Processing, defects, and devices," *Journal of applied physics* , vol. 86, no. https://doi.org/10.1063/1.371145, pp. 1-78, 1999.

[27] A. Hassan, "Circuits Techniques for wireless sensing systems in high temperature envirnments," 2019.

[28] S. M. L. F. A. G. V. P. Araujo D, "Diamond for Electronics: Materials, Processing and Devices. Materials," *Materials (Basel)*, vol. doi: 10.3390/ma14227081. PMID: 34832481; PMCID: PMC8623275..

[29] 1. S. L. G. D. J. S. Philip G. Neudeck, "Extreme temperature 6H-SiC JFET integrated circuit technology," *Phys. Status Solidi*, no. DOI 10.1002/pssa.200925188, p. 2329–2345, 2009.

[30] B. J. K. B. C. ,. A. P. P. Debbie G. Senesky, "Harsh Environment Silicon Carbide Sensors for Health and Performance Monitoring of Aerospace Systems: A Review," *IEEE SENSORS JOURNAL*, vol. 9, no. 11, 2009.

[31] M. C. S. e. al, "Wireless capacitive pressure sensor operating up to 400 °C from 0 to 100 PSI utilizing power scavenging," in *Proc. IEEE Topical Conf. Wireless Sensors Sensor Netw*, 2014.

[32] S. J. S. B. V. C. a. B. S. A. Padhy, "A survey of energy and spectrum harvesting technologies and protocols for Next generation Wireless networks," *IEEE Access*, vol. 9, no. : 10.1109/access.2020.3046770., p. 1737–1769, 2021.

[33] D. G. G. M. Y. S. A. A. S. a. M. S. R. Y. I. Shtern, "Multisectional thermoelement for generators working at the temperatures up to 1200 K," in *Proc. IEEE Conf. Russian Young Res. Elect. Electron. Eng*, 2017.

[34] R. B. T. H. T. C. S. K. a. B. S. T. C. Holgate, "Increasing the efficiency of the multi-mission radioisotope thermoelectric generator," *J. Electron. Mater*, vol. 44, pp. 1814-1821, 2015.

[35] S. W. a. C. Y. Y. Xie, "Generation of electricity from deep-sea hydrothermal vents with a thermoelectric converter," *Appl. Energy*, vol. 164, pp. 620-627, 2016.

[36] A. A. N. a. G. C. T. Y. Kim, "Waste heat recovery of a diesel engine using a thermoelectric generator equipped with customized thermoelectric modules," *Energy Convers. Manage*, vol. 124, pp. 280-286, 2016.

[37] Y.-C. C. F. C. T. D. a. H. Y. Q. Lin, "Design and experiments of a thermoelectric-powered wireless sensor network platform for smart building envelope," *Appl. Energy*, vol. 305, 2022.

[38] N. T. L. D. J. K. N. E. M. P. d. C. Shane Winters, "High Temperature wireless platform powered by Energy Scavenging," *IEEE open journal of industry applications*, 2024.

[39] G. Gonzalez, Foundation of Oscillator Circuit Design, 2006.

[40] E. (n.d.)., " Ring Oscillator: Working and Its Applications. Retrieved from https://www.elprocus.com/ring-oscillator-working-and-its-applications/".

[41] R. Schaumann, Design of Analog Filters, OXFORD UNIVERSITY PRESS, 2001, pp. 483-489.

[42] I. P. a. L. M. M. Azadmehr, "100 years of Colpitts Oscillators: Ontology Review of Common Oscillator Circuit Topologies," *EEE Circuits and Systems Magazine*, vol. 20, no. 4, pp. 8-27, 2020.

[43] N. M. J. &. N. D. Fox, "Radiometric Aspects of an Experiment to Determine the Melting/Freezing Temperature of Gold.," *Metrologia,* pp. 221-227, 1991.

[44] H. S. F. &. O. A. Sakate, "Observation of Al2O3 melting and freezing plateaus using a cavity-type tungsten crucible," *Metrologia,,* no. 32, pp. 129-131, 1995.

[45] A. M. M. F. P. S. M. Ranjan R. Lamichhane, "A Wide Bandgap Silicon Carbide (SiC) Gate Driver for High-Temperature and High-Voltage Applications," in *International Symposium on Power Semiconductor Devices & IC's*, Waikoloa, Hawaii, 2014.

[46] C.-W. Choi, J.-H. So, J.-S. K. and and D.-K. Kim, "Influence Analysis of SiC MOSFET's Parasitic Capacitance on DAB Converter Output," mdpi , https://doi.org/10.3390/electronics12010182, 2022.

[47] I. Cree, "C3M0075120K Silicon Carbide Power MOSFET. C3M™ MOSFET Technology (Rev. 5).," Cree, Inc., (2021).

[48] J. Zanoni, "Simulation and teting of high temperature oscillator circuit," University of Maine Honors thesis , Orono, 2022.

[49] W. H. K. a. D. J. Y. R. Wang, "Silicon-carbide MESFET-based 400C MEMS sensing and data telemetry"," *IEEE Sensors J,* vol. 5, no. 6, pp. 1389-1394, 2005.

[50] O. T. J. T. C. H. Manabendra Saha, "A review of thermoelectric generators for waste heat recovery in marine applications," *Sustainable Energy Technologies and Assessments,* no. https://doi.org/10.1016/j.seta.2023.103394., pp. 2213-1388, 2023.

[51] A. R. M. &. M. S. &. H. B. V. Siddique, "A review of the state of the science on wearable thermoelectric power generators (TEGs) and their existing challenges," *Renewable and Sustainable Energy Reviews,,* vol. https://doi.org/10.1016/j.rser.2017.01.177., no. ISSN 1364-0321,, pp. 730-744, 2017.

APPENDIX

APPENDIX A. Open loop analysis

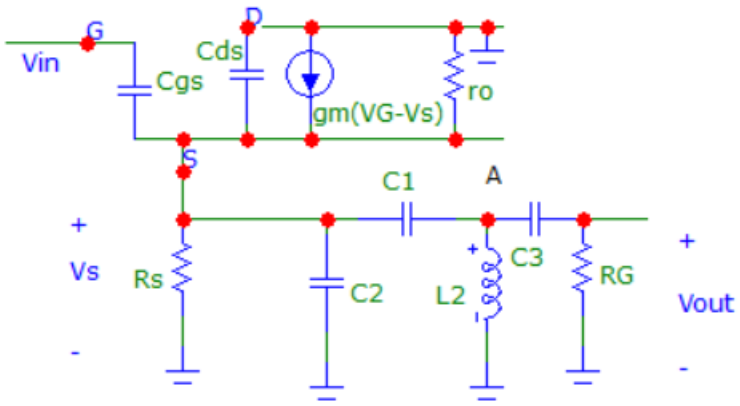

Figure 14: Detailed Open Loop Model of the Circuit

As explained in section 2.4.2 Figure 14 is the open loop model of the oscillator circuit and nodal equations 18-20 were solved using MATLAB.

The expression for gain of the transfer function obtained from MATLAB for open loop analysis is given by equation A1.

$$G(jw) = -(C\_gs + gm)/(((C\_1\,(1/R\_G\ + 2\pi fjC\_3))/C\_3\ - (2\pi fjC\_3 + (1/R\_G\ + 2\pi fjC\_3)(2\pi fjC\_1 + 2\pi fjC\_3 - j/(2f\pi L\_1\,))j)/(2f\pi C\_3\,)(gm + 1/R\_s\ + 1/r\_o\ + 2\pi fjC\_1 + 2\pi fjC\_2 + 2\pi fjC\_ds + 2\pi fjC\_gs)j)\ 2f\pi C\_1\,) \quad \text{(A1)}$$

The phase of the transfer function at each frequency point was determined using 'atan2d' function which gives the phase as expressed in equation A2.

$$\phi(j2\pi f) = \frac{180 \cdot \operatorname{atan2}\left(\frac{(C_{gs}+g_m)(2\pi fC_1 - \frac{(2\pi fC_1 - \frac{j}{2f\pi L_1})(2\pi fC_1 + 2\pi fC_2 + 2\pi fC_{ds} + 2\pi fC_{gs})}{2\pi fC_1} + \frac{(g_m + \frac{1}{R_s} + \frac{1}{r_o})(2\pi fC_1 + 2\pi fC_3 - \frac{j}{2f\pi L_1})}{4j\pi^2 f^2 C_1 C_3 R_G})}{(\frac{(2\pi fC_1 - \frac{j}{2f\pi L_1})(g_m + \frac{1}{R_s} + \frac{1}{r_o})}{2\pi fC_1} - \frac{C_1}{C_3 R_G} + \frac{(2\pi fC_1 + 2\pi fC_3 - \frac{j}{2f\pi L_1})(2\pi fC_1 + 2\pi fC_2 + 2\pi fC_{ds} + 2\pi fC_{gs})}{4j\pi^2 f^2 C_1 C_3 R_G})^2 + (2\pi fC_1 - \frac{(2\pi fC_1 - \frac{j}{2f\pi L_1})(2\pi fC_1 + 2\pi fC_2 + 2\pi fC_{ds} + 2\pi fC_{gs})}{2\pi fC_1} + \frac{(g_m + \frac{1}{R_s} + \frac{1}{r_o})(2\pi fC_1 + 2\pi fC_3 - \frac{j}{2f\pi L_1})}{4j\pi^2 f^2 C_1 C_3 R_G})^2}\right)}{\pi} \quad \text{(A2)}$$

The expression for frequency is obtained by setting the imaginary part of the transfer function to Zero which is given by equation A3.

$$
\begin{aligned}
f = ((\sqrt{(} & C1\text{^}2\ C3\text{^}2\ RG\text{^}2\ Rs\text{^}2\ ro\text{^}2 + 2C1\text{^}2\ C3L1RGRs\text{^}2\ gmro\text{^}2 + 2C1\text{^}2\ C3L1RGRs\text{^}2 + 2C1\text{^}2\ C3L1RG\ Rsro\text{^}2 \\
& + C1\text{^}2\ L1\text{^}2\ Rs\text{^}2\ gm\text{^}2\ ro\text{^}2 + 2C1\text{^}2\ L1\text{^}2\ Rs\text{^}2\ gmro + C1\text{^}2\ L1\text{^}2\ Rs\text{^}2 \\
& + 2C1\text{^}2\ L1\text{^}2\ Rsgmro\text{^}2 + 2C1\text{^}2\ L1\text{^}2\ Rsro + C1\text{^}2\ L1\text{^}2\ ro\text{^}2 + 2C1C2C3\text{^}2\ RG\text{^}2\ Rs\text{^}2\ ro\text{^}2 \\
& - 2C1C2C3L1RGRs\text{^}2\ gmro\text{^}2 - 2C1C2C3L1RGRs\text{^}2\ ro - 2C1C2C3L1RGRsro\text{^}2 \\
& + 2C1C3\text{^}2\ CdsRG\text{^}2\ Rs\text{^}2\ ro\text{^}2 + 2C1C3\text{^}2\ CgsRG\text{^}2\ Rs\text{^}2\ ro\text{^}2 + 2C1C3\text{^}2\ L1RGRs\text{^}2\ gmro\text{^}2 \\
& + 2C1C3\text{^}2\ L1RGRs\text{^}2\ ro + 2C1C3\text{^}2\ L1RGRsro\text{^}2 - 2C1C3CdsL1RGRs\text{^}2\ gmro\text{^}2 \\
& - 2C1C3CdsL1RGRs\text{^}2\ ro - 2C1C3CdsL1RGRsro\text{^}2 - 2C1C3CgsL1RGRs\text{^}2\ gmro\text{^}2 \\
& - 2C1C3CgsL1RGRs\text{^}2\ ro - 2C1C3CgsL1RGRsro\text{^}2 + 2C1C3L1\text{^}2\ Rs\text{^}2\ gm\text{^}2\ ro\text{^}2 \\
& + 4C1C3L1\text{^}2\ Rs\text{^}2\ gmro + 2C1C3L1\text{^}2\ Rs\text{^}2 + 4C1C3L1\text{^}2\ Rsgmro\text{^}2 + 4C1C3L1\text{^}2\ Rsro \\
& + 2C1C3L1\text{^}2\ ro\text{^}2 + C2\text{^}2\ C3\text{^}2\ RG\text{^}2\ Rs\text{^}2\ ro\text{^}2 + 2C2C3\text{^}2\ CdsRG\text{^}2\ Rs\text{^}2\ ro\text{^}2 \\
& + 2C2C3\text{^}2\ CgsRG\text{^}2\ Rs\text{^}2\ ro\text{^}2 + 2C2C3\text{^}2\ L1RGRs\text{^}2\ gmro\text{^}2 + 2C2C3\text{^}2\ L1RGRs\text{^}2\ ro \\
& + 2C2C3\text{^}2\ L1RGRsro\text{^}2 + C3\text{^}2\ Cds\text{^}2\ RG\text{^}2\ Rs\text{^}2\ ro\text{^}2 + 2C3\text{^}2\ CdsCgsRG\text{^}2\ Rs\text{^}2\ ro\text{^}2 \\
& + 2C3\text{^}2\ CdsL1RGRs\text{^}2\ gmro\text{^}2 + 2C3\text{^}2\ CdsL1RGRs\text{^}2\ ro + 2C3\text{^}2\ CdsL1RGRsro\text{^}2 \\
& + C3\text{^}2\ Cgs\text{^}2\ RG\text{^}2\ Rs\text{^}2\ ro\text{^}2 + 2C3\text{^}2\ CgsL1RGRs\text{^}2\ gmro\text{^}2 + 2C3\text{^}2\ CgsL1RGRs\text{^}2\ ro \\
& + 2C3\text{^}2\ CgsL1RGRsro\text{^}2 + C3\text{^}2\ L1\text{^}2\ Rs\text{^}2\ gm\text{^}2\ ro\text{^}2 + 2C3\text{^}2\ L1\text{^}2\ Rs\text{^}2\ gmro \\
& + C3\text{^}2\ L1\text{^}2\ Rs\text{^}2 + 2C3\text{^}2\ L1\text{^}2\ Rsgmro\text{^}2 + 2C3\text{^}2\ L1\text{^}2\ Rsro + C3\text{^}2\ L1\text{^}2\ ro\text{^}2\ ) + C1L1Rs \\
& + C3L1Rs + C1L1ro + C3L1ro + C1L1Rsgmro + C3L1Rsgmro + C1C3RGRsro + C2C3RGRsro \\
& + C3CdsRGRsro + C3CgsRGRsro)/8(C1C2C3L1RGRsro\pi\text{^}2 + C1C3CdsL1RGRsro\pi\text{^}2 \\
& + C1C3CgsL1RGRsro\pi\text{^}2\ )\ )\text{^}(1/2)\ )
\end{aligned}
\tag{A3}
$$

APPENDIX B: MATLAB script for Sensitivity analysis

This code performs sensitivity analysis and frequency response simulation of a high-temperature oscillator circuit using MATLAB. Initially, it sets up the circuit parameters, including frequency range, component values (like transconductance, threshold voltage, supply voltage, resistances, capacitances, and inductances), and characteristics specific to a CREE Silicon Carbide Power MOSFET. The script then proceeds with symbolic validation using a system of nodal equations to model the circuit behavior analytically. The equations are solved to obtain the magnitude and phase response and imaginary part is set to zero and the resonant frequency of the oscillation is obtained. The sensitivity analysis section calculates how changes in specific component values (C1, C2, L1, and Cgs) affect the resonant frequency, providing insights into which components have the most significant impact on the circuit's performance. However, it is important to note that this analysis focuses on component sensitivities rather than the effects of high temperatures on the circuit, which is identified as a limitation in this approach. The script is shown below.

```
clear
close all
clc

%% Initialize Circuit Parameters

w = (0:1000:25e6)*2*pi;

gm_ = 10e-3;     %[S]
kn_ = 0.1;       %[A/V^2]
Vtn_ = 2.4;      %[V]
VDD_ = 5;        %[V]
Rs_ = 50;        %[ohms]
RG_ = 1e6;       %[ohms]

L1_ = 600e-9;   %[H]
C1_ = 1e-9;     %[F]
C2_ = 1e-9;     %[F]
```

```
C3_ = 82e-9;     %[F]

% CREE MOSFET internal characteristics


ro_ = 1e3;

Ciss = 1350e-12; % input capacitance [F]
Coss = 58e-12; % output capacitance [F]
Crss = 3e-12; % reverse transfer capacitance [F]

Cgd_ = Crss;       % gate-drain capacitance
Cds_ = Coss - Cgd_; % drain-source capacitance
Cgs_ = Ciss - Cgd_; % gate-source capacitance

%% Symbolic Validation of Derived Formulas

syms Vout Vin Vgs Vs VA VB VG VDD Vtn ID ...
   L1 C1 C2 C3 Cgs Cds Cgd Rs RG ro RDD ...
   gm kn s f

vars = [Vout Vin Vgs Vs VA VB VG VDD Vtn ID L1 C1 C2 C3 Cgs Cds Cgd Rs RG ro RDD
gm kn s f];
assume(vars,"real")
assume(vars,"positive")

% system of nodal equations

eqGiven = Vgs == VG - Vs;
eqA= Vs*(s*Cds+s*C1+s*C2+s*Cgs+1/Rs + 1/ro)-VG*s*Cgs-gm*Vgs-Vout*s*C1==0;
eqB = Vout*(s*C1+1/(s*L1))-Vs*(s*C1)==0;
eqC = VG*(s*C3+s*Cgd+s*Cgs+1/RG)-Vin*(s*C3)-Vs*(s*Cgs)==0;

Vs_Vout = solve(eqB,Vs);
Vgs_VGVs = solve(eqGiven,Vgs);
eqA2 = subs(eqA,Vgs,Vgs_VGVs);
eqA3 = subs(eqA2,Vs,Vs_Vout);
VG_Vout=solve(eqA3,VG);
eqC2 = subs(eqC,VG,VG_Vout);

eqC3 = subs(eqC2,Vs,Vs_Vout);
G_s = simplify(solve(eqC3,Vout)/Vin);


eqD = 2*Vs == kn*Rs*(VDD - Vtn - Vs)^2;
eqE = ID == Vs/Rs;
```

```
eqF = gm == sqrt(2*kn*ID);
Vs_Rs = solve(eqD,Vs,"ReturnConditions",true);
ID_Rs1 = solve(subs(eqE,Vs,Vs_Rs.Vs(1)),ID,"ReturnConditions",true);
ID_Rs2 = solve(subs(eqE,Vs,Vs_Rs.Vs(2)),ID,"ReturnConditions",true);
gm_Rs1 = solve(subs(eqF,ID,ID_Rs1.ID),gm,"ReturnConditions",true);
gm_Rs2 = solve(subs(eqF,ID,ID_Rs2.ID),gm,"ReturnConditions",true);


G_s = subs(G_s,gm,gm_Rs2.gm);

G_s = subs(G_s,[VDD,Vtn,kn],[VDD_,Vtn_,kn_]);

G_jw = subs(G_s,s,1j*2*pi*f*1e6); % function of f in [MHz]
phi_jw = atan2d(imag(G_jw),real(G_jw));


% frequency response as function of f [MHz]

G_jw1 = simplify (subs (G_jw, [Rs,
RG,ro,L1,C1,C2,C3,Cgs,Cds,Cgd],[Rs_,RG_,ro_,L1_,C1_,C2_,C3_,Cgs_,Cds_,Cgd_]));
phi_jw1 = simplify (subs(phi_jw,
[Rs,RG,ro,L1,C1,C2,C3,Cgs,Cds,Cgd],[Rs_,RG_,ro_,L1_,C1_,C2_,C3_,Cgs_,Cds_,Cgd_]));

%%sensitivity calculation
% Partial derivatives
df_C1_sym = diff (f_sym, C1);
df_C2_sym = diff (f_sym, C2);
df_L1_sym = diff (f_sym, L1);
df_Cgs_sym = diff (f_sym, Cgs);

% Normalized sensitivity
S_C1_sym = (C1/f_sym) *df_C1_sym;
S_C2_sym = (C2/f_sym) *df_C2_sym;
S_L1_sym = (L1/f_sym) *df_L1_sym;
S_Cgs_sym = (Cgs/f_sym) *df_Cgs_sym;

% Substitute values for all variables
S_C1_value = double (subs(S_C1_sym, [RG, ro, L1, C1, C2, C3, Cgs, Cds, Cgd, kn, Rs, VDD,
Vtn], ...
   [RG_, ro_, L1_, C1_, C2_, C3_, Cgs_, Cds_, Cgd_, kn_, Rs_, VDD_, Vtn_]));
S_C2_value = double (subs(S_C2_sym, [RG, ro, L1, C1, C2, C3, Cgs, Cds, Cgd, kn, Rs, VDD,
Vtn], ...
   [RG_, ro_, L1_, C1_, C2_, C3_, Cgs_, Cds_, Cgd_, kn_, Rs_, VDD_, Vtn_]));
S_L1_value = double (subs(S_L1_sym, [RG, ro, L1, C1, C2, C3, Cgs, Cds, Cgd, kn, Rs, VDD,
Vtn], ...
   [RG_, ro_, L1_, C1_, C2_, C3_, Cgs_, Cds_, Cgd_, kn_, Rs_, VDD_, Vtn_]));
```

```
S_Cgs_value = double (subs(S_Cgs_sym, [RG, ro, L1, C1, C2, C3, Cgs, Cds, Cgd, kn, Rs, VDD,
Vtn], ...
   [RG_, ro_, L1_, C1_, C2_, C3_, Cgs_, Cds_, Cgd_, kn_, Rs_, VDD_, Vtn_]));
fprintf('Normalized sensitivity for C1: %f\n', S_C1_value);
fprintf('Normalized sensitivity for C2: %f\n', S_C2_value);
fprintf('Normalized sensitivity for Cgs: %f\n', S_Cgs_value);

Figure()
bar_labels = categorical({'C1','C2','L','Cgs'});
bar_values = [S_C1_value,S_C2_value,S_L1_value,S_Cgs_value];
bar(bar_labels, bar_values);
ylabel('Normalized Sensitivity');
title('Sensitivity Analysis for Source Follower Oscillator')
```

APPENDIX C: Montecarlo Analysis in MATLAB

This MATLAB code performs Monte Caro simulation to access the variability of a frequency function derived from open loop analysis in section 2.4.2, considering the tolerances of various components including resistors, capacitors, inductors, MOSFET's parasitic capacitances, Cgs and Cds, and transconductance (gm). The simulation runs 1000 times, each time randomly varying the component values within their specified tolerances. The frequency function (f) is computed at each iteration with varied component values, the results are stored, and a histogram is plotted to visualize the distribution of calculated frequencies. However, the limitation of this model is that it doesn't directly account for the effects of temperature on component values.

```
clear all;
close all;

% Defining constants
N = 1000;  % Number of simulations

% Defining component tolerance parameters
MOSFET_CAPACITOR_TOLERANCE = 0.20; %power mosfet(±20%)
CAPACITOR_TOLERANCE = 0.05; % Tolerance for capacitors (±5%)
INDUCTOR_TOLERANCE = 0.20;   % Tolerance for inductors (±20%)
RESISTOR_TOLERANCE = 0.05;   % Tolerance for resistors (±5%)
gm_tolerance = 0.20; %%tolerance of gm(±20%)
pi = 3.1416;
```

```
% Define the symbolic variables
syms C1 C2 C3 RG Rs ro gm L1 Cds Cgs

% Define f as a function of these symbolic variables obtained from small signal model
f = (((C1^2*C3^2*RG^2*Rs^2*ro^2 + 2*C1^2*C3*L1*RG*Rs^2*gm*ro^2 +
2*C1^2*C3*L1*RG*Rs^2*ro + 2*C1^2*C3*L1*RG*Rs*ro^2 + C1^2*L1^2*Rs^2*gm^2*ro^2
+ 2*C1^2*L1^2*Rs^2*gm*ro + C1^2*L1^2*Rs^2 + 2*C1^2*L1^2*Rs*gm*ro^2 +
2*C1^2*L1^2*Rs*ro + C1^2*L1^2*ro^2 + 2*C1*C2*C3^2*RG^2*Rs^2*ro^2 -
2*C1*C2*C3*L1*RG*Rs^2*gm*ro^2 - 2*C1*C2*C3*L1*RG*Rs^2*ro -
2*C1*C2*C3*L1*RG*Rs*ro^2 + 2*C1*C3^2*Cds*RG^2*Rs^2*ro^2 +
2*C1*C3^2*Cgs*RG^2*Rs^2*ro^2 + 2*C1*C3^2*L1*RG*Rs^2*gm*ro^2 +
2*C1*C3^2*L1*RG*Rs^2*ro + 2*C1*C3^2*L1*RG*Rs*ro^2 -
2*C1*C3*Cds*L1*RG*Rs^2*gm*ro^2 - 2*C1*C3*Cds*L1*RG*Rs^2*ro -
2*C1*C3*Cds*L1*RG*Rs*ro^2 - 2*C1*C3*Cgs*L1*RG*Rs^2*gm*ro^2 -
2*C1*C3*Cgs*L1*RG*Rs^2*ro - 2*C1*C3*Cgs*L1*RG*Rs*ro^2 +
2*C1*C3*L1^2*Rs^2*gm^2*ro^2 + 4*C1*C3*L1^2*Rs^2*gm*ro + 2*C1*C3*L1^2*Rs^2 +
4*C1*C3*L1^2*Rs*gm*ro^2 + 4*C1*C3*L1^2*Rs*ro + 2*C1*C3*L1^2*ro^2 +
C2^2*C3^2*RG^2*Rs^2*ro^2 + 2*C2*C3^2*Cds*RG^2*Rs^2*ro^2 +
2*C2*C3^2*Cgs*RG^2*Rs^2*ro^2 + 2*C2*C3^2*L1*RG*Rs^2*gm*ro^2 +
2*C2*C3^2*L1*RG*Rs^2*ro + 2*C2*C3^2*L1*RG*Rs*ro^2 +
C3^2*Cds^2*RG^2*Rs^2*ro^2 + 2*C3^2*Cds*Cgs*RG^2*Rs^2*ro^2 +
2*C3^2*Cds*L1*RG*Rs^2*gm*ro^2 + 2*C3^2*Cds*L1*RG*Rs^2*ro +
2*C3^2*Cds*L1*RG*Rs*ro^2 + C3^2*Cgs^2*RG^2*Rs^2*ro^2 +
2*C3^2*Cgs*L1*RG*Rs^2*gm*ro^2 + 2*C3^2*Cgs*L1*RG*Rs^2*ro +
2*C3^2*Cgs*L1*RG*Rs*ro^2 + C3^2*L1^2*Rs^2*gm^2*ro^2 + 2*C3^2*L1^2*Rs^2*gm*ro
+ C3^2*L1^2*Rs^2 + 2*C3^2*L1^2*Rs*gm*ro^2 + 2*C3^2*L1^2*Rs*ro +
C3^2*L1^2*ro^2)^(1/2) + C1*L1*Rs + C3*L1*Rs + C1*L1*ro + C3*L1*ro +
C1*L1*Rs*gm*ro + C3*L1*Rs*gm*ro + C1*C3*RG*Rs*ro + C2*C3*RG*Rs*ro +
C3*Cds*RG*Rs*ro + C3*Cgs*RG*Rs*ro)/(8*(C1*C2*C3*L1*RG*Rs*ro*pi^2 +
C1*C3*Cds*L1*RG*Rs*ro*pi^2 + C1*C3*Cgs*L1*RG*Rs*ro*pi^2)))^(1/2); % the formula
using these variables

% Define initial component values
gm_i = 0.101;     %[S]
kn_ = 0.1;        %[A/V^2]
Vtn_ = 2.6;       %[V]
VDD_ = 6;         %[V]
Rs_i = 50;        %[ohms]
RG_i = 1e6;       %[ohms]
L1_i = 600e-9;    %[H]
C1_i = 1e-9;      %[F]
C2_i = 1e-9;      %[F]
C3_i = 82e-9;     %[F]
ro_i = 1e3;
```

```
Ciss = 1350e-12; % input capacitance [F]
Coss = 58e-12; % output capacitance [F]
Crss = 3e-12; % reverse transfer capacitance [F]

Cgd_ = Crss;      % gate-drain capacitance
Cds_i = Coss - Cgd_; % drain-source capacitance
Cgs_i = Ciss - Cgd_; % gate-source capacitance

% Initialize vector to store results
results = zeros(1, N);
% Run simulations
for i = 1:N
   % Generate random variations for each component type
   mosfet_capacitor_variation = 1 + MOSFET_CAPACITOR_TOLERANCE * (2 * rand(2, 1) -
1);
   capacitor_variation = 1 + CAPACITOR_TOLERANCE * (2 * rand(5, 1) - 1);
   inductor_variation = 1 + INDUCTOR_TOLERANCE * (2 * rand(1, 1) - 1);
   resistor_variation = 1 + RESISTOR_TOLERANCE * (2 * rand(3, 1) - 1);
   gm_variation =1 +gm_tolerance*(2*rand(1,1)-1);

   % Apply variations to initial values
   C1_v = C1_i * capacitor_variation(1);
   C2_v = C2_i * capacitor_variation(2);
   C3_v = C3_i * capacitor_variation(3);
   RG_v = RG_i * resistor_variation(1);
   Rs_v = Rs_i * resistor_variation(2);
   ro_v = ro_i * resistor_variation(3);
   gm_v = gm_i * gm_variation(1);
   L1_v = L1_i * inductor_variation;
   Cds_v = Cds_i * mosfet_capacitor_variation(1);
   Cgs_v = Cgs_i * mosfet_capacitor_variation(2);

   % Substitute the variables in the function f with their values
   f_val = subs(f, {C1, C2, C3, RG, Rs, ro, gm, L1, Cds, Cgs}, {C1_v, C2_v, C3_v, RG_v, Rs_v,
ro_v, gm_v, L1_v, Cds_v, Cgs_v});

   % Store result
   results(i) = double(f_val);
end

% Plot histogram of results
histogram(results);
% Calculate mean and standard deviation
mean_value = mean(results)
std_deviation = std(results)
xlabel('Frequency');
```

```
ylabel('Number of Simulations');
title('Histogram of Frequency for Montecarlo Simulations');
grid on;
```

BIOGRAPHY OF THE AUTHOR

Nikung Thapa was born in Palpa, Nepal and completed his high school education at New Horizon English Boarding Higher Secondary School in Palpa in 2012. He earned a Bachelor of Science in Electronics and Communication Engineering from Tribhuvan University's Institute of Engineering, Western Region Campus, in May 2017. After that, Nikung worked as an Electronics Engineer at Avian Engineering Services in Palpa, Nepal till 2020. Then he began his graduate studies in the Electrical and Computer Engineering department at The University of Maine, where he has been actively involved as a Teaching Assistant and a Research Assistant at the Frontier Institute for Research in Sensor Technologies (FIRST) from August 2021 to August 2023. He is a candidate for the Master of Science degree in Electrical Engineering from University of Maine in May 2024.